



Lawrence Berkeley Laboratory

UNIVERSITY OF CALIFORNIA

Materials & Molecular Research Division

MODELING OF CHANGING ELECTRODE PROFILES

Geoffrey Allan Prentice
(Ph.D. thesis)

December 1980

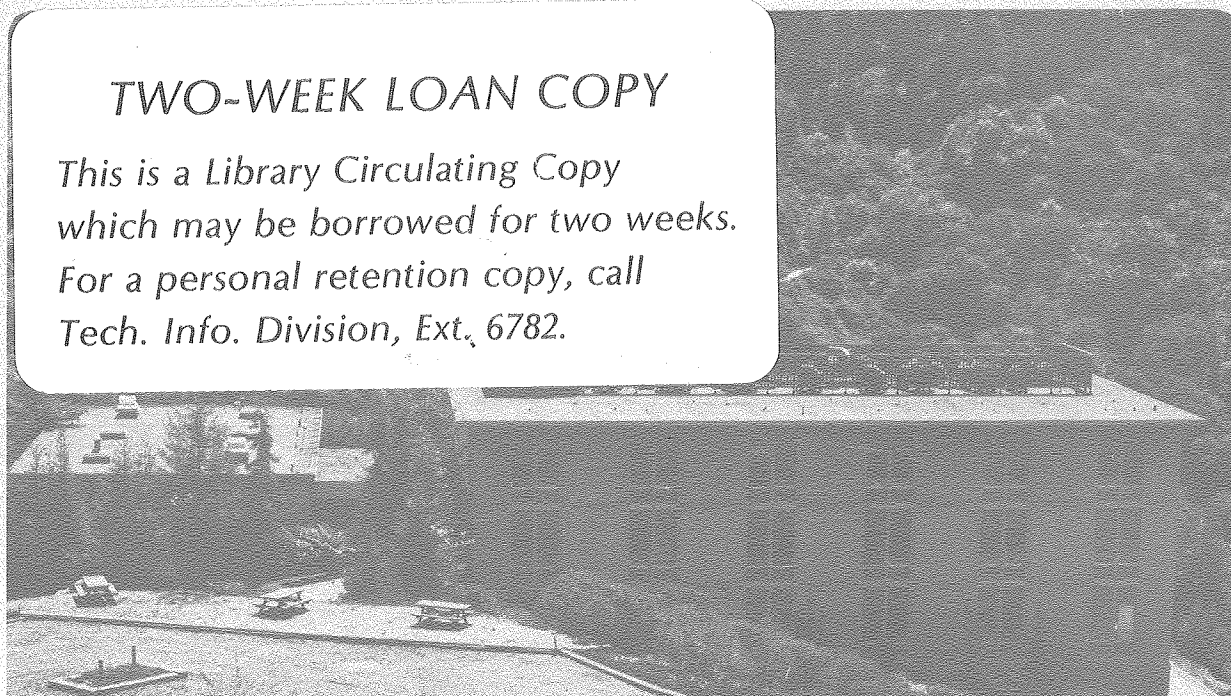
RECEIVED
LAWRENCE
BERKELEY LABORATORY

FEB 17 1981

LIBRARY AND
DOCUMENTS SECTION

TWO-WEEK LOAN COPY

*This is a Library Circulating Copy
which may be borrowed for two weeks.
For a personal retention copy, call
Tech. Info. Division, Ext. 6782.*



LBL-11694 c. 2

DISCLAIMER

This document was prepared as an account of work sponsored by the United States Government. While this document is believed to contain correct information, neither the United States Government nor any agency thereof, nor the Regents of the University of California, nor any of their employees, makes any warranty, express or implied, or assumes any legal responsibility for the accuracy, completeness, or usefulness of any information, apparatus, product, or process disclosed, or represents that its use would not infringe privately owned rights. Reference herein to any specific commercial product, process, or service by its trade name, trademark, manufacturer, or otherwise, does not necessarily constitute or imply its endorsement, recommendation, or favoring by the United States Government or any agency thereof, or the Regents of the University of California. The views and opinions of authors expressed herein do not necessarily state or reflect those of the United States Government or any agency thereof or the Regents of the University of California.

MODELING OF CHANGING ELECTRODE PROFILES

Geoffrey Allan Prentice

Materials and Molecular Research Division
Lawrence Berkeley Laboratory

and

Department of Chemical Engineering
University of California
Berkeley, California 94720

This work was supported by the U.S. Department of Energy
under Contract No. W-7405-ENG-48.

CONTENTS

Abstract	v
Acknowledgments.	vii
Nomenclature	viii
1. Introduction.	1
2. Model	10
3. Numerical Procedure	14
4. Experimental Program.	50
5. Experimental Results and Analysis	63
6. Results of Simulated Experiments.	71
7. Effects of Ohmic Drop and Curvature	81
8. Simulations of Selected Geometries.	99
9. Summary and Conclusions	143
Appendices	147
A. Program Description	147
B. Program Details	150
C. Program Variables	162
D. Program Listing	169
E. Deposition on a Sinusoidal Profile.	199
F. Calculation of Node Potentials.	205
G. Numerical Differentiation Procedure	208
H. Lagrangian Interpolation.	211
I. Overpotential Calculations in the Butler-Volmer Equation	212
J. Initial Estimates for Surface Potential	213
K. Node Arrangements for Potential Calculation	215
L. Node Arrangements for Potential Calculation near Surface	218
M. Node Arrangements for Current Calculations.	220
References	222

MODELING OF CHANGING ELECTRODE PROFILES

Geoffrey Allan Prentice

Materials and Molecular Research Division
Lawrence Berkeley Laboratory

and

Department of Chemical Engineering
University of California
Berkeley, California 94720Abstract

A model for simulating the transient behavior of solid electrodes undergoing deposition or dissolution has been developed. The model accounts for ohmic drop, charge transfer overpotential, and mass transport limitations. The finite difference method, coupled with successive overrelaxation, was used as the basis of the solution technique. An algorithm was devised to overcome the computational instabilities associated with the calculations of the secondary and tertiary current distributions. Simulations were performed on several model electrode profiles: the sinusoid, the rounded corner, and the notch.

Quantitative copper deposition data were obtained in a contoured rotating cylinder system. Sinusoidal cross-sections, machined on stainless steel cylinders, were used as model geometries. Kinetic parameters for use in the simulation were determined from polarization curves obtained on copper rotating cylinders. These parameters, along with other physical property and geometric data, were incorporated in simulations of growing sinusoidal profiles. The copper distributions on the

sinusoidal cross-sections were measured and found to compare favorably with the simulated results.

At low Wagner numbers the formation of a slight depression at the profile peak was predicted by the simulation and observed on the profile. At higher Wagner numbers, the simulated and experimental results showed that the formation of a depression was suppressed. This phenomenon was shown to result from the competition between ohmic drop and electrode curvature.

ACKNOWLEDGMENTS

It has been my privilege to work with Charles Tobias these past several years. He has been a continual source of fruitful research ideas and delightfully irreverent aphorisms. With characteristic immodesty he once stated that he took better care of his students than they took of themselves--unfortunately, I have found this to be true. I have appreciated the assistance provided by Larry Galovich, a truly resourceful and conscientious technician. My wife Merlyn has borne this period of impecuniosity and delayed gratification with remarkable grace. Finally, I have enjoyed free-associating with my colleagues, especially Paul Sides and Karrie Hanson. We never allowed mutual ignorance to impede a scientific discussion.

This work was supported by the U.S. Department of Energy under Contract No. W-7405-ENG-48.

NOMENCLATURE

A	amplitude (cm)
A_n	area (cm ²)
A_o	initial amplitude (cm)
c	concentration (mol/cm ³)
D	weighting factor
D_m	diffusivity
E	electric field (V/cm)
F	Faraday, 96500 C
H	distance (cm)
I	current (A)
i	current density (A/cm ²)
i_o	exchange current density (A/cm ²)
L	characteristic dimension (cm)
M	atomic weight (g/mol)
n	number of electrons participating in an electrode reaction
Q	charge (C)
Q_d	normalizing factor for charge (C)
Q^*	dimensionless charge

R	gas constant, 8.32 J/mol·K
Re	Reynolds number
r_i	inner cylinder radius (cm)
r_o	outer cylinder radius (cm)
s	unit strip width (cm)
S	surface
Sc	Schmidt number
t	time (s)
T	temperature (K)
u	displacement of average surface plane (cm)
v	velocity (cm/s)
V	electrode potential (V)
W	Wagner number
X,Y	Cartesian coordinates
z	equivalents/mol

x

Subscripts

a anodic
ap applied
b bulk
c cathode
cn concentration
j index of point on the surface
l limiting
n normal
p peak
r reference
rc recess
s surface
x abscissa component
y ordinate component

Superscripts

r iteration number in potential loop
s time step number

Greek Nomenclature

α	transfer coefficient
γ	exponent of concentration dependence
η	overpotential (V)
θ	angle between normal to the electrode surface and Y axis (rad)
κ	electrolyte conductivity ($\text{ohm}^{-1} \text{ cm}^{-1}$)
λ	wavelength (cm)
ν	kinematic viscosity (cm^2/s)
ρ	density (g/cm^3)
ϕ	potential (V)
ϕ_o	surface potential (V)

"How many men in all walks of life have gone through the world eking out a poor existence simply because there was no one to point out the way to success? How many unfortunates have dropped by the wayside, simply because they failed to start in life with a purpose? The object of this chapter is to encourage the youth who is seeking to place himself in life where he can be of use to the world and obtain knowledge by which he can always make a good living."

from the chapter Deposition of Copper

from a Sulphate of Copper Solution

in "The Practical Electroplater"

by Martin Brunor, 1894

1. INTRODUCTION

Heterogeneous reactions occurring at solid electrode surfaces often result in a change in the contour of an electrode. In electrochemical processes such as electrochemical machining and electroforming, the transformation of the surface geometry is the goal of the operation, while in other processes the shape change is undesirable and causes a deterioration in the performance of the system. On a small scale roughness or surface imperfections can be altered electrochemically. A surface can be electropolished by subjecting it to an anodic current so that protruding areas are preferentially dissolved. Microroughness can be reduced through cathodic leveling. A leveling agent, added to an electrolyte bath, causes more current to flow to microrecesses. When relatively more metal is deposited in the recess than on a protruding area, surface roughness is reduced.

The transformation of the electrode contour during battery cycling and the uneven oxidation of the anode in aluminum production are examples of undesirable electrode transfigurations. If redistribution of active material in a secondary battery causes the substrate to become exposed on discharging, then a loss of capacity results. In addition, a local increase in current density on charging may lead to an alteration of the deposit morphology which, as in the case of zinc, may be an undesirable dendritic form. For aluminum production some research effort is being directed toward developing an inert anode. The purpose of this effort is to retain control of the electrode separation as the process proceeds, and thus reduce ohmic losses.

In chlorine production the shape change of the anodes has been reduced through the use of the recently developed dimensionally stable anodes.

Although the shape change phenomena arise in a wide range of electrochemical applications, only a few attempts at modeling the electrochemical moving boundary problems have been undertaken. Calculating the current distribution is generally the crucial step in solving the moving boundary problem. With simplified boundary conditions current density distributions can be obtained without the aid of a computer; hence, the current distribution problem has been studied in greater detail.

In a series of papers presented in the early 1940's, Kasper¹ systematically applied analytical techniques to well-defined cell shapes (concentric cylinders, line-plane geometries, etc.) to calculate the current distribution. He extended techniques that had previously been used to solve field problems in mathematical physics to include the effects of linear polarization for selected electrochemical systems. Wagner² studied two important geometries where infinite current densities arise. He calculated current distributions on triangular waves and on plane parallel electrodes embedded in insulating walls. Using conformal mapping, he was able to include linear polarization on the plane electrodes, but only the primary current distribution and an approximate high current density distribution were derived for the triangular wave.

As high speed digital computers became more widely available in the 1960's, more complicated problems that were intractable by analytical methods proved amenable to numerical techniques. Klingert et al.³

outlined a procedure for calculating the primary and secondary current distribution by the finite difference method. They investigated the behavior of the current distribution on a corner electrode as geometric and polarization parameters were varied. Fleck et al.⁴ presented a general computer program for solving current distribution problems by the finite difference method. They studied the computational parameters and considered the relative merits of features such as increasing the size of the computational molecules, changing the order of computations, and varying the overrelaxation parameter. A catalog of current distribution problems previously solved by analytical methods is also contained in this report.

Problems where the mass transport effects are important (tertiary current distribution problems) also proved amenable to numerical techniques. By transforming the disk system to rotational elliptic coordinates, Newman⁵ calculated the tertiary current distribution on a rotating disk. Parrish and Newman⁶ computed the tertiary current distribution for plane parallel electrodes embedded in insulated walls. They presented results for a wide range of polarization parameters, concentrations, and electrode separations. Using a collocation technique, Caban and Chapman⁷ solved the same problem. They showed that good approximations to the solutions of Parrish and Newman could be obtained with relatively fewer boundary points. A substantial saving in computer time was realized since fewer intervals and fewer iterations were required.

Only a few simulations of the changing current distribution and concomitant electrode shape change for the transient problem have been conducted. The first such problem was considered by Wagner in

the early 1950's. Recognizing that changes in the electrode microprofile are of critical importance in the electropolishing process, he estimated the change in amplitude of a sinusoidal surface undergoing diffusion-controlled anodic dissolution. The expression that Wagner derived is limited to low amplitude-to-wavelength ratio profiles. The mathematical equivalence of the diffusion-controlled problem to the ohmically limited problem (primary current distribution) was also demonstrated.

Since the workpiece geometry in electrochemical machining must generally be determined by a trial and error procedure, a simulation of this process would be desirable. Nilson and Tsuei⁹ used an inverse Cauchy method to determine steady state workpiece geometries. By treating the spatial coordinates as the dependent variables, they were able to transform their problem into a rectangular domain, in which a solution by the finite difference method was easily obtained. They¹⁰ showed that the same inverted problem could be solved by using a series solution. The ohmic losses and variable conductivity were considered in their model. Riggs et al.¹¹ used the finite difference approach to model a high current density electrochemical machining process. By accounting for variables such as overpotential, gas production, temperature effects, and current efficiency, they successfully simulated the profiles obtained from hole sinking experiments on copper and type 302 stainless steel.

A model for the zinc electrode undergoing secondary battery cycling was developed by Choi et al.¹² They incorporated relevant phenomena such as overpotential, precipitation, membrane transport, and convective flow of the electrolyte in a one-dimensional model.

Using the recently developed finite element method, Alkire et al.¹³ predicted the electrode shape change of a flat cathode embedded in one wall of a rectangular cell. They computed profiles over a range of cell dimensions and polarization parameters.

Since the early 1960's few analytical solutions to current distribution problems have appeared in the literature. Clearly, the scope of analytical techniques is limited to those regular geometries (or those that can be transformed to well-defined domains) with simple boundary conditions. The most flexible method is conformal mapping. Although a number of well-known transformations are available for converting a geometry to a standard domain (half-plane, exterior of a circle, etc.), the number of geometries that can be transformed with analytic functions is relatively small. Considerable experience with the method is a necessity, and a heuristic approach is often required. Numerical methods can be used to transform the coordinates; however, if extensive programming is required, one of the other more versatile numerical techniques will probably be more efficient.

The two general numerical methods for obtaining accurate solutions are the finite difference and the finite element methods. Since relatively few electrochemical problems have been studied using either method, conclusions regarding the superiority of one of the methods for a given application are difficult to draw. The finite element method is based on a variational formulation.¹⁴ The problem reduces to finding the unknown functions which extremize a system of functionals. From the calculus of variations, it can be shown that these functions also satisfy the differential equations and their boundary conditions.

The domain of interest can be subdivided into discrete polygons. Some gain in computational efficiency and the ability to follow an irregular geometry appear to be the main advantages of this system.

In the finite difference method the differential equations are approximated by their difference formulations. The domain is generally divided into rectilinear elements; some approximation of the field variable must then be made at a curved boundary. While a large number of iterations may be required to solve a current distribution problem, the computer time per iteration is generally small. The finite difference method is generally easier to implement, and square elements, which are frequently employed, are ideally suited for computer manipulation.

Only a few direct comparisons of the two methods have been performed. There is little interest in solving problems numerically that have been solved analytically; conversely, those problems that do not have analytical solutions cannot be used to compare the accuracy of the two numerical methods. In one study Hohl and Hamilton¹⁵ used both methods to calculate one-dimensional, transient, diffusion profiles for which analytical solutions are available. Their results showed that the average error was lowest for the finite difference method; moreover, they found the computational efficiency of the finite difference method to be superior. The finite element method, however, showed less sensitivity to successive grid refinement.

One goal of this investigation was to develop general techniques to solve electrochemical moving boundary problems. Because of its flexibility, ease of implementation, and accuracy, the finite difference method was chosen as the basis of the solution technique. A general

kinetic expression and an approximate concentration overpotential relation are accommodated in the model. The calculation of the current distribution for the problems investigated requires a solution of Laplace's equation with nonlinear boundary conditions.

In principle, the volume encompassed by the boundaries of any electrochemical system can be divided into small elements. A grid can be defined by the junctures of the corners of the elements and by the intersections of the edges of the elements with the cell surface. On this grid the finite difference method is used to solve for the potential distribution. The current distribution is calculated by numerically differentiating the potential with respect to the normal to the surface, and the overpotential can be obtained from appropriate kinetic and concentration overpotential expressions. In some cases a converged solution can be realized by iterating over the equations describing the potential, current density, and overpotential. From a converged solution the new profile can be calculated by moving the profile coordinates in proportion to the local current density. A final profile is obtained by continued iteration for a specified number of discrete time steps.

There is no guarantee that a converged solution will always result at each time step. By appropriately weighting the surface potentials each time the current density is recomputed, I have devised an algorithm to overcome the computational instability that occurs when calculating the secondary or tertiary current distribution. Converged solutions have been obtained for all reasonable values of the physical parameters on the geometries studied. Although the techniques presented are

adaptable to three-dimensional systems, these studies are limited to two-dimensional and axisymmetric systems.

Because of the paucity of quantitative shape change data in the literature, I initiated a series of studies on contoured rotating cylinder electrodes with sinusoidal cross-sections. After depositing copper from an acid-copper electrolyte, final profile coordinates were obtained for comparison with simulated results.

"This incomprehensible art, which has been in use about three years, is truly valuable and must prevail extensively, notwithstanding the disadvantage to which its reputation has been subjected, in consequence of the many impositions practised on the public, by the unprincipled speculators."

from the article "Electro-Plating"
in The Scientific American, vol. 1,
no. 1, 1845.

2. MODEL

Description

In a general electrochemical system the potential distribution and concentration distributions of all reacting species must be known before the current distribution can be determined. Calculation of the concentration distributions depends in turn on the local hydrodynamic conditions. The local reaction rate of each species also depends on the polarization due to kinetic and mass transport limitations. If gas is evolved at an electrode, the bubbles tend to increase the local mass transport rate, but since they are less conductive than the electrolyte, the bubbles tend to increase the cell resistance. A general two-dimensional model which takes into account hydrodynamic variations, polarization, ohmic drop, mass transport limitations, simultaneous electrode reactions, and gas evolution would be extremely complicated and does not exist.

The model that I have developed accounts for electrode polarization, ohmic drop, and mass transport limitations for a large class of two-dimensional and axisymmetric cells. The mass transport limitations are treated through an approximate concentration overpotential expression, which is valid in an excess of supporting electrolyte where conductivity variations in the diffusion layer and the diffusion potential can be neglected. The hydrodynamics must be sufficiently well defined so that an effective mass transport boundary layer thickness can be estimated everywhere on the profile. An arbitrary kinetic expression can be used in the calculation of charge transfer overpotential.

The approach that I have taken is to treat the bulk electrolyte and the diffusion layer separately. Since the diffusion layer is relatively thin, the local current density entering the diffusion layer from the bulk must equal the current density entering the electrode. The current density in the bulk can be determined from Ohm's law, and the surface potential can be calculated from appropriate overpotential expressions. A solution to the current distribution problem can generally be obtained by iterating over the governing equations.

Equations

The bulk electrolyte is assumed to be well-stirred so that no concentration gradients are present, and Laplace's equation applies

$$\nabla^2 \phi = 0 \quad (1)$$

At the boundaries the normal current density is proportional to the potential gradient

$$\nabla_n \phi = -i_n / \kappa \quad (2)$$

The Butler-Volmer equation describes the dependence of surface potential on current density

$$i_n = i_o \left[\exp \left(\frac{\alpha_a F}{RT} \eta_s \right) - \exp \left(- \frac{\alpha_c F}{RT} \eta_s \right) \right] \quad (3)$$

The exchange current density may be a function of the surface ion concentration

$$i_o = i_{ob} (c/c_b)^\gamma \quad (4)$$

If linear concentration gradients are assumed

$$i_o = i_{ob} (1-i/i_1)^\gamma \quad (5)$$

For metal deposition in well-supported electrolyte, the concentration overpotential can be approximated by

$$\eta_c = \frac{RT}{nF} \ln (1-i/i_1) \quad (6)$$

The total overpotential η , which is comprised of surface overpotential and concentration overpotential, is defined by

$$\eta = V - \phi_o \quad (7)$$

The current is determined by integrating the normal current density over the electrode surface

$$I = \int_s i_n dA_n \quad (8)$$

The time increment for the electrode process is determined by dividing the specified charge passed by the current

$$\Delta t = Q/I \quad (9)$$

The boundary of the electrode surface progresses in proportion to the normal current density at each surface node

$$H_n = \frac{M}{zF\rho} i_n \Delta t \quad (10)$$

Sir, spare your threats:

The bug which you would fright me with I seek.

The Winter's Tale, III, ii

3. NUMERICAL PROCEDURE

The basic procedure to calculate successive profiles is as follows:

1. Specify boundary coordinates, physical properties, polarization parameters, grid spacing, convergence criterion, and time step size.
2. Estimate the initial potential distribution.
3. Construct piecewise polynomials through the boundary points so that derivatives at the surface can be calculated.
4. Obtain a loosely converged estimate of the solution to Laplace's equation. Tighten the convergence criterion as the iteration proceeds.
5. Calculate the normal current density by numerically differentiating the potential at each surface node.
6. Determine the overpotential from the polarization equation.
7. Calculate the surface potential from equation 7; weight this value with the value obtained from the previous iteration. If the potentials and currents meet the convergence criteria, proceed to step 8. Otherwise, continue iteration at step 4.
8. Move each surface node normal to the surface in proportion to the charge passed.
9. Construct interpolating polynomials to determine the new ordinates at evenly spaced abscissa points.

For the primary current distribution Laplace's equation need only be solved one time, and step 7 is eliminated.

Computational Techniques

The grid network for the electrode with a sinusoidal cross-section is depicted in Fig. 1. The finite difference method, coupled with successive-overrelaxation, is used to calculate the potential distribution in the bulk. Based on Fleck's⁴ results that an overrelaxation parameter of 1.8 to 2.0 gave the greatest computational efficiency, I use 1.85. A method outlined in Lapidus¹⁶ is used to approximate the potential at nodes adjacent to the surface (see Appendix F).

A three point numerical differentiation formula is used to calculate the current density at each surface node (see Appendix B and Appendix H). The electric field normal to the surface is calculated from the projections of the X and Y components on the normal as shown in Fig. 2.

$$E_n = E_x \sin \theta + E_y \cos \theta \quad (11)$$

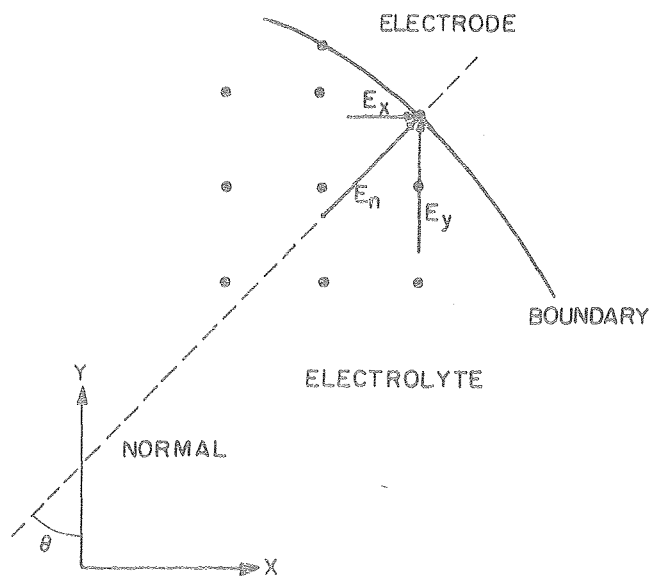
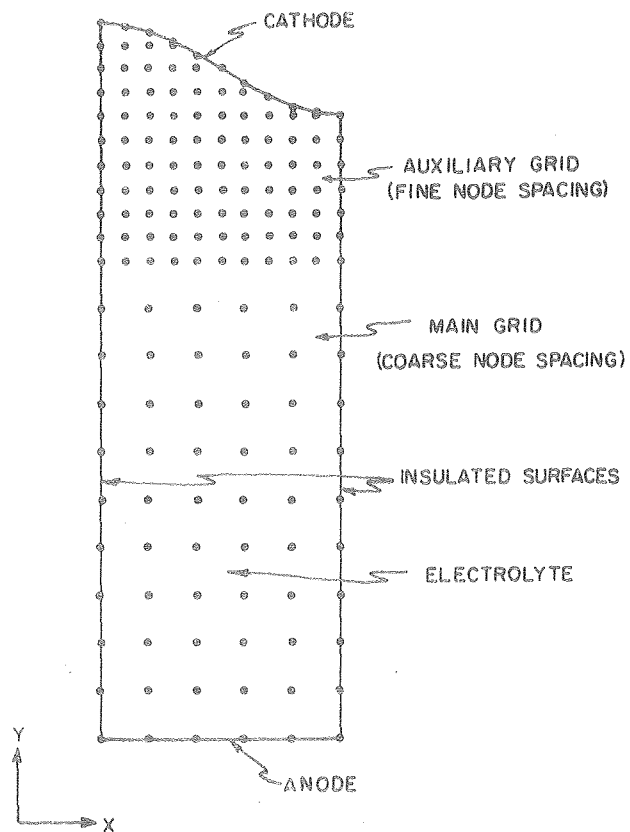
The current density at the surface is the product of the conductivity and the field

$$i_n = \kappa E_n \quad (12)$$

This approximation for the current density at the r th iteration is substituted in the Butler-Volmer equation to get an estimate of the overpotential. The overpotential appears in a transcendental expression, and an explicit solution cannot be obtained. The Newton-Raphson method is most efficient for obtaining the overpotential (see Appendix I). Alternatively, if the entire profile is in the Tafel or linear region, the overpotential can be obtained explicitly. The concentration overpotential calculated explicitly from equation 6, can be added to the

Fig. 1. Schematic diagram of node arrangement for simulation of deposition or dissolution on a sinusoidal electrode.

Fig. 2. Projection of the normal components onto the line perpendicular to the electrode.



XBL 809-5896A

Figs. 1-2

surface overpotential, and the surface potential is obtained from equation 7.

A new estimate of the surface potential is

$$\phi_o^{(r+1)} = \phi_o^{(r-1)} + D (\phi_o^{(r)} - \phi_o^{(r-1)}) \quad (13)$$

where D is a weighting factor which varies between 0 and 1. The surface potentials are checked for convergence before the weighting procedure is performed. When the surface potentials meet the convergence criterion, the weighting factor is reduced on successive iterations until the normalized change in current density between iterations also meets the specified error criterion.

The new coordinates of the j th point on the boundary are

$$X_j^{(s)} = X_j^{(s-1)} + \frac{M\Delta t}{zF\rho} |i_n|_j \sin \theta_j \quad (14)$$

$$Y_j^{(s)} = Y_j^{(s-1)} - \frac{M\Delta t}{zF\rho} |i_n|_j \cos \theta_j \quad (15)$$

The interpolating polynomials of the cubic spline described in Ahlberg et al,¹⁷ are used to interpolate back to the original abscissa coordinates ($X_j^{(s-1)}$). The piecewise cubic polynomials that uniquely specify the curve have the following properties: (1) The polynomials on either side of each surface node intersect at that node; (2) the first derivatives are continuous at each node; (3) the second derivatives are continuous at each node. If the profiles tend toward discontinuous behavior (sharp points or cusps), least squares smoothing can be performed on the $X_j^{(s)}$, $Y_j^{(s)}$ coordinates before interpolating.

A dimensionless number useful in characterizing the secondary current distribution is the Wagner number

$$W = \frac{\kappa \left(\frac{\partial \eta_s}{\partial i} \right)_{i_{av}}}{L} \quad (16)$$

For the primary current distribution the Wagner number is zero. As W increases, a more uniform current distribution is obtained. The characteristic dimension of the system L is generally taken to be the distance over which the profile disturbs the field.

Convergence Procedure

In order to obtain a converged solution, a judicious choice of the factor D in equation 11 must be made. A value of D equal to one implies direct substitution. For small values of W (less than 0.1), a value of D equal to one will generally lead to a converged solution; however, for larger values of W , the oscillatory behavior of the surface potentials may lead to instabilities. Intuitively, one might expect that a converged solution could always be obtained if one were to choose a sufficiently small value of D . One would like to choose a value of D that is small enough to avoid oscillatory instabilities yet large enough to avoid an excessive number of iterations. Such an optimum choice is difficult to make a priori.

Rather than choosing a constant value for D , I have devised an algorithm from which a value for D is calculated each time the surface potential is re-evaluated. In this programmed weighting algorithm the value of D is dependent on four variables: (1) the consistency

of the direction of change of the surface potential at a specified point; (2) the normalized change in current density between iterations; (3) the normalized change in surface potentials between iterations; (4) the Wagner number.

The evaluation of the current density requires a numerical differentiation of the potentials in the bulk electrolyte (equation 2). Since this numerical differentiation is sensitive to small changes in bulk electrolyte potentials, loose convergence (10^{-4}) in the bulk potentials is specified before evaluating the current densities. As a converged solution is approached, and the relative change in surface potentials decreases, the convergence criterion that must be attained before evaluating the current densities decreases. The overpotentials and surface potentials are determined from equations 3, 6, and 7. With the new values of the surface potentials, the relative change in these surface potentials from the previous iteration can be calculated. These changes give a measure of the convergence.

The four variables, noted above, are incorporated in functions to determine the weighting factor. If the surface potential at the specified node is proceeding in the same direction, this "consistency factor" is increased. If this surface potential begins to oscillate, the consistency factor is reduced; large oscillations indicate incipient instability. Small oscillations frequently indicate an approach to convergence. The "current factor" is increased if the average normalized change in current density is smaller than specified limits; the current factor is reduced if the change is large. The limits are functions of the Wagner number and the consistency factor. The normalized change

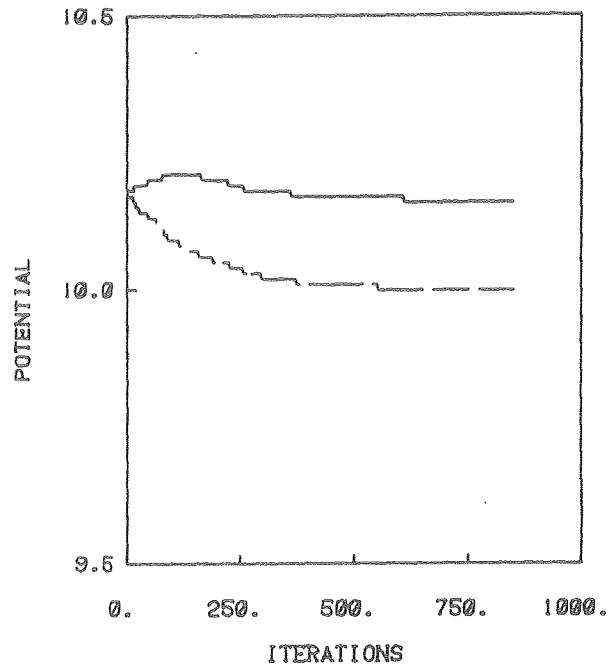
in surface potential indicates the degree of convergence. As this variable approaches the convergence criterion, the weighting factor is reduced. When the weighting factor is reduced sufficiently, the average current error also decreases until the error criterion for that variable is also met. The behavior of the surface potentials, the maximum normalized change in surface potentials, the average normalized change in current density, and the weighting factor are illustrated in Figs. 3, 4, 5, and 6, respectively, for a problem involving deposition on a sinusoidal profile at $W = 25$ for the first time step.

For the problems solved, I selected normalized convergence criteria of 10^{-6} , 10^{-5} , and 10^{-3} , for the bulk potentials, the current densities, and the surface potentials, respectively. The algorithm is sufficiently general so that converged solutions are obtainable over a wide range of Wagner numbers (see Fig. 7). In the first time step the relatively large number of iterations, attributable to poor initial estimates, could be reduced by improving those estimates.

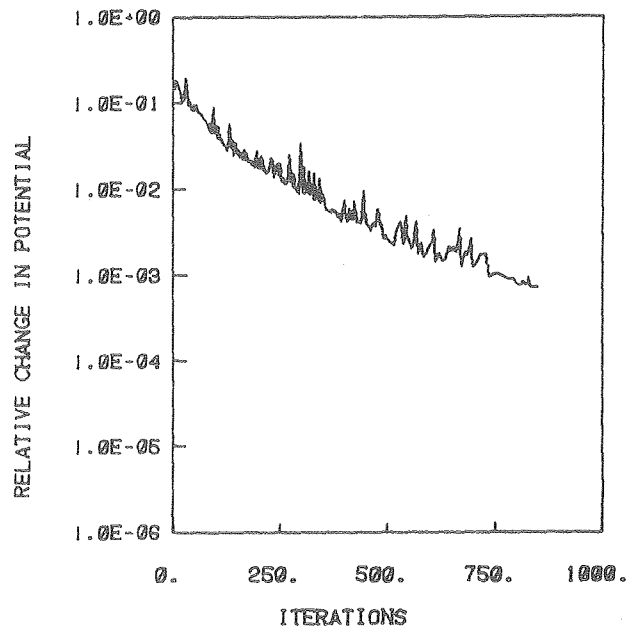
The results of the programmed weighting algorithm are compared with the results of selecting a value for D a priori for $W = 25$ (Fig. 8). This graph illustrates the difficulty of choosing the optimum value for D . A small value (10^{-3}) for D results in a rather efficient computation for the second time step, but the first time step requires five times as many iterations as the programmed weighting technique. A value of D greater than 2×10^{-3} causes oscillations during the second time step, and convergence to the specified criteria does not occur. For this problem converged solutions for the two time steps will always be

Fig. 3. Surface potential at the peak and in the depression (dashed) of a sinusoidal profile. $A_o/\lambda = 0.1$, $W = 25$, time step one, $V_c = 1$, $V_a = 11$.

Fig. 4. Normalized maximum change in surface potential. Parameters as in Fig. 3.



SURFACE POTENTIAL AT PEAK AND IN THE DEPRESSION (DASHED)
W = 25, TIME STEP 1.



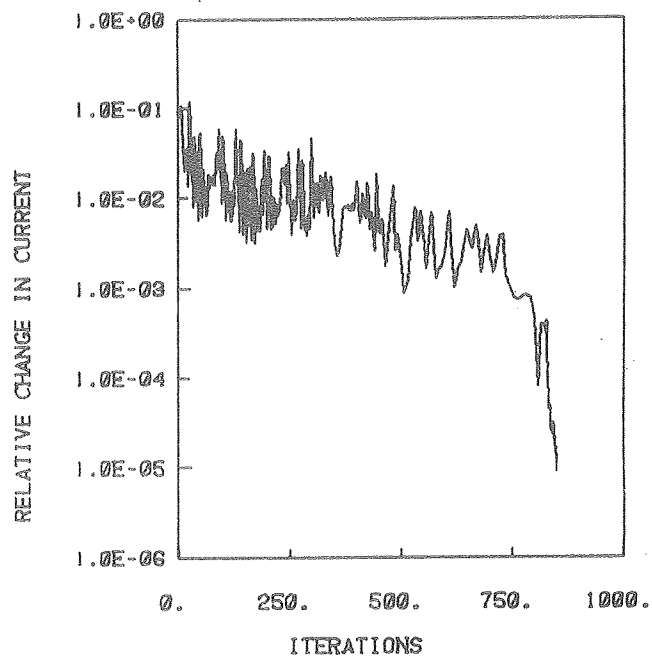
NORMALIZED MAXIMUM CHANGE IN SURFACE POTENTIAL,
W = 25, TIME STEP 1.

XBL 804-9376A

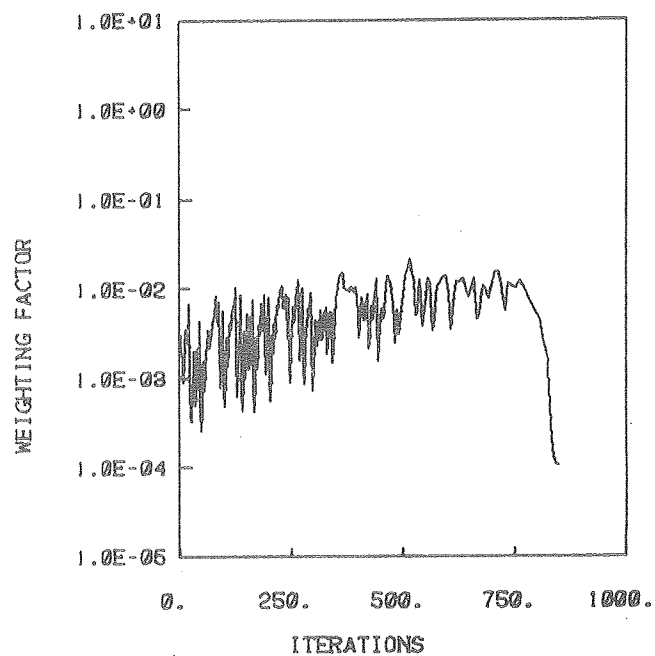
Figs. 3-4

Fig. 5. Normalized average change in current density. Parameters as in Fig. 3.

Fig. 6. Weighting factor for surface potentials. Parameters as in Fig. 3.



NORMALIZED AVERAGE CHANGE IN CURRENT DENSITY,
W = 25, TIME STEP 1.



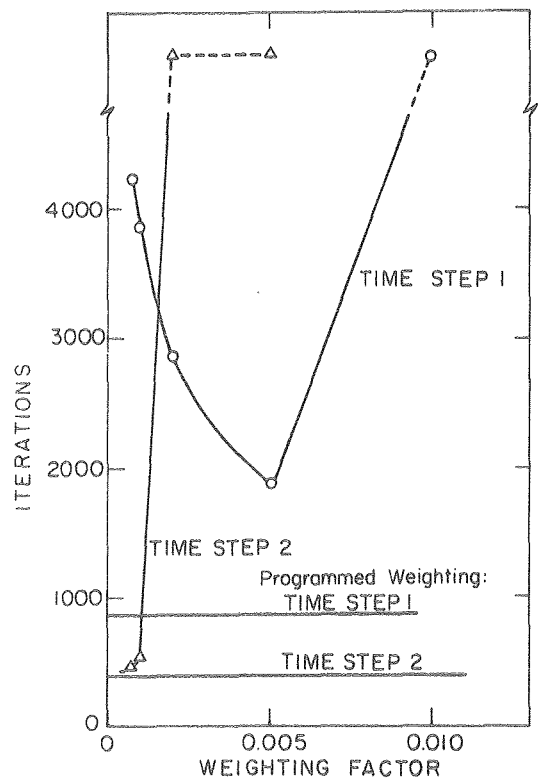
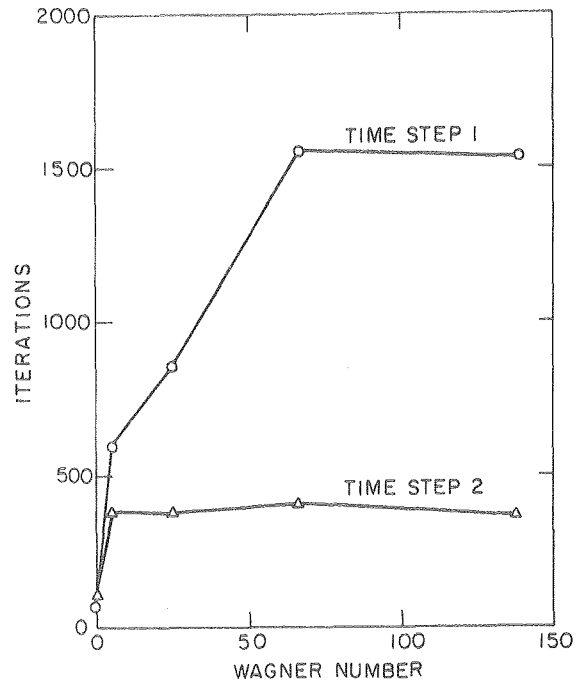
WEIGHTING FACTOR FOR SURFACE POTENTIALS,
W = 25, TIME STEP 1.

XBL 804-9374A

Figs. 5-6

Fig. 7. Iterations required for a converged solution as a function of the Wagner number.

Fig. 8. Iterations required for a converged solution as a function of the weighting factor. Iterations required for convergence when using the programmed weighting technique are indicated by the solid horizontal lines.



XBL803-4768A

Figs. 7-8

obtained more quickly by using the programmed weighting algorithm than by using the optimum constant value for D of approximately 10^{-3} .

The functions and parameters that comprise the convergence algorithm have been determined by empirical methods and have not been optimized; the algorithm could undoubtedly be improved by making a systematic study of these functions and parameters. For example, one could study the overrelaxation parameter. Although I used 1.85 for this parameter, Fig. 9 shows that the number of iterations in the first time step ($W = 25$) could be reduced by almost 10 percent by using 1.8 for this parameter. It is not known whether this is a general result which would apply to other problems with other Wagner numbers. The criteria for determining how frequently to iterate in the current loop relative to the potential loop would probably be a fruitful area for an optimization study. Multiple iterations in the current loop for each iteration in the potential loop might be investigated. The average normalized change in current density is allowed to vary by approximately 5 to 10 percent. Possibly these limits could be increased under certain circumstances without causing unstable behavior.

Error Estimates: General Considerations

The approximation of replacing the electrolyte continuum by square elements results in finite error in the potential values. In general, the accuracy of the solution improves as the mesh size is reduced. Quantitative estimates of the error caused by selecting a certain mesh size are difficult to determine a priori. The expression to calculate the error (truncation error) associated with using the finite difference scheme which I have chosen is well known.¹⁷ The

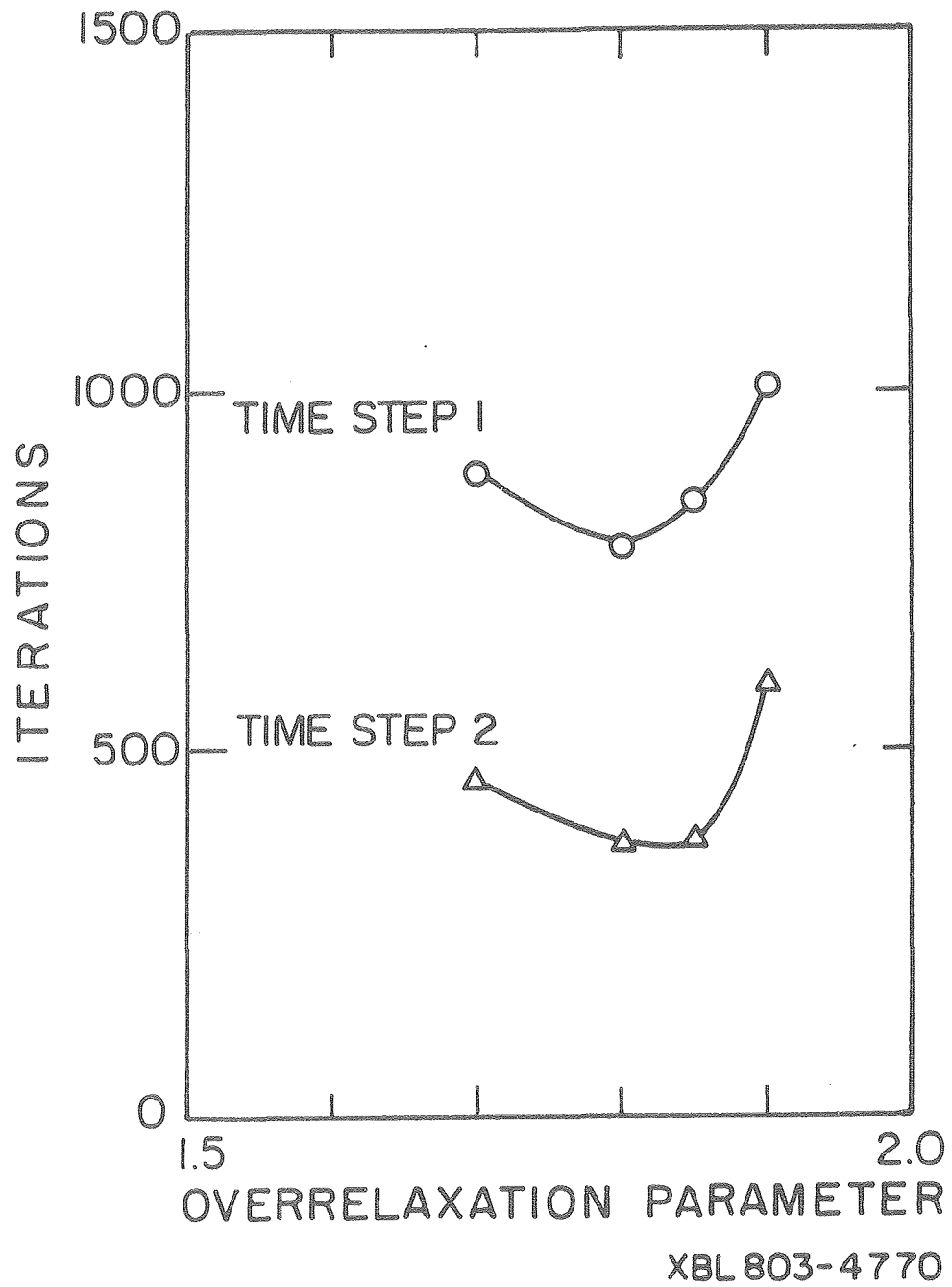


Fig. 9. Iterations required for convergence vs. the overrelaxation parameter.

truncation error is proportional to the mesh interval squared and to the fourth derivative of the potential function in the region of interest. Since the variation in the potential function is not known a priori, it is generally impossible to calculate the error.

The error in the potential is also related to the maximum residual in the final iteration in the potential loop. The maximum permissible residual (the convergence criterion) is specified in advance. The accuracy of the solution will increase up to a limit as the convergence criterion is reduced. After further reduction the truncation errors will dominate the solution accuracy; at some point the round-off error in the computer (10^{-14} with single precision in the CDC 7600) becomes larger than the convergence criterion, and convergence to a smaller residual cannot be attained.

From the potential distribution the current density is determined by numerically differentiating the potential at the electrode surface. Because potential values at least one grid space away from the surface are used in the numerical differentiation, the estimate of the current density improves as the grid spacing is reduced.

The size of the time step influences the shape of the final profile. The error in the quasi-steady state approximation should decrease as the number of time steps for a given amount of charge passed is increased. The boundary ordinates must be interpolated back to the original abscissa coordinates at each time step; therefore, I expect that there is an optimum number of time steps, beyond which the cumulative interpolation error overshadows the increased accuracy realized from reducing the quasi-steady state error.

At each time step the normal to the surface is determined from a numerical differentiation of the surface coordinates. The error associated with the differentiation process decreases as the grid interval is reduced.

If the profile tends toward unstable behavior (e.g., a primary distribution near a sharp corner), least squares smoothing can be performed to reduce the instability. By specifying the maximum root-mean-square (rms) error in the polynomial curve with respect to the generated coordinates, a polynomial equation of an appropriate degree can be determined. As the rms error specification is increased, the degree of the polynomial is reduced, along with the accuracy of the solution. A sufficiently small rms specification will force the polynomial curve to pass near each point, and little smoothing is achieved.

Although the error in our solution cannot be determined a priori, it is clear from the foregoing discussion that by reducing the grid spacing, convergence criterion, and time step interval (the computation parameters), a more accurate solution is likely to be obtained. The disadvantage in arbitrarily reducing grid spacing and time step interval is that the execution time in the computer increases (roughly, as the inverse cube of mesh size and inversely with time step interval).

In order to establish criteria useful in determining the computation parameters, I ran a number of simulations on sinusoidal profiles of various amplitude-to-wavelength ratios. Since I am attempting to simulate real systems, there is no justification for attempting to obtain solutions of accuracy greater than the accuracy to which parameters in the model are known. By varying the computation parameters, I determined maximum

limits where the final profile did not change by more than a specified criterion on successive refinements. I considered that the solution had converged if the profile did not change by more than 2 percent at each point, based on the simulated metal thickness at that point.

Qualitatively, one expects more irregular profiles to require more refined grids. In regions where the current or the electrode curvature is changing rapidly, an increased node density is required to track these relatively rapid changes.

Mesh Size

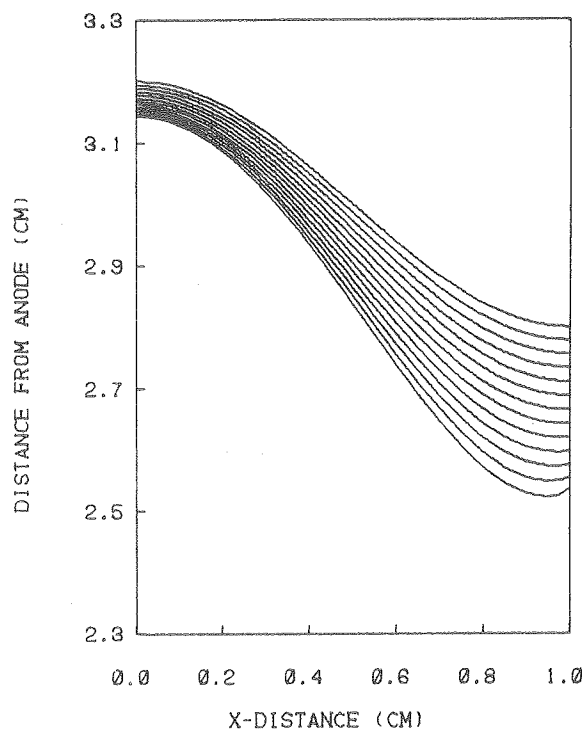
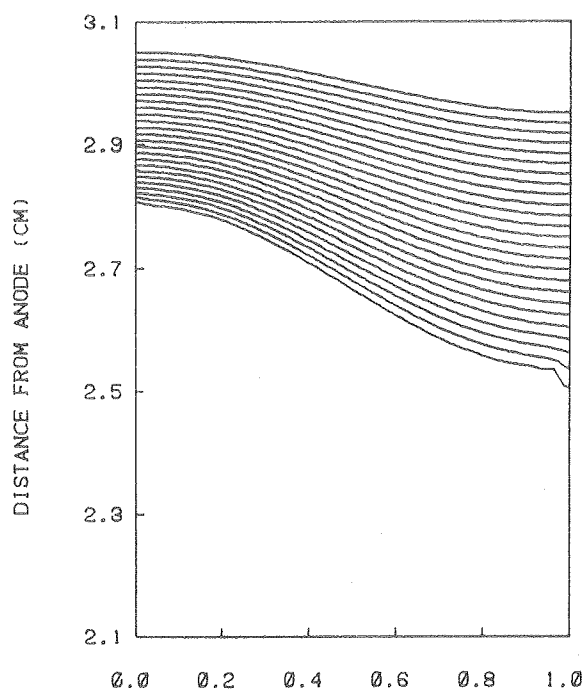
Two quantities that can be determined more accurately by reducing the mesh size are the current densities at the electrode surface and the derivatives of the surface coordinates. One cannot determine the accuracy of the current densities a priori, but one expects that the current densities will approach values where further refinement does not significantly affect the final profile.

I studied profiles with amplitude to wavelength (A/λ) ratios of 0.025 and 0.1. Simulations of deposition on these profiles with A/λ of 0.025 and 0.1 are shown in Figs. 10 and 11, respectively. The top curve depicts the original half-wavelength of the profile. The successive time steps are shown below with the final profile at the bottom. By successively refining the mesh size and observing the effect on the final profile after the passage of a specified quantity of charge, I can estimate the minimum refinement necessary to obtain an accurate solution.

For the sinusoidal profiles studied, the peak of the profile exhibited a characteristic type of unstable behavior, which depended

Fig. 10. Half-wavelength of a sinusoidal cathode. The original profile is shown at the top. The final profile appears at the bottom, and the intermediate growth stages are in between $W = 0$, $A_0/\lambda = 0.025$.

Fig. 11. Half-wavelength of a sinusoidal cathode. $W = 0$, $A_0/\lambda = 0.1$. Other details as in Fig. 10.



XBL 809-11778A

Figs. 10-11

on the initial A/λ ratio. When the initial profile is relatively flat ($A/\lambda = 0.025$), the peak tends to become pointed after the passage of a specified quantity of charge. For the high A/λ ratio (0.1) case, a depression forms at the peak after the profile advances to a certain point. The point at which this characteristic behavior is displayed is a logical point to halt the simulation.

In order to put the charge on a dimensionless basis, I defined the quantity of charge passed that would cause a plane electrode that is λ wide to advance one amplitude A

$$Q_d = A\lambda \frac{zF_0\Delta s}{M} \quad (17)$$

where Δs is a unit strip width perpendicular to the page (see Fig. 10 or 11). I chose values of the physical parameters that pertain to copper

$$Q_d = 2.7 \times 10^4 A\lambda \quad (18)$$

A dimensionless quantity of charge can be defined by dividing the number of coulombs in the simulation (equation 9) by Q_d .

$$Q^* = Q/Q_d \quad (19)$$

Selected Y-coordinates of the profiles at $Q^* = 2.78$ (20 time steps in Fig. 10) and at $Q^* = 3.33$ (24 time steps in Fig. 10) are shown in Tables 1a and 1b, respectively. At time step 20 the peak ($X = 1.0$) has not yet begun to sharpen, and the relatively smooth curve can be adequately described by a grid spacing of 0.05 cm. After four additional time steps the peak becomes sufficiently irregular that even with a

Table 1. Effect of grid spacing on profile error, $A_0/\lambda = 0.025$;
 (a) $Q^* = 2.78$, (b) $Q^* = 3.33$.

$A/\lambda = 0.25$				
a) At $Q^* = 2.78$ $Q^* = 0.139/\text{Time Step}$				
Grid Space (cm)	Y(0)	Y(0.8)	Y(1.0)	% Deviation at Y(1.0) Based on Deposit Thickness
0.2	2.837	2.632	2.618	4.0
0.1	2.838	2.629	2.614	2.9
0.05	2.839	2.629	2.607	0.8
0.025	2.839	2.629	2.606	0.6
0.0125	2.839	2.629	2.604	
b) At $Q^* = 3.33$ $Q^* = 0.139/\text{Time Step}$				
Grid Space (cm)	Y(0)	Y(0.8)	Y(1.0)	% Deviation at Y(1.0) Based on Deposit Thickness
0.2	2.801	2.562	2.549	9.9
0.1	2.804	2.584	2.544	8.7
0.05	2.804	2.557	2.529	5.3
0.025	2.805	2.557	2.526	4.7
0.0125	2.808	2.557	2.505	

grid spacing of 0.025 cm the error cannot be limited to less than 2 percent of the simulated deposit thickness. Similarly, in Table 2, before the depression develops, a grid spacing of 0.025 cm keeps the error within acceptable limits. After the depression at the peak develops, the 0.025 cm mesh spacing is too coarse to limit the error to 2 percent of the simulated deposit thickness.

Another indication of the accuracy of the numerical techniques is the error in the derivatives at the electrode surface. Since the initial profile is described by a sine wave, the error can be determined in the numerically computed derivatives. The relative error in the derivatives is on the order of 0.1 percent for a mesh size of 0.2 cm, and 0.005 percent for a mesh size of 0.1 cm (Table 3).

From these studies on successive grid refinements, I can propose guidelines for the maximum mesh size which produces a satisfactory simulation. I have chosen to examine the variations in current density and surface derivatives in order to establish the mesh size criterion. At $Q^* = 0.31$ for $A/\lambda = 0.1$, the variations in current density from node to node never exceed 10 percent, and the absolute change in derivative does not exceed 0.1. At $Q^* = 0.41$ the variation in current density is over 30 percent, and the derivatives change by 0.3 near the peak. I estimate from these studies that variations in the current density should not exceed 15 percent, and the absolute variations in the surface derivatives should not exceed 0.15 between adjacent nodes.

Table 2. Effect of grid spacing on profile error, $A_0/\lambda = 0.1$;
 (a) $Q^* = 0.31$, (b) $Q^* = 0.41$.

$A/\lambda = 0.1$				
a) At $Q^* = 0.31$		$Q^* = 0.034/\text{Time Step}$		
Grid Space (cm)	Y(0)	Y(0.8)	Y(1.0)	% Deviation at Y(1.0) Based on Deposit Thickness
0.1	3.154	2.637	2.602	3.9
0.05	3.155	2.641	2.601	2.4
0.025	3.155	2.643	2.597	1.5
0.0125	3.155	2.643	2.594	
b) At $Q^* = 0.41$		$Q^* = 0.34/\text{Time Step}$		
Grid Space (cm)	Y(0)	Y(0.8)	Y(1.0)	% Deviation at Y(1.0) Based on Deposit Thickness
0.1	3.143	2.556	2.535	6.0
0.05	3.144	2.568	2.546	5.9
0.025	3.143	2.570	2.536	2.2
0.0125	3.143	2.572	2.530	

Table 3. Comparison of analytical and numerical values of derivatives at the electrode surface for $A/\lambda = 0.1$.

X-Coordinate	Analytical Value	0.2 Grid Spacing (% Error)	0.1 Grid Spacing (% Error)
0.1	-0.194161	--	0.006
0.2	-0.369316	0.11	0.004
0.4	-0.597567	0.9	0.006
0.5	-0.628319	--	0.006

Convergence Criterion

As the convergence criterion is reduced, more accurate results are expected; however, there is no reason to reduce the convergence criterion past the point where other errors dominate the result.

In order to determine the maximum convergence criterion, an expression can be derived for the error as a function of the mesh size, which has been specified based on other considerations. First, an order of magnitude value for the current can be calculated

$$i_{\text{est}} = \frac{\kappa \Delta V_{\text{cell}}}{Y_{\text{cell}}} \quad (20)$$

where ΔV_{cell} is an approximate anode-cathode potential difference. For the primary distribution this is the applied potential difference. For other current distributions the methods of appendix J are suitable for determining ΔV_{cell} . ΔY_{cell} is the maximum anode-cathode separation. An estimate of the potential difference between the nodes is

$$V_{\text{node}} = \frac{i_{\text{est}} \Delta Y_{\text{node}}}{\kappa} \quad (21)$$

or

$$V_{\text{node}} = \frac{\Delta V_{\text{cell}} \Delta Y_{\text{node}}}{\Delta Y_{\text{cell}}} \quad (22)$$

V_{node} can be normalized by dividing by the node potential

$$V_{\text{node}} = \phi_o + \Delta V_{\text{node}} \quad (23)$$

and

$$\frac{\Delta V_{\text{node}}}{V_{\text{node}}} = \frac{\Delta V_{\text{cell}} \Delta Y_{\text{node}}}{(\phi_o + \Delta V_{\text{node}}) \Delta Y_{\text{cell}}} \quad (24)$$

where ϕ_0 is the potential adjacent to the cathode in the low current density region. The error in $\Delta V_{\text{node}}/V_{\text{node}}$ is roughly proportional to the error in the current density. For the primary distribution on the $A/\lambda = 0.1$ sinusoidal profile and 0.025 cm mesh spacing

$$\frac{\Delta V_{\text{node}}}{V_{\text{node}}} = \frac{(10 \text{ V}) (0.025 \text{ cm})}{(1 \text{ V} + 0.07 \text{ V}) (3.2 \text{ cm})} = 0.07 \quad (25)$$

If we want to limit the current density error, due to the residual, to 0.01 percent, then the convergence criterion should be no larger than $(0.001) (0.07) = 7 \times 10^{-5}$.

The results of successively increasing the convergence criterion are shown in Table 4. The maximum difference in the current density at the first time step increases by roughly an order of magnitude as we increase the convergence criterion by an order of magnitude. The current densities can be normalized with respect to an average current density, and a comparison of these results can be made as the convergence criterion is increased. The relative errors are shown in the third column in Table 4. These errors are lower than those from comparing the current densities directly. Because of the constraints imposed by the network, the current densities tend to shift in a somewhat uniform manner. Because of this phenomenon, a slightly larger convergence criterion can be used, and a satisfactory result can still be obtained. Table 5 shows how the change in convergence criterion affects the final profile. The final profiles with a convergence criterion of less than 10^{-3} are within 0.1 percent of the curve obtained with a convergence criterion of 10^{-6} . The errors caused by specifying a 10^{-2} convergence

Table 4. Effect of convergence criterion on error in current distribution.

Convergence Criterion	Maximum Error in Current Density	Relative Error in Current Density*
10^{-5}	0.14	0.03
10^{-4}	1.5	0.3
10^{-3}	4.9	1.4
10^{-2}	34.0	20.0

*Errors in the current density caused by successive increases in the convergence criterion. Deviations are based on a convergence criterion of 10^{-6} .

Table 5. Effect of convergence criterion on profile error.

At $Q^* = 0.41$; $A/\lambda = 0.1$			
Convergence Criterion	$Y(0)$	$Y(0.8)$	$Y(1.0)$
10^{-6}	3.143	2.570	2.536
10^{-5}	3.143	2.571	2.536
10^{-4}	3.143	2.571	2.536
10^{-3}	3.143	2.570	2.536
10^{-2}	Unstable		

criterion are too large, and an unstable curve results. The number of iterations increases by a factor of 10 as the convergence criterion is reduced from 10^{-3} to 10^{-6} .

Time Step Interval

I assume that the current distribution does not significantly vary during the interval which I select as the time step size. Clearly, this quasi-steady state approximation becomes more accurate as the time step interval is reduced. In order to obtain a better approximation, the current distribution can be calculated at two successive time steps, the current densities averaged, and the profile advanced in proportion to half the quantity of charge specified. This method would approximately double the computation time, so I have not used this technique.

Because of the errors inherent in the interpolation of the coordinates back to the original abscissa values, I expect to reach a lower time interval limit, below which the error of the interpolation will dominate the result, and further improvement in the accuracy will not be realized. In Table 6 the results of successively decreasing the time step interval are summarized. From Table 6a it can be seen that the profile accuracy is not significantly improved when reducing the step size interval by a factor of four. As the irregularity at the peak develops, the time step interval equivalent to 0.034 is no longer sufficient to give an accurate result.

Since the mesh size is determined by the irregularity of the geometry and the variation in current density, it is reasonable to base the time step interval on the mesh size. At $Q^* = 0.068$ per time

Table 6. Effect of time step on profile error; (a) $Q^* = 0.34$,
(b) $Q^* = 0.41$.

a) Profile Coordinates at $Q^* = 0.34$; $A/\lambda = 0.1$				
Time Step Interval (Q^*)	Y(0)	Y(0.9)	Y(1.0)	Maximum % Deviation
0.068	3.150	2.580	2.574	1.3
0.034	3.150	2.578	2.575	0.4
0.017	3.151	2.577	2.576	
b) Profile Coordinates at $Q^* = 0.41$; $A/\lambda = 0.1$				
Time Step Interval (Q^*)	Y(0)	Y(0.9)	Y(1.0)	Maximum % Deviation
0.068	3.142	2.531	2.530	7.1
0.034	3.143	2.528	2.537	4.4
0.017	3.143	2.525	2.548	

step, the profile advances a maximum of approximately 0.05 cm, which is twice the maximum required mesh spacing. Since the current distribution is known before advancing the profile, the maximum change can be restricted to the two grid space criterion.

Smoothing

The simulation of a deposition process is inherently unstable in the sense that small errors at a point tend to be cumulative and are magnified as the simulation progresses. For example, if, through a small error, a local peak forms on the electrode surface in the simulation, that peak tends to attract more current and becomes even larger. In the dissolution process, by contrast, the additional current attracted by a similar local peak tends to dissolve the peak back to the average surface plane, and propagation of the error does not occur.

In order to lessen the tendency of unstable behavior of the surface profile, smoothing of the coordinates can be performed. I have chosen least squares polynomial smoothing, which is a straightforward and well-known technique. One can specify either the degree of the polynomial or the rms error. I chose to specify the rms error from which the minimum polynomial degree is computed. For highly irregular curves or those with separate distinctive features, multiple polynomial equations can be generated and spliced together.

It is reasonable to specify the rms error as a fraction of the grid spacing, on which the maximum advance of the profile also depends. I can estimate this criterion based on the results in Table 7. The cubic equation that is obtained with an rms smoothing greater than 10 microns (the profile advances approximately 200 microns/time step

Table 7. Effect of least squares smoothing on profile error.

a) Profile Coordinates at $Q^* = 0.34$; $A/\lambda = 0.1$				
Rms Error (cm)	Polynomial Degree	Y(0)	Y(0.9)	Y(1.0)
1×10^{-2}	3	3.143	2.581	2.575
5×10^{-3}	3	3.143	2.581	2.575
1×10^{-4}	3	3.143	2.579	2.575
5×10^{-4}	5	3.150	2.579	2.575
2×10^{-4}	5	3.151	2.578	2.576
1×10^{-5}	10	3.150	2.581	2.585
No Smoothing	32*	3.150	2.574	2.577
b) Profile Coordinates at $Q^* = 0.41$; $A/\lambda = 0.1$				
Rms Error (cm)	Polynomial Degree	Y(0)	Y(0.9)	Y(1.0)
1×10^{-2}	3	3.133	2.532	2.528
5×10^{-3}	3	3.133	2.532	2.528
1×10^{-3}	3	3.133	2.532	2.528
5×10^{-4}	6	3.143	2.527	2.534
2×10^{-4}	12	3.143	2.528	2.536
1×10^{-4}	17	3.144	2.528	2.546
1×10^{-5}	32*	3.144	2.537	2.582
No Smoothing		3.143	2.551	2.562

* Not fit to specific criterion because of other constraints.

at the peak) is not sufficient to describe the actual profile, and the profile near $X = 0$ is distorted. Smoothing between 1 micron and 5 microns gives acceptable results. Table 7b shows that the extent of the depression is reduced significantly as the rms error criterion is increased. Some judgment is required to decide whether curves should be subdivided so that smoothing over a specific feature can be accurately performed.

In this study smoothing between 0.5 and 2 percent of the grid space size gives the best results. Without smoothing, at $Q^* = 0.41$ the absolute change in the derivatives is greater than 3 between adjacent nodes. With 2 micron smoothing the change in derivatives is 0.5 at the peak.

Summary of Error Criteria

I have estimated criteria (see Table 8) for determining the calculation parameters that are based on empirical results. The mesh size is first selected on the basis of the relative change in current density and absolute change in surface derivative values. Relatively fine meshes are required for highly irregular geometries. The time step size and the convergence criterion can be estimated from the grid spacing. Some smoothing may be required for highly irregular profiles or if thick deposits are to be simulated.

Table 8. Error criteria guidelines.

Parameter	Limit
Grid Spacing	Less than 0.15 absolute difference in derivative and less than 15 percent relative change in current density between successive surface nodes
Time Step Size	Less than 2 grid spaces
Convergence Criterion	See Equation 23, less than 0.1 percent of the relative potential change between adjacent nodes
Smoothing	Greater than 0.5% of the grid space and less than 2% of the grid space

"Never hesitate to perform an experiment, for fear of learning something new."

C. W. Tobias, general admonition
to graduate students

4. EXPERIMENTAL PROGRAM

Introduction

An experimental program was initiated to obtain data on the growth of electrodeposited profiles. The contoured rotating cylinder system was chosen primarily because it offered a uniform hydrodynamic boundary layer. Since the system is axisymmetric, a simulation can be reduced to a two-dimensional problem. The acid-copper system provided high current efficiency, simple ion discharge, and acceptable deposits.

Selection of Operating Parameters

Initial trials were aimed at determining a range of operation where quantitative profile data could be obtained. Thick deposits (~ 1 mm) obtained near the limiting current tended to be rough and unsuitable for measurement. In general, operation at low fractions of limiting current ($\sim 20\%$) and at low current density (~ 30 mA/cm²) favored smooth deposits.

Eisenberg et al.¹⁸ established a correlation for the limiting current density on smooth rotating cylinder electrodes in turbulent flow

$$i_l = 0.791 n F c_b v \text{Re}^{-0.3} \text{Sc}^{-0.644} \quad (26)$$

or

$$i_l = 0.791 n F c_b v^{0.7} d_i^{-0.30} v^{-0.344} D_m^{0.644} \quad (27)$$

Since the limiting current density increases in proportion to the bulk reactant concentration (c_b) and as the 0.7 power of the surface velocity (v), the highest practical copper sulfate concentration and a high rotation speed are desired. A rotation speed on the order

of 800 rpm was sufficiently high to maintain a high limiting current density ($\sim 350 \text{ mA/cm}^2$), yet low enough to avoid operational difficulties with vortex formation and bubble entrainment. The copper sulfate concentration ($\sim 0.8 \text{ M}$, at 25°C) was chosen to be sufficiently far from the saturation limit to avoid precipitation at the anode. Large ohmic losses were avoided by adding supporting electrolyte ($\sim 1 \text{ M H}_2\text{SO}_4$).

An operating temperature of 25°C was convenient, and most physical property and polarization data were available at that temperature. Experiments were run at temperatures of 40°C and 55°C , but no particular advantages to operating in this range were noted. The slope of the polarization curve decreases with temperature. This may be caused by an increase in the cathodic transfer coefficient (α_c) or it may be that the exchange current density is actually larger than that calculated, and the data were not obtained in the Tafel region. With increasing temperature, electrolyte conductivity increases, while the slope of the polarization curve decreases; because of these countervailing tendencies, the range of the Wagner number cannot be significantly expanded by varying temperature alone.

In order to avoid roughness and still operate at high current densities, a leveling agent was tested. In several runs with 10^{-3} M benzotriazole at a current density on the order of 100 mA/cm^2 , the deposit was stressed and peeled from the substrate.

The Cu^+ species exists in small equilibrium quantities with the dominant Cu^{++} species. Only the Cu^+ species can react with dissolved oxygen and thus deplete the electrolyte of reactant. In order to avoid reactant depletion, the dissolved oxygen was removed by sparging

the electrolyte with nitrogen gas. In addition, a nitrogen blanket was maintained over the electrolyte during each run. In order to check for oxide precipitation, the anode weight loss and cathode weight gain were measured after each of several runs. The anode weight loss was never more than 3% greater than the cathode weight gain. Within the experimental accuracy of the current integration system, the current efficiency was 100%.

Equipment

A schematic of the experimental apparatus is shown in Fig. 12. A model 6259B Hewlett-Packard regulated power supply provided constant cell potential through feedback sensors connected directly to the cell. The copper reference electrode potential was measured with a model 610 Keithley electrometer. A Princeton Applied Research model 379 digital coulometer continuously monitored the charge passed. A one-half hp variable speed motor and controller, manufactured by Minarik, were used to rotate the cylindrical electrode at constant speed (± 5 rpm).

The cell was custom built from type 316 stainless steel on the inside. An outer brass jacket permitted continuous water circulation for temperature control. The upper and lower cell surfaces were machined from Lucite. The cell dimensions are 13.7 cm inside diameter by 16.8 cm high, and the volume of electrolyte contained in the cell is approximately 2.5 L. A stainless steel shaft connected the motor to the rotating electrode. The current was conducted through finger contacts to an Everdur collar. The anode was rolled from 1/16-in. OFHC sheet stock and was press-fitted into the cell. A glass capillary, positioned

Fig. 12. Schematic of experimental apparatus. A) power supply, B) coulometer, C) shunt for current measurement D) finger contacts, E) motor, F) rotating cathode, G) electrolyte, H) anode, I) water jacket, J) reference electrode, K) electrolyte pump, L) electrolyte filter, M) electrometer.

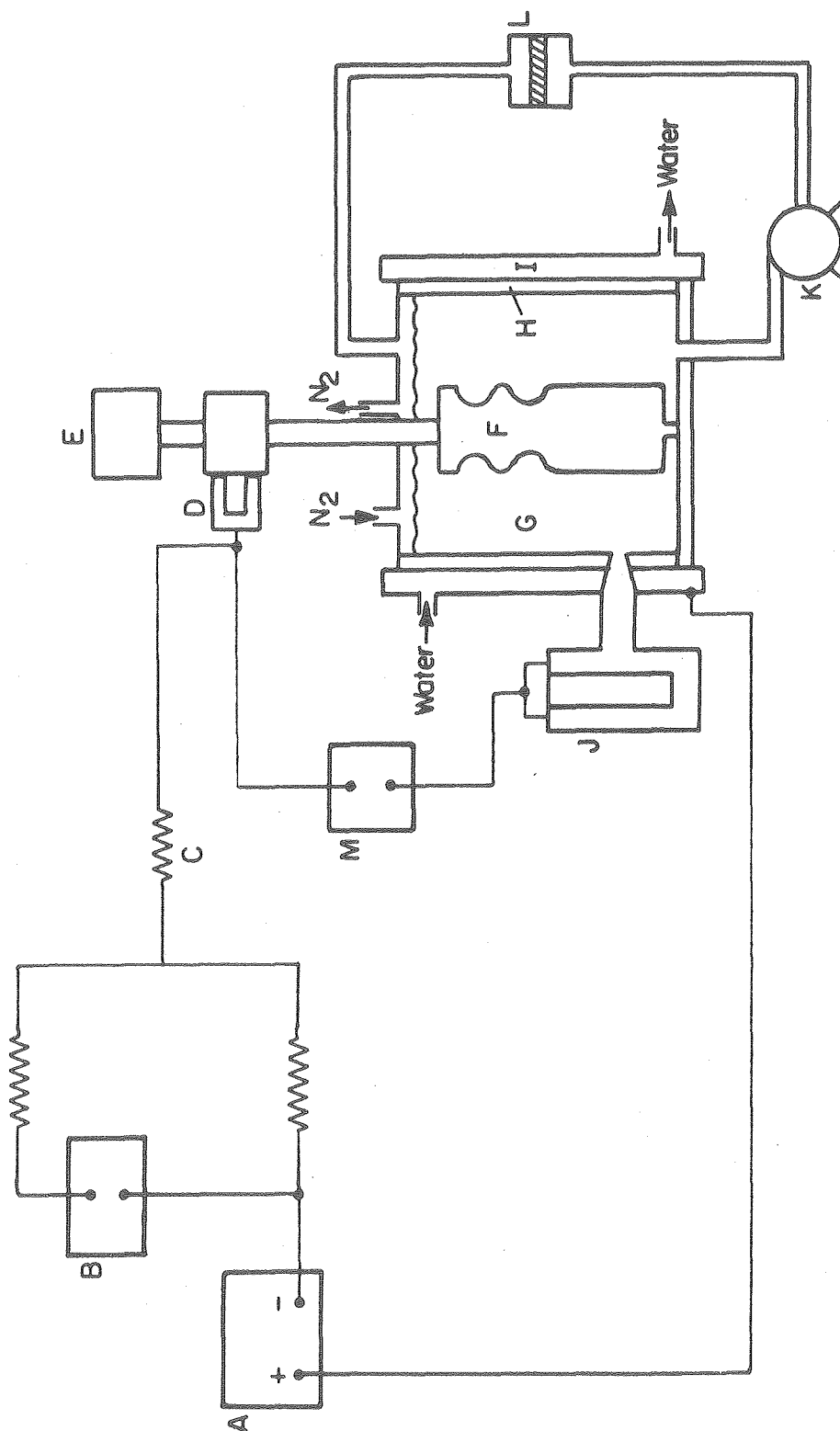


Fig. 12

XBL 805-5241

flush with the anode, was connected to the copper reference electrode. A constant temperature bath maintained the temperature in the reference electrode to within 0.5°C of the electrolyte in the cell. An FMI Corp. model RPD pump continuously circulated the electrolyte through a fritted glass disk, which trapped particles larger than 10 microns. A photograph of the cell appears in Fig. 13.

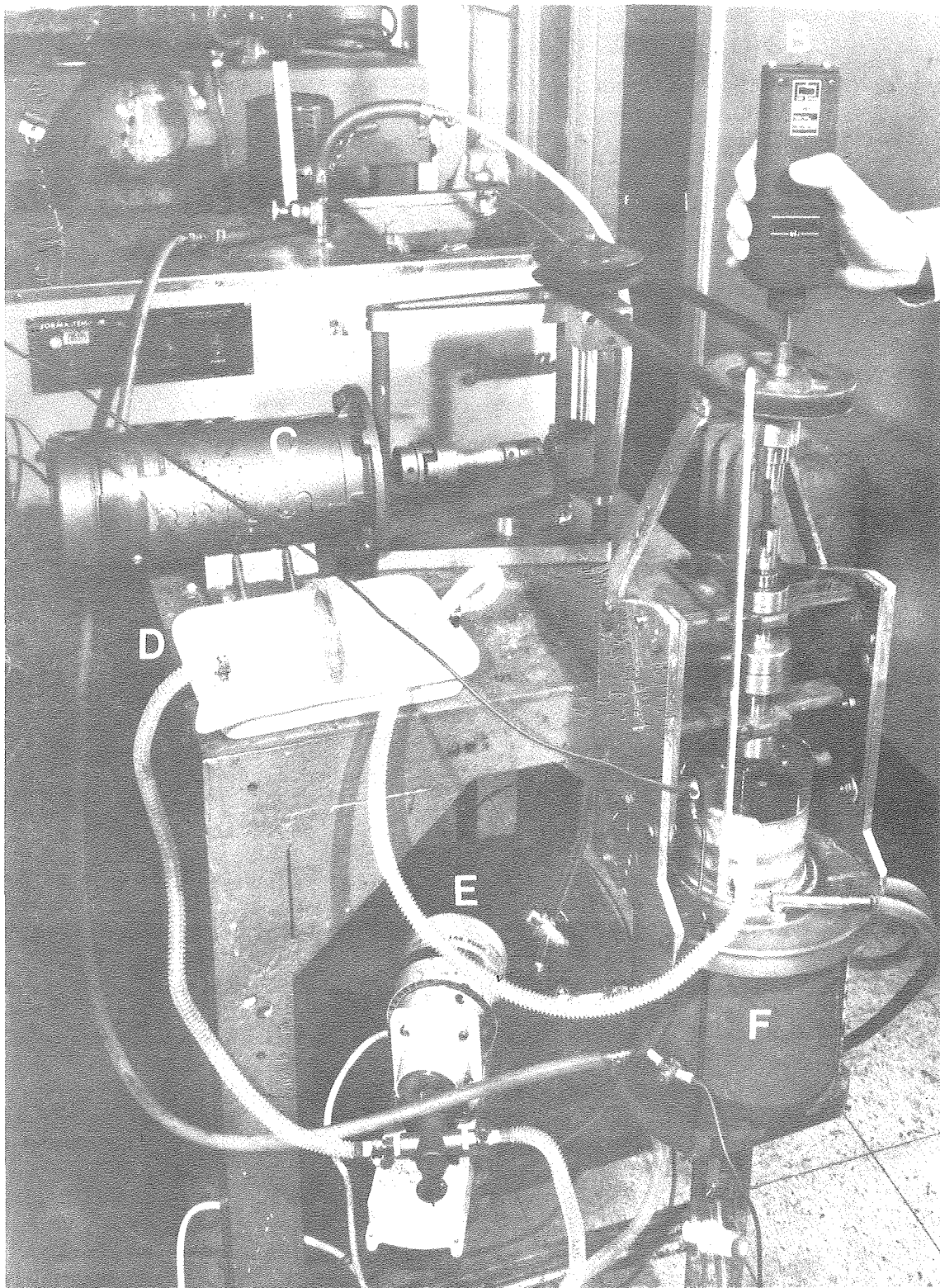
The contoured rotating cylindrical cathodes were machined from type 316 stainless steel. A strike from a cyanide-copper bath was required before each experiment.

Experimental Procedure

The contour of the stainless steel cathode was measured on a Ferranti-Sheffield Co-ordinate Inspection Machine. The cylinder was mounted at its centering marks on the fixed pins of a steel jig. The point where the pin contacted the bottom centering mark was the coordinate system reference point from which the contour was measured before and after deposition. The X and Y coordinates of the axisymmetric surface were determined to within ± 0.006 cm.

Before plating from the acid-copper electrolyte, a cyanide-copper strike was required. The cylinder was weighed and its volume determined by water displacement. The cylinder was rotated at approximately 1000 rpm and buffed to an optical finish with one micron diamond paste. Surface impurities were removed by immersing the cylinder in 10 percent hydrochloric acid followed by an acetone rinse. De-ionized water was used for the final rinse. After pressing the sleeve anode into the cell, it was cleaned with 400 grit emery paper and rinsed with de-ionized water.

Fig. 13. Experimental cell and auxiliary equipment. A) constant temperature bath, B) digital tachometer, C) motor to drive cylinder, D) electrolyte filter, E) electrolyte pump, F) rotating cylinder cell.



XBB 804-4916A

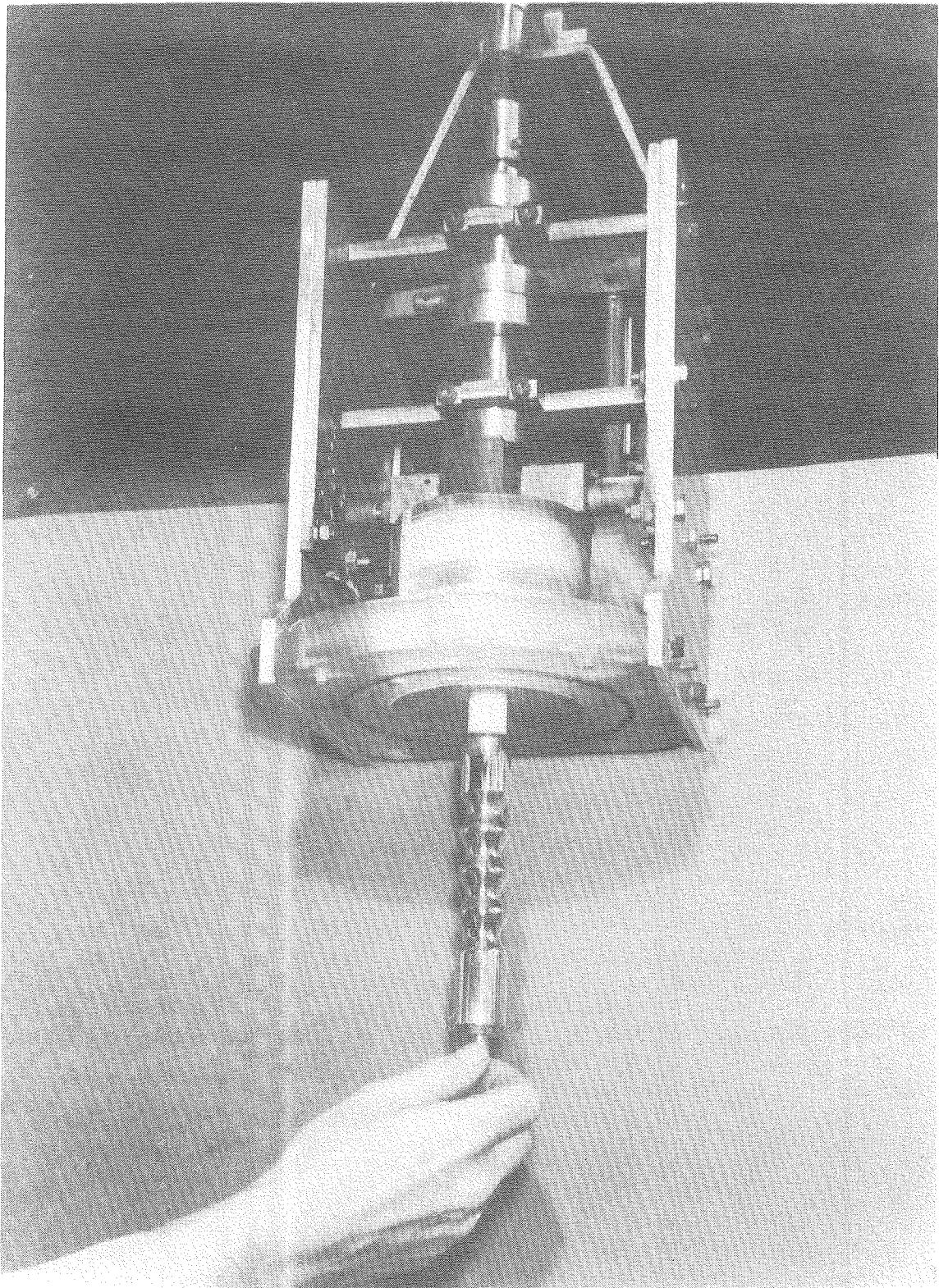
Fig. 13

The cylinder was mounted by a threaded connection to the stainless steel shaft (Fig. 14). The cell was attached to the main assembly and held in place by tightening the nuts on four threaded rods. Four metal bars acted as guides to maintain a reproducible spacing between the top and bottom of the cell. The capillary probe, anode lead, cooling water tubes, and filter system were attached to the cell.

Electrolyte was prepared from reagent grade chemicals and de-ionized water. The dissolved oxygen in the electrolyte was removed by nitrogen sparging. Thirty minutes of sparging with 50 cm³/min was sufficient to remove over 90 percent of the oxygen from 3 L of electrolyte. The electrolyte was added to the cell and reference electrode. The nitrogen blanket above the electrolyte was supplied through a tube from a cylinder.

The filter pump was started and adjusted to circulate the electrolyte at approximately 0.3 L/min. Rotation of the cylinder was begun and the speed checked with a digital tachometer. Electrolyte temperature was regulated to within 0.2°C by adjusting the temperature of the circulating water bath. The applied potential was increased over a one minute period and automatically adjusted through a feedback loop to the power supply. Applied potential, current, and reference potential were continuously monitored on a 3-pen recorder. The charge passed was also monitored by the digital coulometer.

After the run the cylinder was weighed and its volume determined. The final profile was measured in the same way as the original profile. After completing all studies and measurements on the cathode, the



CBB 804-4918

Fig. 14. Installation of contoured rotating cylinder in the cell.

plated copper was dissolved in 50 percent nitric acid. The reproducible stainless steel mandrel was then prepared for a subsequent run.

Polarization Measurements

The same preparation techniques as for the contoured cylinders were used on the smooth copper cylinders for use in taking polarization data. The cylinders were rotated in the electrolyte for one hour at approximately 30 mA/cm^2 so that data could be obtained on a slightly roughened surface ($\sim 0.002 \text{ cm}$). The current was varied between one mA/cm^2 and 100 mA/cm^2 in steps of approximately 10 mA/cm^2 . The applied potential (V_{ap}) and the reference potential (V_r) were recorded at each current step. The reference potential with respect to the rotating cylinder was measured with a Luggin capillary, which was flush with the anode surface.

The cathodic surface overpotential can be determined from the following relation

$$V_{ap} = \eta_s(\text{anode}) + \eta_{cn}(\text{anode}) + \Delta\phi_{ohm} - \eta_{cn}(\text{cathode}) - \eta_s(\text{cathode}) + \Delta\phi_{contact} \quad (28)$$

By convention the cathodic overpotentials are negative. The two anodic contributions were measured directly

$$\eta_s(\text{anode}) + \eta_{cn}(\text{anode}) = V_{ap} - V_r \quad (29)$$

The ohmic drop between the concentric cylinders of height H with inner radius r_i and outer radius r_o is

$$\Delta\phi_{ohm} = I/(2\pi Hk) \ln(r_o/r_i) \quad (30)$$

The concentration overpotential at the cathode is approximately

$$\eta_{cn}(\text{cathode}) = RT/nF \ln(1-i/i_1) \quad (31)$$

The limiting current density i_1 can be calculated from Equation 26. The rotating contact resistance was measured directly before each run. In order to calculate this resistance, a smooth cylinder was partially immersed in a dish of mercury. Current, in the range of interest, was applied to the system, and the potential drop between the connecting lug and the cylinder was monitored with a digital multimeter.

In those days

Copper it was that was the thing of price;

And gold lay useless, blunted with dull edge.

Now lies the copper low, and gold hath come

Unto loftiest honours.

Lucretius

5. EXPERIMENTAL RESULTS AND ANALYSIS

Polarization Parameters

Polarization data were obtained on initially smooth copper cylinders 2.54 cm in diameter. The cathodic transfer coefficient was calculated from the slope of the current density-overpotential plot in the Tafel region. The anodic transfer coefficient was calculated in an analogous manner. Because a relatively large ohmic drop is subtracted when calculating the overpotential, relatively large errors result; however, polarization parameters available in the literature for similar, but not identical, concentrations are of the same order of magnitude. The exchange current density was calculated by extrapolating the polarization curve in the Tafel region to zero overpotential. The polarization parameters obtained in my experiments, as well as those obtained by other investigators, are summarized in Table 9.

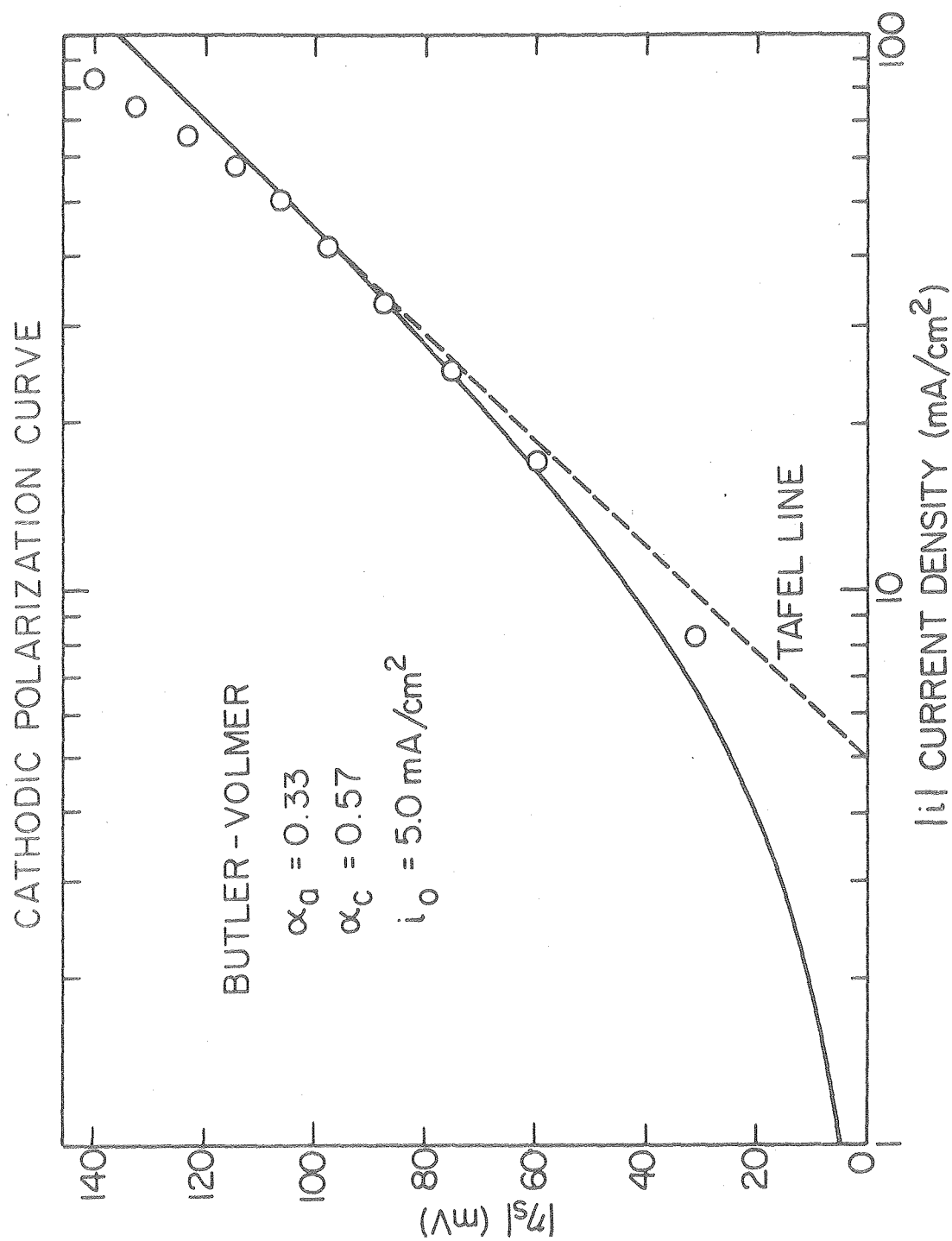
Analysis of Polarization Data

A plot of the experimental overpotential values for use in calculating the polarization parameters is shown in Fig 15. The solid line represents the Butler-Volmer expression with a Tafel slope which is valid in the operating range (20 to 50 mA/cm²) for the contoured cylinder electrodes.

The deviation of the experimental points from the Butler-Volmer equation at high current density probably results from neglecting the concentration dependence of the exchange current density. From an analysis of the data of Mattson and Bockris,²⁰ Newman²¹ calculated a correction to the exchange current density of

Table 9. Polarization parameters.

Temperature (°C)	Concentration		α_c	i_o (A/cm ²)
	CuSO ₄ M	H ₂ SO ₄ M		
25	0.8	1.0	0.57 0.57	0.0045 0.005
40	0.8	1.0	0.65 0.69	0.0097 0.0098
55	0.8	2.0	1.6	0.040
VALUES FROM THE LITERATURE				
25 ²⁰	0.5 0.5 1.0	0.5 1.5 0.5	0.89 0.8 0.94	0.0017 0.001 0.002
25 ²¹	0.5 0.075	0.5 0.5	0.5 0.5	0.008 0.003
25 ²²	1.0	1.0	0.6	0.003



XBL 806-5324

Fig. 15. Cathodic polarization curve.

$$(c/c_b)_{\text{Cu}^{++}}^{0.42}$$

where c and c_b are the cupric ion concentration at the electrode surface and in the bulk electrolyte, respectively. If a linear concentration gradient is assumed

$$(c/c_b)_{\text{Cu}^{++}}^{0.42} = (1-i/i_1)^{0.42} \quad (32)$$

With this correction the upward trend of the data in the high current density region is predicted; if a limiting current density of 0.35 A/cm^2 is used (Eq. 27), about half the difference between the Butler-Volmer equation and the data is accounted for.

The anodic transfer coefficient (α_a) was calculated from data taken on the counterelectrode. Anodic film formation, which has been observed²³ in the acid-copper system, may be responsible for the low α_a (0.33) that was calculated. Mattsson and Bockris²⁰ report a value of 1.5 for α_a in a system with lower CuSO_4 and H_2SO_4 concentrations. The discrepancy between the data and the Butler-Volmer expression at low current density may be explained in terms of the artificially low α_a . Since the current density range below 20 mA/cm^2 is not of great interest, this apparent disparity introduces little error in the model.

Variations in temperature, concentrations of the ionic species and placement of the Luggin capillary are the probable contributors to error in the overpotential. As a basis for comparison, the variations at 50 mA/cm^2 for electrolyte that is 0.8 M CuSO_4 and

1.0 M H_2SO_4 at 25°C were examined for the effect on cathodic overpotential. An increase in temperature decreases the overpotential and increases the electrolyte conductivity. From experimental polarization curves

$$\partial\eta_s/\partial T = -0.001 \text{ V}/^\circ\text{C} \quad (33)$$

The conductivity data of Kern and Chang²⁴ show that

$$\partial\kappa/\partial T = 0.003 \text{ ohm}^{-1} \text{ cm}^{-1}/^\circ\text{C} \quad (34)$$

An increase in copper sulfate concentration reduces the conductivity, while an increase in sulfuric acid increases the conductivity. From Kern and Chang²⁴ these variations can be calculated

$$\partial\kappa/\partial c_{\text{CuSO}_4} = -0.1 \text{ ohm}^{-1} \text{ cm}^{-1}/\text{M} \quad (35)$$

$$\partial\kappa/\partial c_{\text{H}_2\text{SO}_4} = 0.25 \text{ ohm}^{-1} \text{ cm}^{-1}/\text{M} \quad (36)$$

If the Luggin capillary is slightly misplaced, the ohmic drop to the tip will be different from that calculated. The effect on the overpotential is

$$\partial\eta_s/\partial r_o = 0.003 \text{ V/mm} \quad (37)$$

The total error caused by these sources is

$$\begin{aligned} \Delta\eta_s = & -\partial\eta_s/\partial T \Delta T + \partial\eta_s/\partial r_o \Delta r_o + \partial\eta_s/\partial\kappa (\partial\kappa/\partial c_{\text{CuSO}_4} \Delta c_{\text{CuSO}_4} \\ & + \partial\kappa/\partial c_{\text{H}_2\text{SO}_4} \Delta c_{\text{H}_2\text{SO}_4} + \partial\kappa/\partial T \Delta T) \end{aligned} \quad (38)$$

The sense of the temperature change is maintained since the overpotential variation and the conductivity act in opposite directions; only the magnitudes are relevant for the other variations. The variation in overpotential with conductivity is manifested through the change in ohmic drop

$$\partial \eta_s / \partial \kappa = 1.0 \text{ V/ohm}^{-1} \text{ cm}^{-1} \quad (39)$$

The temperature was maintained within 0.2°C. The capillary misplacement was less than 0.5 mm. The electrolyte constituents were within 0.03 M of the specified concentrations. From Eq. (38)

$$\begin{aligned} \Delta \eta_s &= (-0.001)(0.2) + (0.003)(0.5) + (1.0)(0.1)(0.03) \\ &\quad + (0.25)(0.03) + (0.003)(0.2) \\ &= -0.0002 + 0.0015 + 0.003 + 0.0075 + 0.0015 \\ &= 0.014 \text{ V} \end{aligned} \quad (40)$$

The reproducibility of the data is generally of this order. Sources of error such as miscalibrated shunts, multimeter offset, etc. cause errors on the order of a few mV. The error is larger where the ohmic drop is a larger fraction of the cell potential, e.g., at higher current density and at higher temperature.

Contoured Cylinder Experiments

In order to operate over a range of Wagner numbers, the characteristic dimension (the original amplitude) of the sinusoidal cross-section was varied. The other parameters that enter in the Wagner number are more difficult to vary. The electrolyte conductivity and the slope of the polarization curve can each be varied by a factor

of two, whereas the amplitudes of the two profiles studied were varied by a factor of 7. The pertinent conditions of the experimental runs on the contoured cylinders are summarized in Table 10.

Table 10. Experimental parameters.

Experiment Number	Temperature (°C)	Concentration		Rotation Speed	V _{ap}	Time	i _{av} initial	Deposit Weight	W
		CuSO ₄	H ₂ SO ₄						
		(M)	(M)	(RPM)	(V)	(h)	(A/cm ²)	(g)	
20	40	0.8	1.0	800	0.65	25	0.08	290	1.0
22	40	0.8	2.0	800	0.23	48	0.04	293	1.8
28	40	0.8	1.0	800	0.35	18	0.04	103	1.8
32	25	0.8	1.0	800	0.47	15	0.04	112	1.7
33	25	0.8	1.0	800	0.41	25	0.04	158	1.7
34	25	0.8	1.0	800	0.30	46	0.025	167	2.7
35	25	0.8	1.0	800	0.30	20	0.025	92	18.0

6. RESULTS OF SIMULATED EXPERIMENTS

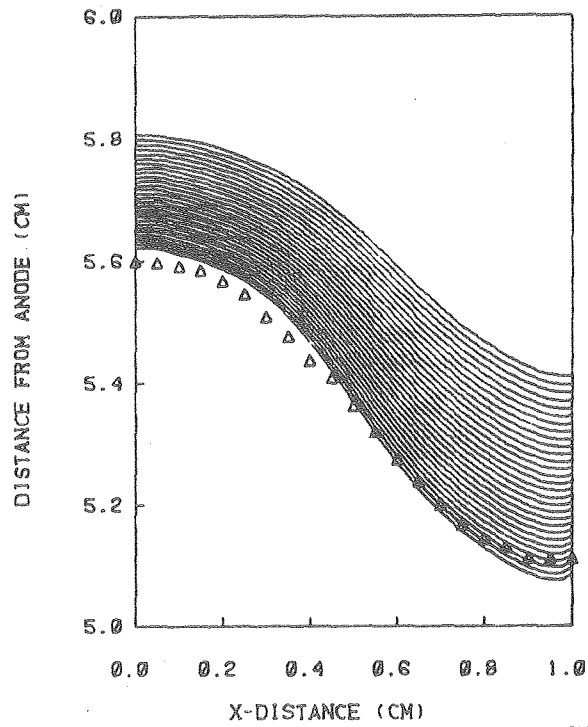
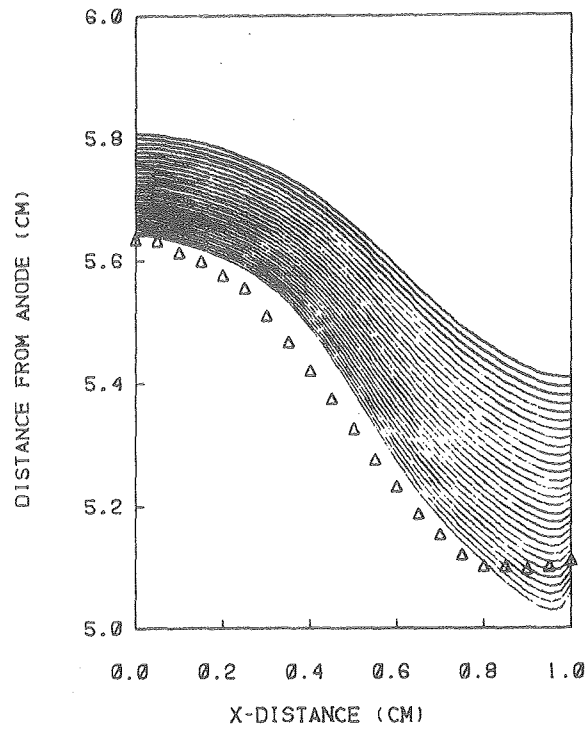
Method

The original coordinates of the contoured cylinders were determined (within ± 0.006 cm) on a Ferranti Inspection Machine, and the coordinates of a half-wavelength of one of the contoured sections were used to define the original profile in the simulation. The values of the electrolyte conductivity, transfer coefficients, and exchange current density were also read-in. An effective applied potential was calculated for use in the simulation by subtracting the resistance in the rotating contacts and the anodic overpotential from the measured applied potential. The total current to the cylinder increased during the experiment for two reasons: (1) the roughening of the surface increased the true surface area and reduced the overpotential, and (2) during deposition the average surface plane moved closer to the counter-electrode and reduced the ohmic losses. The rotating contact resistance is small ($\sim 0.003 \Omega$) and the anodic area is relatively large (5 times the cathodic area); therefore, the increase in total current ($\sim 10\%$) with time at constant applied potential does not significantly affect the effective applied potential, and a constant value was assumed.

From the deposit weight on the contoured cylinders, the charge passed was calculated so that the simulation could be halted after the appropriate number of time steps. Comparisons of final simulated profiles and selected experimental profiles are shown in Figs. 16 to 19. The maximum deviations based on the deposit thickness at selected points are listed in Table 11.

Fig. 16. Half-wavelength of the simulated and experimental profiles. The upper curve depicts the original profile, and the lowest curve is the simulated final profile. The experimentally obtained profile is denoted by triangles. Run number 20.

Fig. 17. Simulated vs. experimental results for run number 22. Other details as in Fig. 16.



XBL 808-10858A

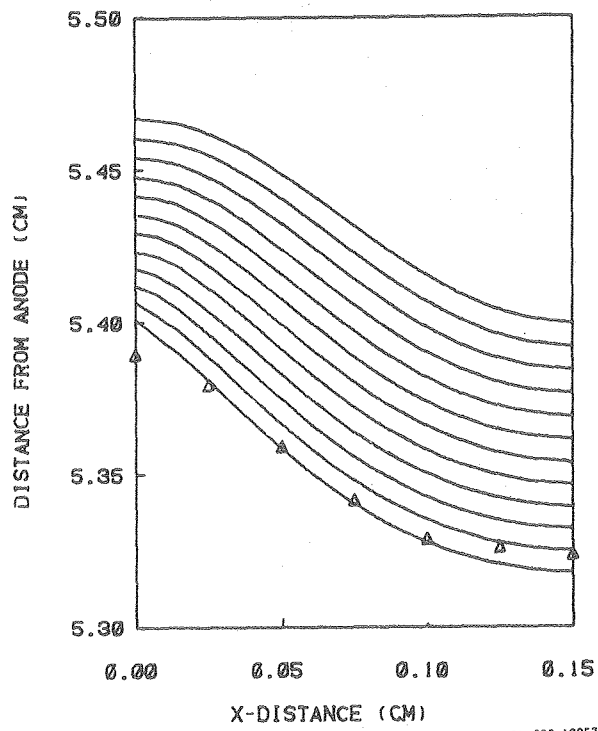
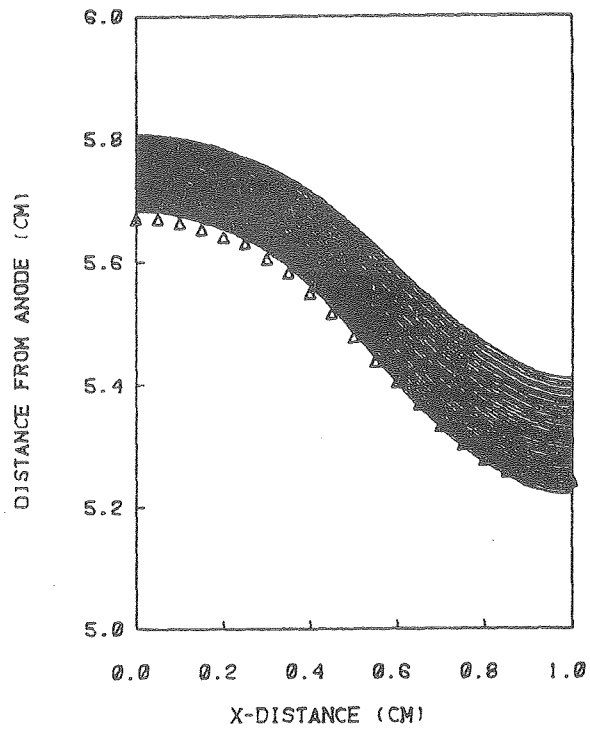
Figs. 16-17

Fig. 18. Simulated vs. experimental results for run number 34.

Other details as in Fig. 16.

Fig. 19. Simulated vs. experimental results for run number 35.

Other details as in Fig. 16.



XBL 808-10857A

Figs. 18-19

Table 11. Experimental vs. simulated profile coordinates.

Experiment Number	Y(0) Measured cm from anode	Y($\lambda/4$) Measured cm from anode	Y($\lambda/2$) Measured cm from anode	Y(0) Simulated cm from anode	Y($\lambda/4$) Simulated cm from anode	Y($\lambda/2$) Simulated cm from anode	Maximum Percent Difference
20	5.63	5.32	5.11	5.64	5.38	5.60	18
22	5.60	5.36	5.11	5.62	5.37	5.08	10
28	5.73	5.54	5.28	5.73	5.55	5.28	9
32	5.72	5.55	5.30	5.73	5.55	5.28	15
33	5.69	5.47	5.25	5.70	5.50	5.22	18
34	5.67	5.48	5.23	5.68	5.48	5.22	8
35	5.39	5.34	5.32	5.40	5.35	5.32	12
Original Coordinates	5.80	5.65	5.41	$A_0 = 0.2, \lambda = 2 \text{ cm}$			
	5.47	5.44	5.41	$A_0 = 0.03, \lambda = 0.3 \text{ cm}$			

Analysis of Contoured Cylinder Results

The discrepancy between the experimental and simulated results on the rotating contoured cylinders averages approximately 10 percent. In general, the shape of the final profile is qualitatively more similar to the simulated result for thinner, smoother deposits. The disparity between simulation and experiment is most apparent in run number 20 (Fig. 16), where the average deposit thickness was approximately 2 mm and the average roughness was on the order of 0.1 mm. The experimental result is that which would be expected if the overpotential near the peak were increased. A probable explanation of this phenomenon is that plasticizer from the PVC based filter tubing, which was used in runs 20 and 22, acted as a leveling agent. In the 48 hour run (run 22) a white viscous material was clearly evident in the filter. Flexible teflon tubing, which is inert in the acid system, was used in all subsequent experiments. In an experiment under the same conditions, but with the teflon tubing, a much rougher deposit was obtained. Because the roughness was of the same order of magnitude as the deposit thickness, meaningful measurements could not be obtained. The roughness obtained in the absence of the PVC tubing tends to support the hypothesis that a leveling effect was caused by the PVC tubing.

Run number 22 (Fig. 17) was conducted under conditions similar to run number 20, except that the initial average current density was approximately half that of run number 20. Since the Wagner number was approximately double that of run number 20, a more uniform current distribution was obtained. The kinetic effects tended to mask the leveling effects, and better agreement resulted. In run number 34

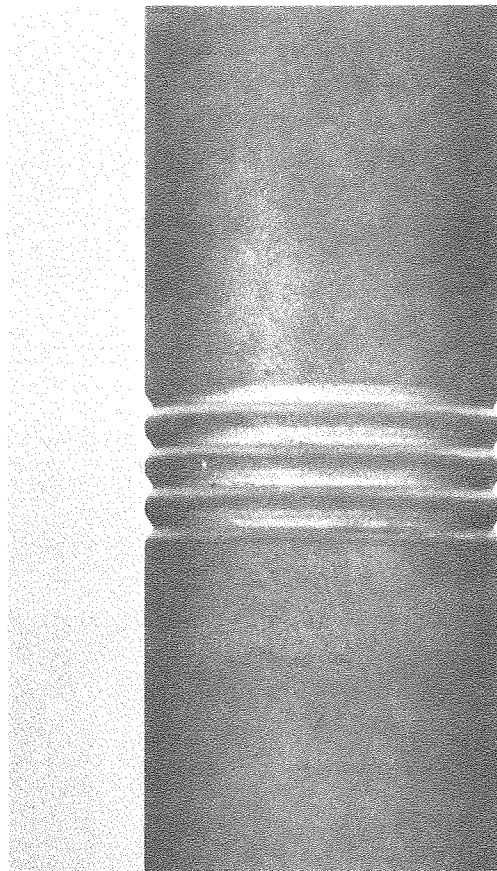
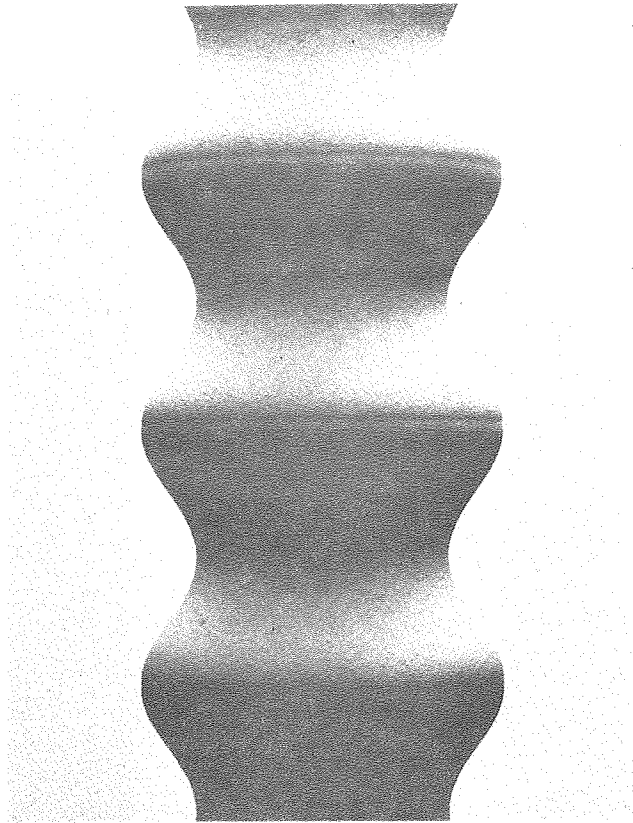
(Fig. 18) the average current density was again halved. A coherent matte deposit, approximately 1.5 mm thick, was obtained, and the agreement with the simulated curve was within 10 percent at each point. Since the model does not account for local variations in roughness, a uniform, relatively smooth deposit favors a current distribution that can be successfully simulated.

In run number 35 (Fig. 19) the contoured cylinder with the smaller amplitude (0.03 cm) and wavelength (0.3 cm) was used. The characteristic dimension was reduced by an order of magnitude, and the Wagner number was correspondingly increased by an order of magnitude. The small depression that forms on the peak for a low Wagner number run (Fig. 20) is absent in the high Wagner number case (Fig. 21). The formation of a characteristic feature, such as the depression at the peak, is addressed in the next section.

In summary, the deviations between experiment and simulation are generally on the order of 10 percent. Discrepancies of this magnitude can be attributed to standard experimental error: initial and final profile measurement, as well as conductivity, current, and temperature variations. Observable variations in surface roughness also contribute to current density variations.

Fig. 20. Contoured rotating cylinder electrode. $A_o = 2\text{ mm}$, $\lambda = 2\text{ cm}$,
 $W = 2.7$.

Fig. 21. Contoured rotating cylinder electrode. $A_o = 0.3\text{ mm}$, $\lambda = 3\text{ mm}$,
 $W = 18$.



BBC 807-8914A
Figs. 20-21

7. EFFECTS OF OHMIC DROP AND CURVATURE

The relative effects of ohmic drop and curvature cause variations in the primary current distribution on an electrode profile. In this section I am using the term ohmic drop to describe the effect of distance from the counterelectrode on the current distribution. The ohmic drop in these terms is the resistance when no curvature is present, viz. between two infinite plane parallel electrodes. The current-voltage relationship in this case is linear and can be modeled as a linear resistor. Where the electrode separation is smaller, the ohmic drop is smaller, and more current flows.

An electrode that is convex with respect to the counterelectrode tends to attract more current to the curved region. With a primary current distribution the equipotential lines nearest the electrode surface tend to follow the surface contour; since the flux lines must be perpendicular to the equipotentials, the current density tends to rise where the curvature is high. In the extreme case of an electrode with a sharp corner, the curvature and the current density are infinite at that corner.

In order to study the interaction between curvature and ohmic drop, four model electrode cross-sections were considered: circular, parabolic, sinusoidal, and biquadratic. In each case the electrode was oriented with its plane of symmetry perpendicular to a plane counterelectrode (Fig. 1).

With this arrangement the peak, which is on the line of symmetry, is nearest to the counterelectrode, and, therefore, favored ohmically. The curvature is a maximum at the peak for the parabolic

and sinusoidal electrodes and a minimum at the peak for the biquadratic electrode. The curvature is uniform on the circular electrode. The peaks of the parabolic and the sinusoidal electrodes are favored by maximum curvature and minimum ohmic resistance; therefore, one expects that the primary current distribution on the initial profile will be maximum at the peak. For the biquadratic electrode the peak is favored ohmically, but the maximum curvature occurs away from the peak. Because of these competing effects, one cannot easily predict the position of the current density maximum. In the case of the circular electrode, the current density should be maximum at the peak since the curvature is everywhere uniform, but the peak is ohmically favored. The numerical simulations show that the maximum current density on the initial profile is at the peak when the curvature is also maximum there. In the biquadratic case the current density is maximum near the curvature maximum but is slightly shifted toward the peak the ohmic drop is lower.

As the profile advances, the curvature and relative ohmic drop change in ways that are not easily predicted from a knowledge of the initial current distribution. Intuitively, one expects the peak to grow preferentially if it is initially relatively sharp; conversely, a profile that is relatively blunt might be expected to form "shoulders" that would then grow preferentially in an area away from the peak.

The growing profiles with a primary current distribution were simulated in six different cases: a high and a low amplitude-to-wavelength (A_0/λ) ratio sinusoidal profile, a high and a low focal length parabolic profile, a circular electrode, and a biquadratic electrode.

The advancing low amplitude ($A_0/\lambda = 0.025$) sinusoidal profile is shown in Fig. 10. In this case the peak is favored at each time step and eventually becomes sharper. For $A_0/\lambda = 0.1$, the profile tends to grow rapidly in a region away from the peak, and consequently, a depression forms at the peak (Fig. 11).

The fundamental differences between the characteristics of the two profiles can be seen on normalized plots of the key variables: curvature, distance from the counterelectrode, and initial current distribution. I have chosen to normalize each variable over its range; thus, for distance from the counterelectrode

$$Y_{\text{norm}} = (Y_{\text{min}} - Y)/(Y_{\text{min}} - Y_{\text{max}}) \quad (41)$$

Each variable was normalized in a similar manner so that it is zero where X is one and is one where X is zero.

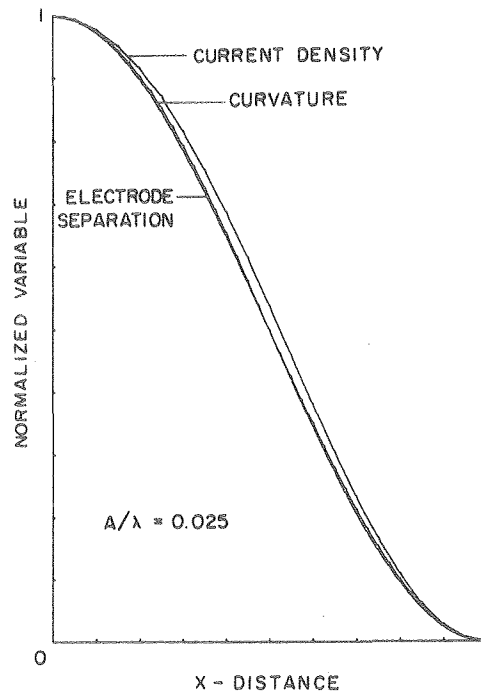
For the low amplitude sine wave, Fig. 22 shows that the curvature and the current density are varying approximately linearly with the sinusoidal profile. The value of the normalized curvature is less near the peak in the low amplitude case; therefore, the curvature does not strongly influence the current distribution, and the resulting distribution is similar to that which would be obtained from placing plane electrodes at corresponding positions. Since ohmic effects dominate, the peak is favored and continues to be favored during growth.

For the high amplitude sine wave the curvature at the peak falls more rapidly, and the current density also drops more rapidly (Fig. 23). The current density is decreasing most rapidly near $X = 0.8$. Since the curvature is also relatively high near $X = 0.8$, a shoulder begins

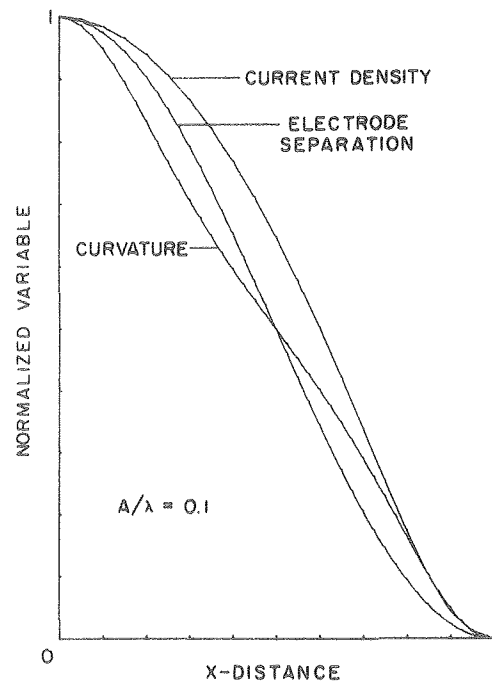
Fig. 22. Normalized values of current density, electrode separation, and curvature for a low A_0/λ sinusoidal profile. Note that current density and curvature are maximum at $X = 1$.

Fig. 23. Normalized values of selected variables for a high A_0/λ sinusoidal profile.

SINUSOIDAL PROFILE



SINUSOIDAL PROFILE



XBL 808-5657A

Figs. 22-23

to form in that area. As the profile advances, the curvature increases in the shoulder area, and relatively more current is attracted to that area than to the peak. Eventually, the current density becomes higher in the shoulder region, and diversion of current from the peak causes a depression to form at the peak.

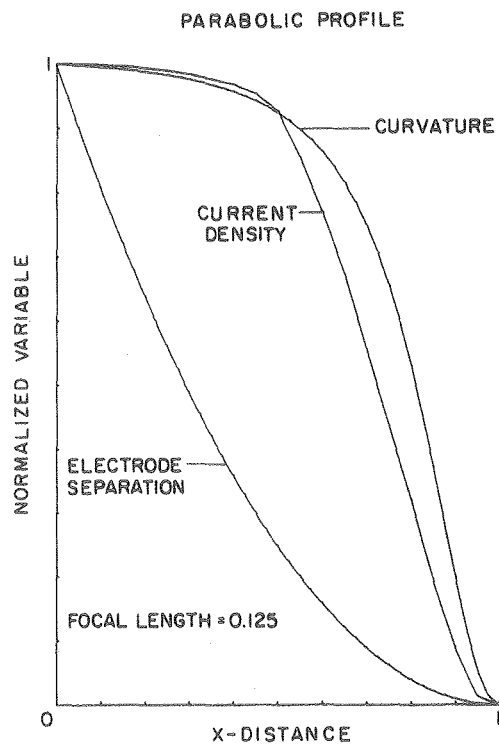
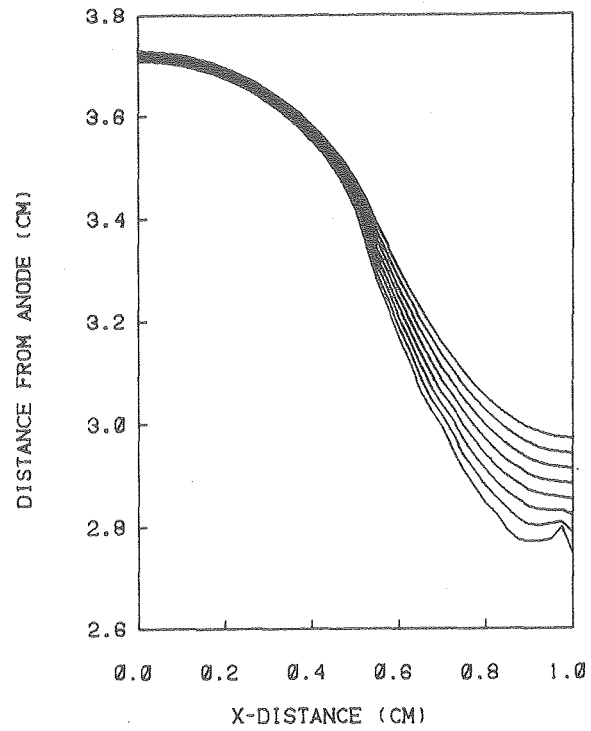
For the parabola and other non-periodic functions, a circular section was joined to the original curve in order to obtain a finite non-zero current density near $X = 0$. In this region the current density is sufficiently small so that changes in this area do not appreciably disturb the current density near the peak. The parabola with the smaller focal length grows in the manner that is intuitively expected. The initially high curvature on the peak and the ohmically favored position of the peak cause the current density to be a maximum there as the profile advances (Fig. 24). The rapid decrease in curvature and current density near the peak are shown in Fig. 25. As the focal length is increased, the parabola becomes blunted, and a more uniform initial current distribution near the peak results (Fig. 26). Eventually, a shoulder forms near $X = 0.9$, and that area advances more rapidly than the peak (Fig. 27).

The circular electrode also develops a shoulder away from the peak (Fig. 28). The plot of the normalized current density (Fig. 29) shows that the current density decreases moderately with respect to electrode spacing near the peak. The negative curvature in the recess ($X = 0$ to 0.5) causes the current density to be relatively low there.

Fig. 24. Simulated deposition on a low focal-length parabolic electrode.

$W = 0$.

Fig. 25. Normalized values of selected variables for a low focal-length parabolic profile.

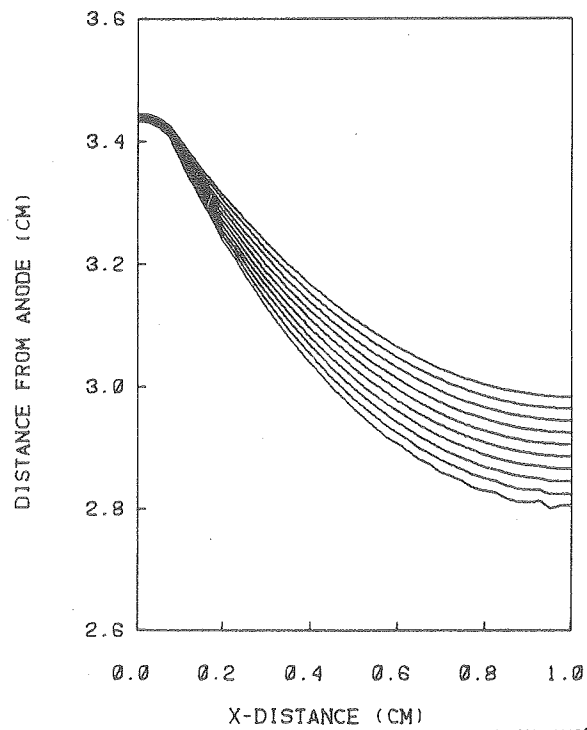
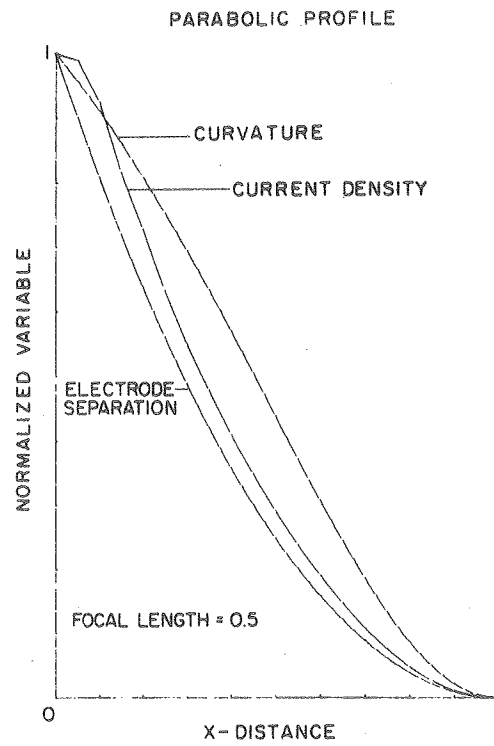


Figs. 24-25

Fig. 26. Normalized values of selected variables for a high focal-length parabolic profile.

Fig. 27. Simulated deposition on a high focal length profile.

$W = 0.$

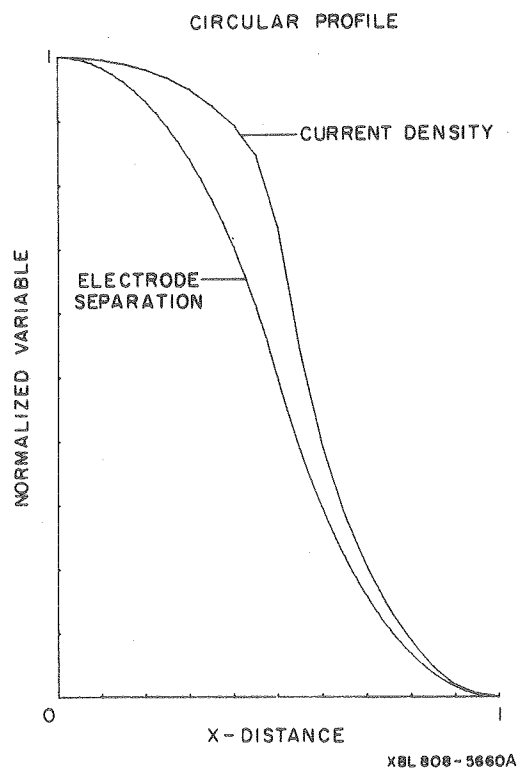
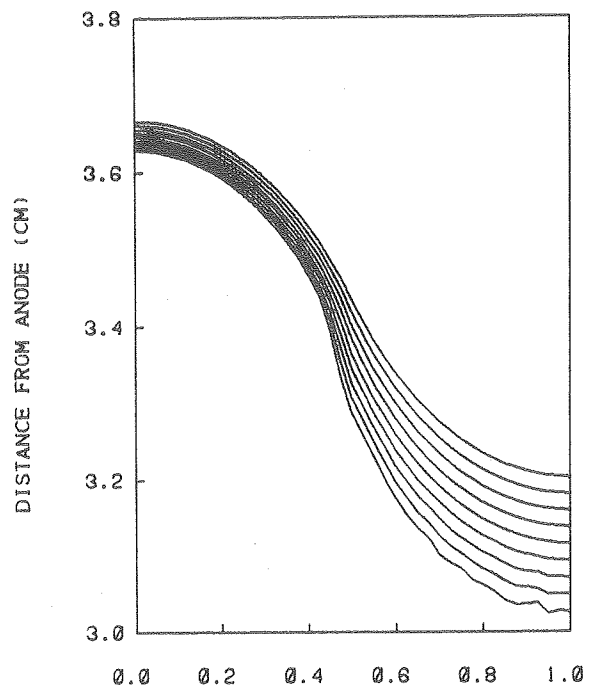


XBL 808-11327A

Figs. 26-27

Fig. 28. Simulated deposition on a circular profile. $W = 0$.

Fig. 29. Normalized values of selected variables for a circular electrode.



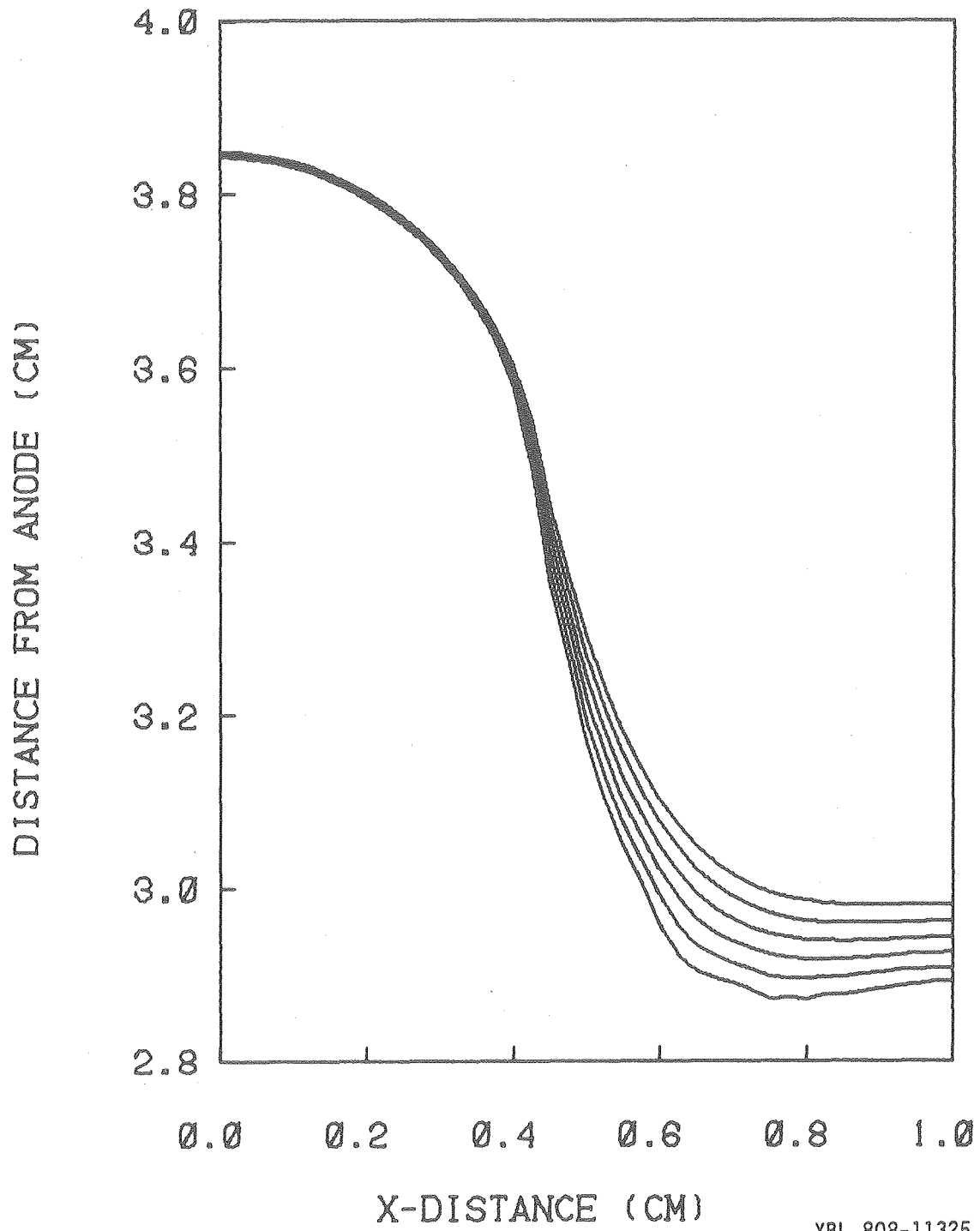
Figs. 28-29

The biquadratic electrode (Fig. 30) continues to grow most rapidly where the initial current density is highest, near $X = 0.75$. In time this area grows more rapidly than the peak.

Generalizations that can be made from this study are only valid for a primary current distribution where the cathode is described by a continuous, monotonic, even function with a single curvature maximum, and the counterelectrode is a plane surface perpendicular to the axis of symmetry. When the curvature is a maximum at the peak, there are two extreme cases where the peak tends to accelerate as it advances. When the peak is initially sharp, it attracts substantially more current than the immediate surroundings, and it grows preferentially. At the other extreme where the curvature on the entire profile is small and the current density decreases linearly with distance from the counterelectrode, the ohmic effects dominate. A shoulder, associated with a relatively rapid decrease in current density away from the peak, does not form, and the peak grows most rapidly.

In the cases that fall between these extremes, a shoulder forms in an area away from the peak. The curved region then attracts more current and grows more rapidly than the peak. The shoulder forms sufficiently near the peak so that current is diverted from the peak, and a depression forms there. When the peak is not coincident with the curvature maximum, as in the biquadratic case, a depression forms near the curvature maximum rather than at the peak.

Some approximate quantitative relations can be generated from these examples. One criterion for formation of a sharp peak is that the current density decrease linearly with distance from the counter-



XBL 808-11325

Fig. 30. Simulated deposition on a biquadratic electrode.

electrode. In the normalized plot for the low-amplitude sine wave (Fig. 22), the normalized current density near the peak (X greater than 0.7) is always within 3 percent of the normalized distance from the counterelectrode. The difference between the normalized distance is 6 percent at $X = 0.7$ for the circular electrode (Fig. 29). The peak does not become sharp for the circle; hence, the 3 percent deviation is approximately the maximum difference that can be tolerated in order to form a sharp peak.

For the profile that is initially relatively sharp, the current density decreases rapidly near the peak. One measure of the rate of decrease is $|di/dX|_{\text{norm}}$ where the normalized current density is 90 percent of its value on the peak. A value of one for $|di/dx|_{\text{norm}} / |dY/dX|_{\text{norm}}$ at that point indicates a linear variation of current density with counterelectrode distance. A larger value indicates that the current density is falling more rapidly because of curvature effects. For the low focal length parabola the normalized current density is 90 percent of the value at the peak near $X = 0.9$ (Fig. 25). At this position the ratio of derivatives is 9. For the high focal length parabola the normalized current density falls to 90 percent of its maximum value near $X = 0.7$, where the ratio of derivatives is 1.2. This analysis suggests that if the ratio of derivatives is on the order of at least 10, the peak will sharpen.

For the biquadratic curve described by $Y = B(X-1)^4$, where $B = 5$, the effect of curvature causes the initial current density maximum to shift away from the peak to $X = 0.75$. This point continues to be favored and continues to advance most rapidly as the profile grows.

As the coefficient B is increased, the curvature maximum becomes larger and shifts toward the peak. It seems reasonable that the peak would be favored for extreme values of B . For a sufficiently large value of B , the curvature maximum will occur at a point indistinguishable from the peak; for a small value of B , the curvature effects will be negligible and ohmic effects will dominate. For example, the maximum curvature occurs near $X = 0.99$ for B equal to 1000. The curvature is 120 there but falls rapidly to 5 at $X = 0.98$. At the other extreme the curvature is a maximum at $X = -8$ for B equal to 2×10^{-4} . At this point the curvature is only 0.13, but the electrode is 1.3 units farther from the counterelectrode than the peak.

As the Wagner number is increased, the current distribution becomes more uniform, and the effects of curvature and ohmic drop become less pronounced. The formation of a shoulder, for example, on a sinusoidal profile is a manifestation of competing ohmic and curvature effects. If these effects are suppressed, then the shoulder is less likely to form. A comparison of Fig. 23 and Fig. 30 shows the difference between an advancing profile resulting from a primary and a secondary current distribution. For a profile with $A_0/\lambda = 0.1$, formation of a shoulder and accompanying depression at the peak for an equal amount of charge passed does not occur when $W = 1$ (Fig. 31).

Only the magnitude of the amplitude and wavelength of the profiles ($A_0/\lambda = 0.1$ in both cases) was significantly varied between experiments 34 and 35. Since the Wagner number is inversely proportional to the characteristic dimension, W is higher by an order of magnitude for the smaller profile. Although the average surface plane advanced

CATHODIC DEPOSITION

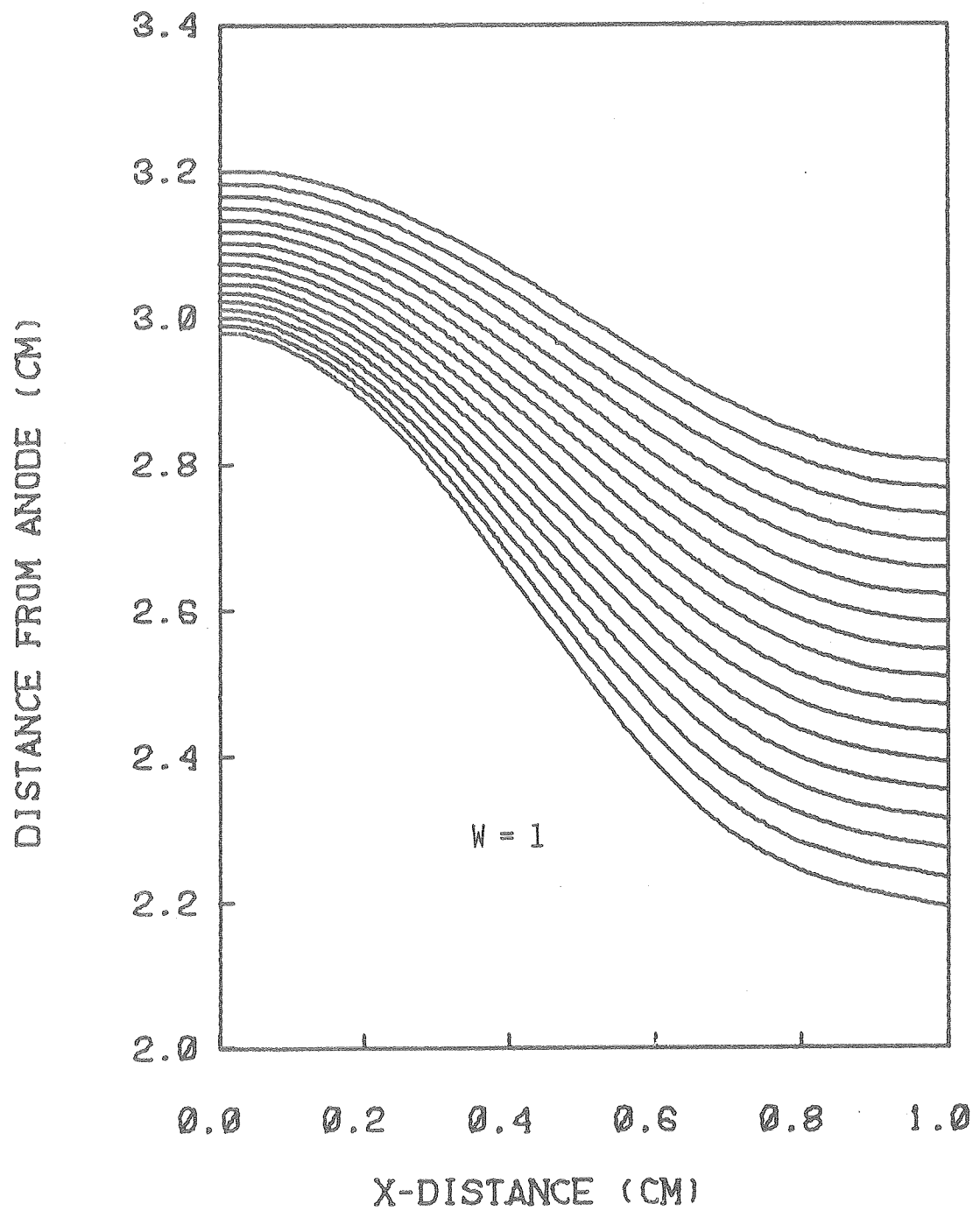


Fig. 31. Simulated deposition on a sinusoidal profile. $A_0/\lambda = 0.1$,
W = 1.3.

XBL 801-7634

by a greater number of original amplitudes, no depression at the peak occurred for the smaller profile. The smaller characteristic length permits a more uniform current distribution and, therefore, a more uniform growth of the profile.

8. SIMULATIONS OF SELECTED GEOMETRIES

Corner Problem

The rounded corner electrode has several interesting features. The current density in the corner tends to rise. In addition, the current density may vary significantly over the profile, and the effect of kinetic limitations has a striking effect on the metal distribution. In plating practice the higher current density may cause an excessive deposit in the corner area, and above a certain current density level the deposit may burn, i.e., form a rough, discolored deposit. In the present study the effects of varying the Wagner number and the geometric parameters are examined. In a subsequent section other methods of altering the current distribution will be investigated.

In the first series of simulations, the counterelectrode is closer to the cathode than is the insulating wall. The result of depositing with a primary current distribution is illustrated in Fig. 32. The simulation was halted after the peak became sharp, and a relatively high current density developed there.

The greatest amount of charge is passed somewhat above the midpoint of the corner. As the peak progresses, its growth is accelerated because of increased curvature at the top surface and because of the proximity of the peak to the counterelectrode. The peak attracts current from the immediate surroundings and causes depressions to form on either side. The metal distribution near $X = 0$ is unaffected by the corner and approaches the uniform thickness that would be obtained from depositing between two plane electrodes. The resistance increases considerably in the recess, and little deposition occurs there.

The effects of increasing the Wagner number are illustrated in Figs. 33, 34 and 35. In each simulation the same amount of charge has been passed to arrive at the final profile. At a Wagner number of 0.01, the final profile is similar to the result from the primary current distribution. At $W = 0.1$, the peak is flatter, and the depressions on either side of the peak have disappeared. At $W = 1$, the metal distribution is much more uniform, and the peak is no longer discernable.

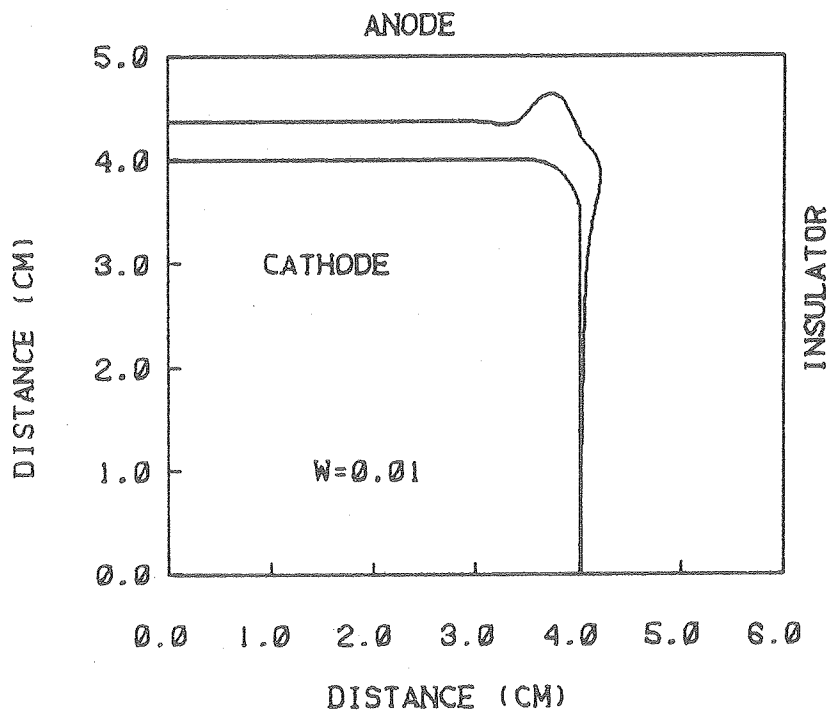
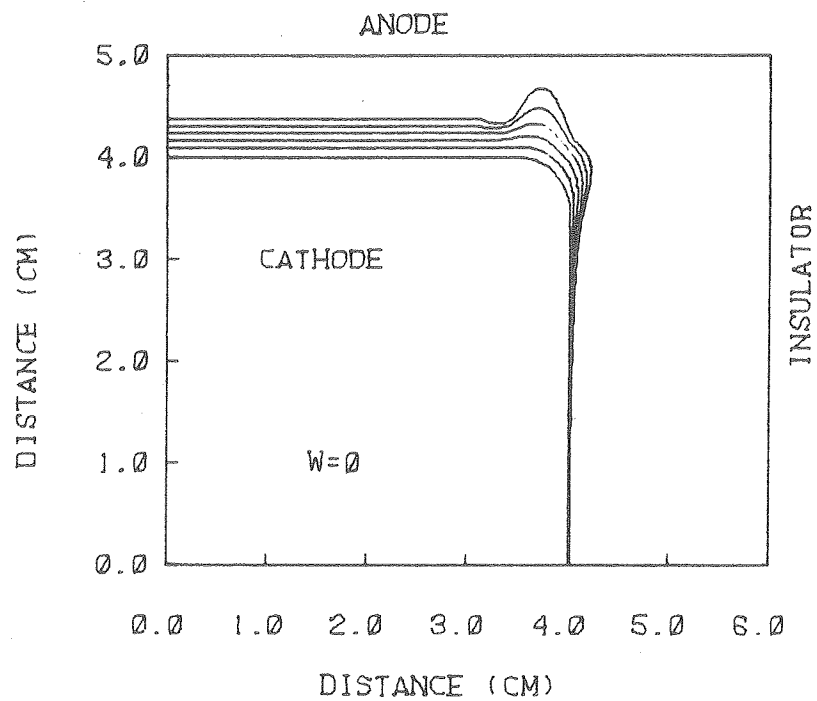
One method of quantifying the changes in metal distribution is to measure the height of the peak above a characteristic deposit thickness. I have chosen to take the maximum deposit weight above the original horizontal cathode plane ($Y = 4$) and divide this distance by the deposit thickness at $X = 0$. With this definition a larger ratio is characteristic of a non-uniform current distribution. The results are tabulated in Table 12. For the primary current distribution the ratio is 1.8. For a Wagner number of one, the peak is imperceptible.

In the second series of simulations, the insulator was moved closer to the cathode, and the counterelectrode was moved farther away. The same series of simulations was run for this geometry as for the previous one. The primary current distribution simulation displays the same characteristic features as those in the previous geometry (Fig. 36). In contrast to the previous series, for a Wagner number of 0.1, the depression on the right hand side of the peak has disappeared (see summary Fig. 37). This difference arises because the anode is farther away, and the relative ohmic advantage of the peak is less. As a result, the peak is somewhat blunter, and less

Fig. 32. Simulated deposition on a corner electrode. The anode is at the top surface, the cathode occupies the lower left-hand corner, and all other surfaces are insulated.

$W = 0$.

Fig. 33. Deposition on a corner electrode. The intermediate time steps have been removed. $W = 0.01$. Other details as in Fig. 32.

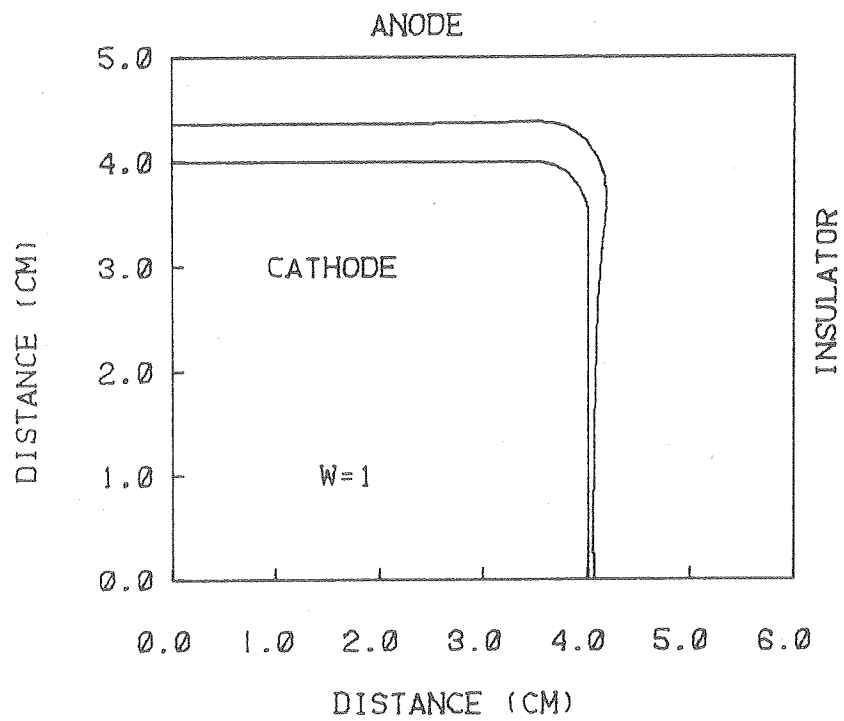
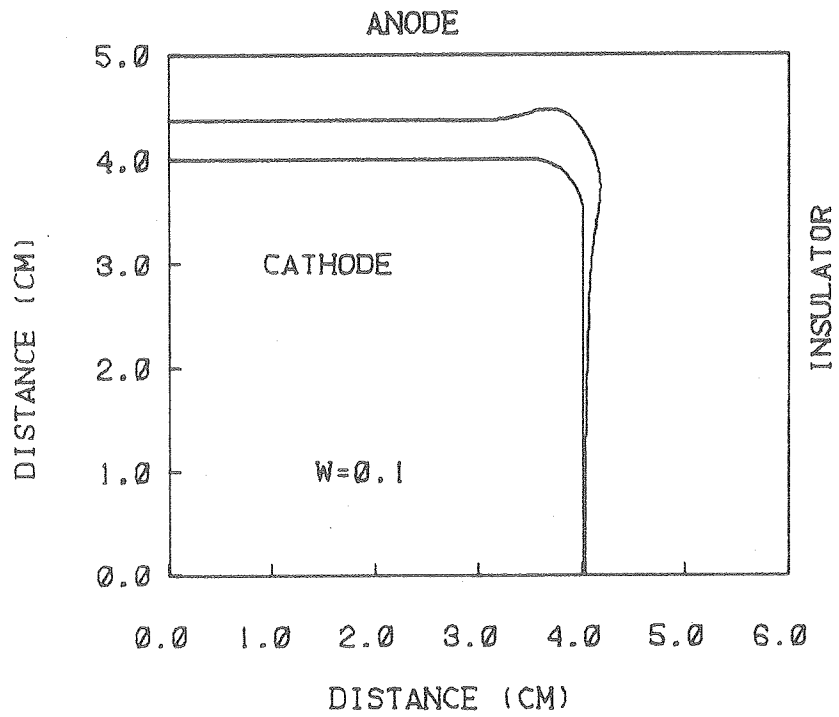


XBL 7910-12064A

Figs. 32-33

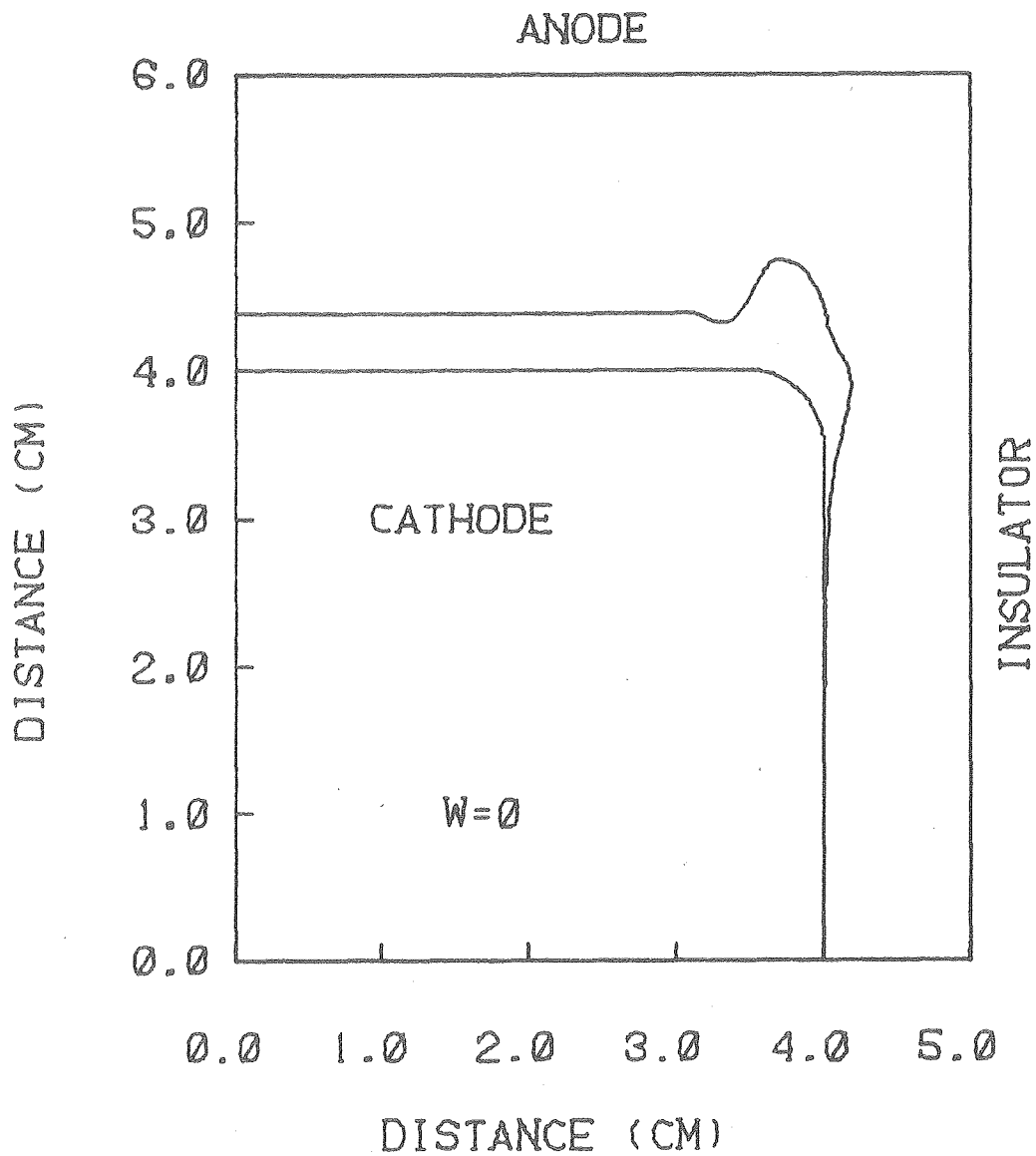
Fig. 34. Deposition on a corner electrode. $W = 0.1$. Other details as in Fig. 32.

Fig. 35. Deposition on a corner electrode. $W = 1$. Other details as in Fig. 32.



XBL 7910-12066A

Figs. 34-35



XBL 799-12059

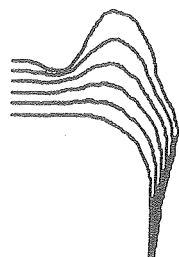
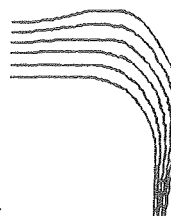
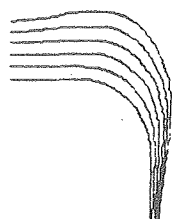
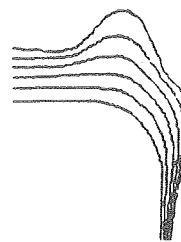
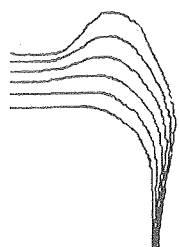
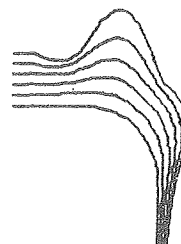
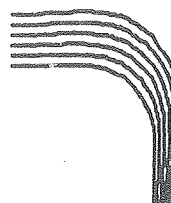
Fig. 36. Deposition on a corner electrode. Note that anode is farther from the cathode, and the insulator is closer than in Fig. 32.
 $W = 0$.

Fig. 37. Summary of the simulated deposition on the corner electrodes.

The series on the right is from the cells shown in Figs. 32 to 35. The series on the left is from the cell shown in Fig. 36. Proceeding downward, the Wagner numbers are approximately 0, 0.01, 0.1, and 1.

INSULATOR CLOSE

ANODE CLOSE

 $W=0$  $W=1$ 

XBL 7910-12072

Fig. 37

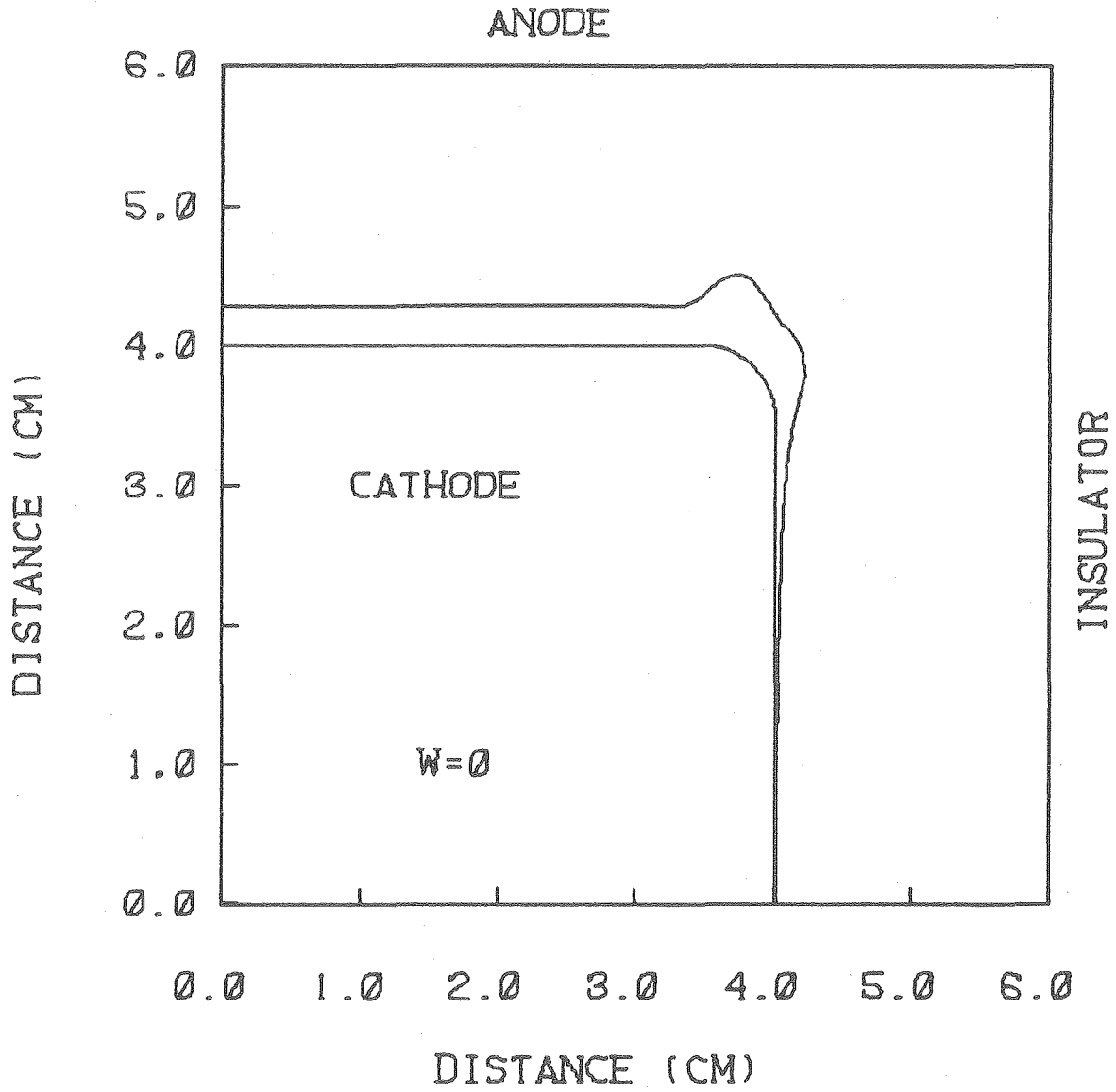
Table 12. Ratio of maximum deposit thickness
to characteristic deposit thickness.

Wagner Number	Y_{\max}/Y_{char}	
	Anode Close	Insulator Close
0	1.8	2.0
0.02	1.7	1.8
0.1	1.3	1.3
1.0	1.1	1.0

current is diverted from the immediate surroundings. At a Wagner number of one, the kinetic resistance becomes significant, and the differences due to the geometric variations become less important.

In order to control the metal distribution, auxiliary electrodes and shields can be placed at strategic points in the electrolyte. These devices are commonly used in metal plating operations. The auxiliary electrode, at the same potential as the cathode, redirects the current more effectively, but the current efficiency suffers since some of the metal is plated on the auxiliary electrode, rather than on the cathode. The shield is an insulating material. Although it increases the cell resistance, it does not generally affect the current efficiency. These devices can be simulated, and their effects on the metal distribution can be determined.

The simulated metal deposit resulting from a primary current distribution, where the insulator and the anode were initially equidistant from the cathode is shown in Fig. 38. For certain applications a relatively uniform deposit in the corner area would be desirable. In Fig. 39 the result of placing a shield near the anode is shown. Some of the current is diverted from the peak, and a slightly blunter peak results. As the insulator is moved closer to the cathode, the redirected current reinforces and sharpens the peak (Fig. 40). Clearly, placing the shield at the location shown would be undesirable. An auxiliary electrode placed at the same location as the shield in Fig. 39 produces a relatively uniform deposit around the corner (Fig. 41). If the auxiliary electrode is moved closer to the cathode, the deposit becomes thinned at the corner (Fig. 42). From these

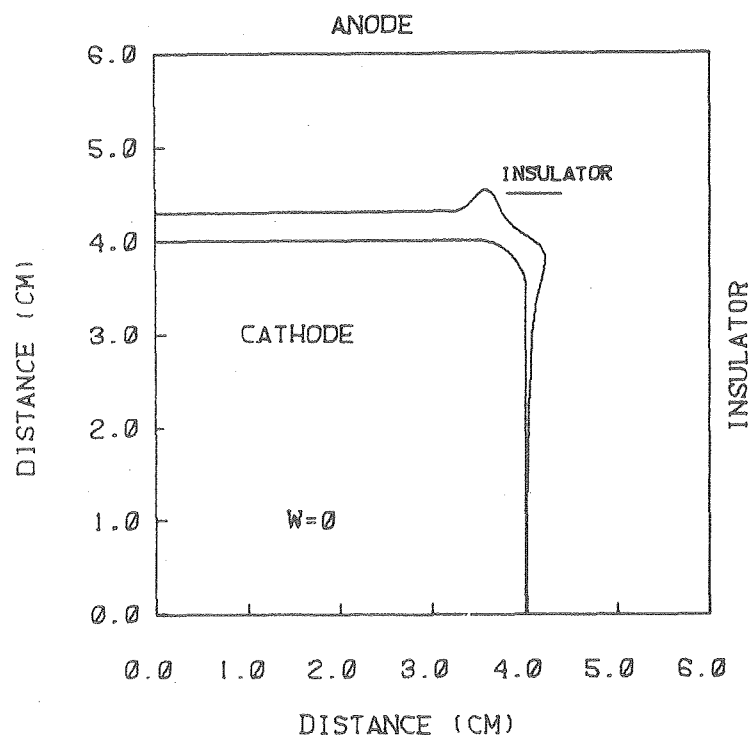
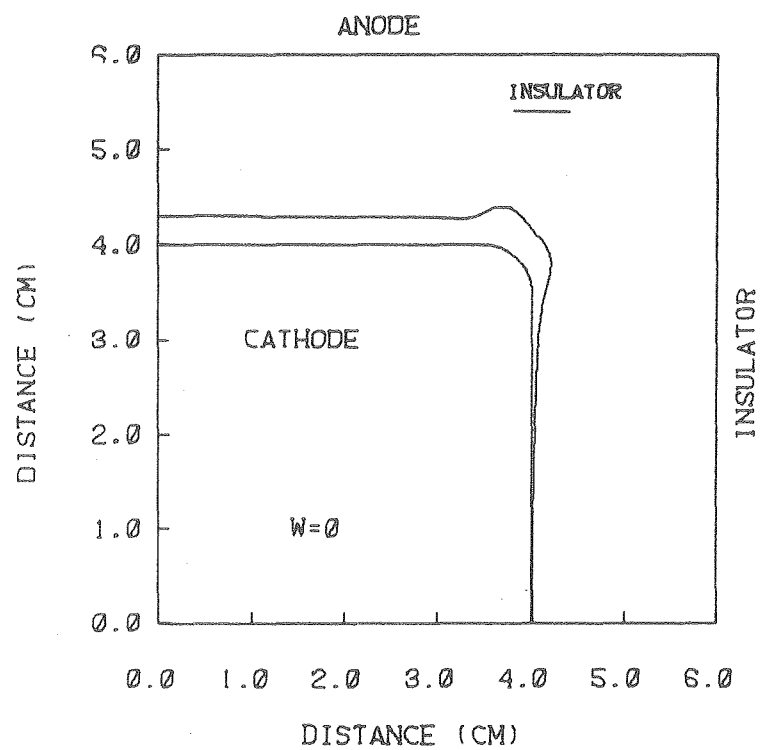


XBL 7910-12067

Fig. 38. Simulated deposition on a corner electrode. $W = 0$.

Fig. 39. Simulated deposition on a corner electrode. Same conditions as in Fig. 38 except for the insulator near the anode.

Fig. 40. Simulated deposition with an insulator near the cathode. Other conditions as in Fig. 38.

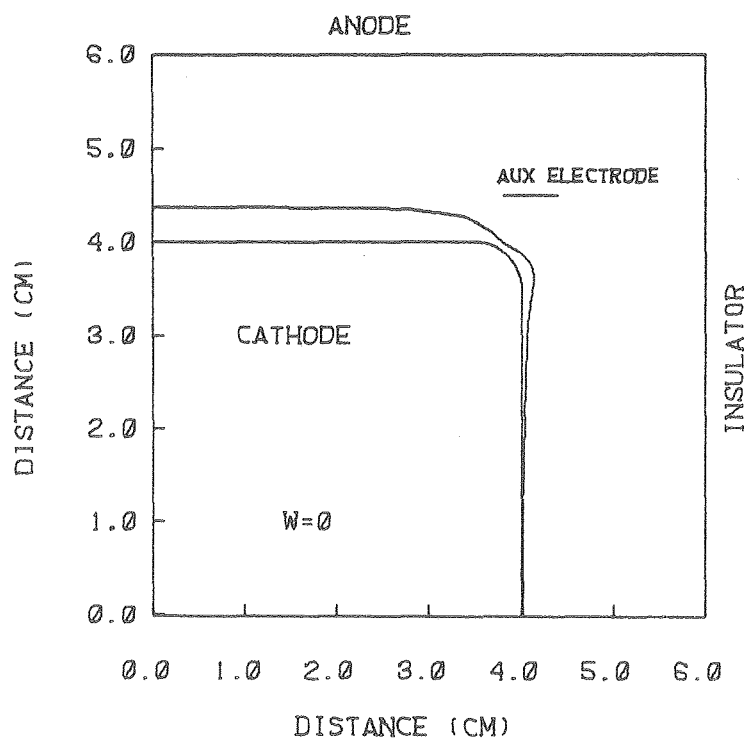
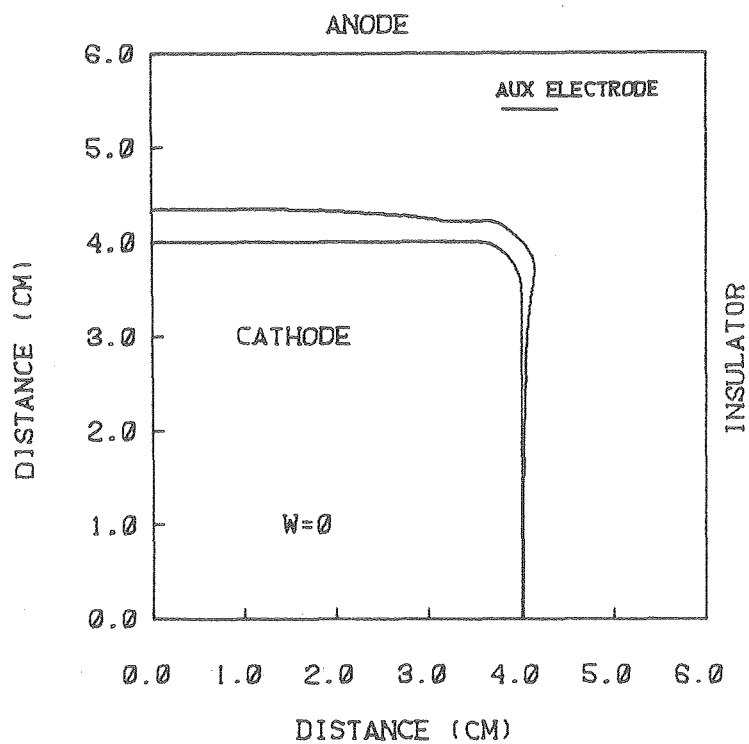


XBL 7910-12068A

Figs. 39-40

Fig. 41. Simulated deposition with an auxiliary electrode, at the same potential as the cathode, near the anode. Other conditions as in Fig. 38.

Fig. 42. Simulated deposition with an auxiliary electrode near the cathode. Other conditions as in Fig. 38.



XBL 7910-12070A

Figs. 41-42

simulations the optimum configuration is that shown in Fig. 41, where the auxiliary electrode is close to the anode. The deposit is most uniform and the formation of the peak is suppressed.

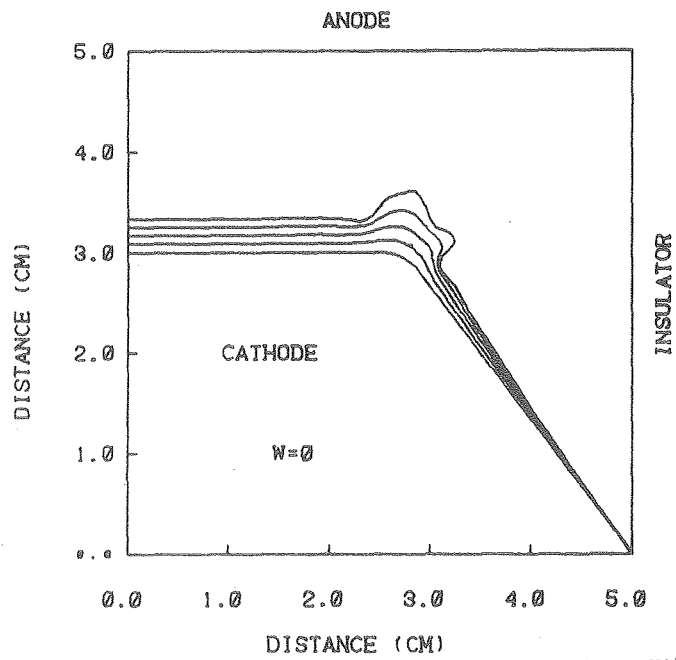
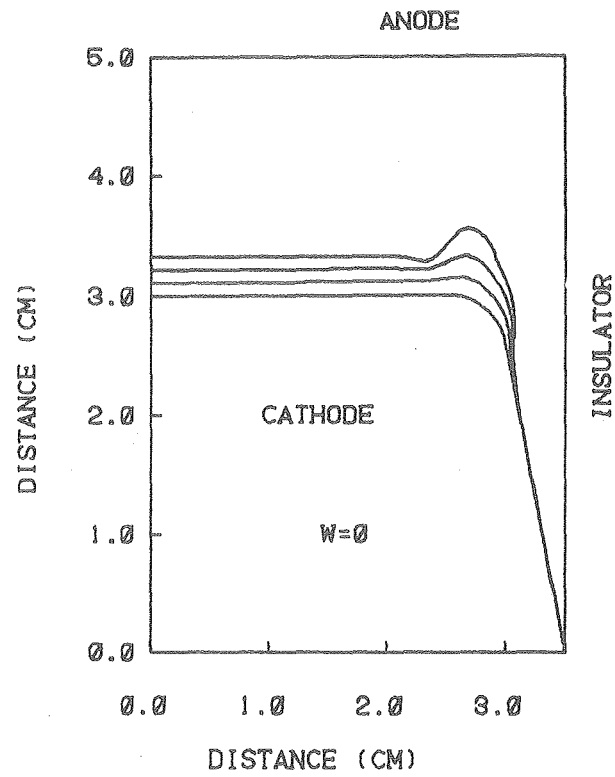
Deposition in a notch with kinetic resistance was studied. The geometric arrangement is similar to the corner electrode, but the side of the electrode that extends into the main recess intersects the insulator at an acute angle. From symmetry considerations this arrangement is equivalent to a cell where a mirror image is projected across the insulator. Such an equivalent cell forms a notch with an angle twice that between the insulator and the cathode.

Two geometric variations were studied: one where the angle between the cathode and the insulator was 11° and another where the angle was 40° . The primary current distribution displays the same characteristic features as those in the corner electrode problem (Figs. 43 and 44). Because of curvature effects, a local peak forms above the midpoint of the corner. Where an electrode forms an acute angle with an insulator, no current can flow to the point at the vertex in a primary current distribution.

As the Wagner number is increased, the peak at the corner is reduced, but little additional current flows to the base of the notch (Figs. 45 and 46). Even with the larger base angle, little additional current flows into the recess (Figs. 47 and 48). If the Wagner number is extremely large, the normal current density at each point approaches a constant value. The results of extreme kinetic control are shown in Figs. 49 and 50. In these cases the deposit approaches the insulator at an acute angle, and the deposit in the notch along the insulator

Fig. 43. Simulated deposition on a notch electrode. The angle between the insulator and the cathode is 11° . $W = 0$.

Fig. 44. Simulated deposition on a notch electrode. The base angle is 40° . $W = 0$.

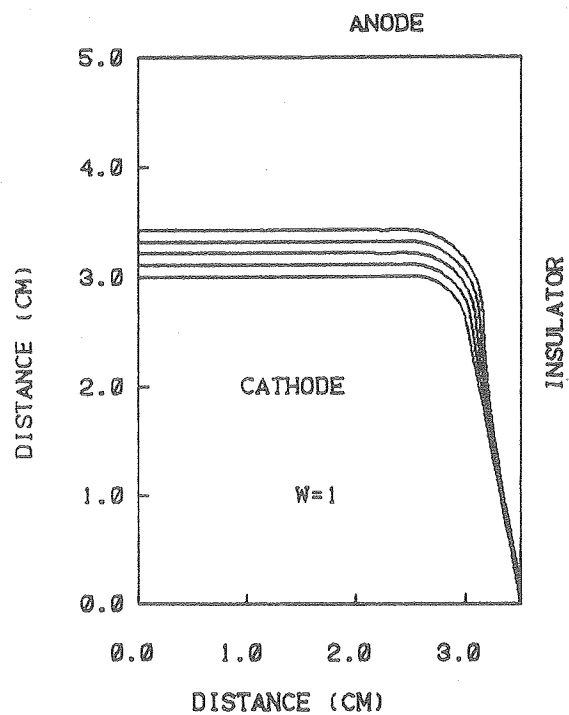
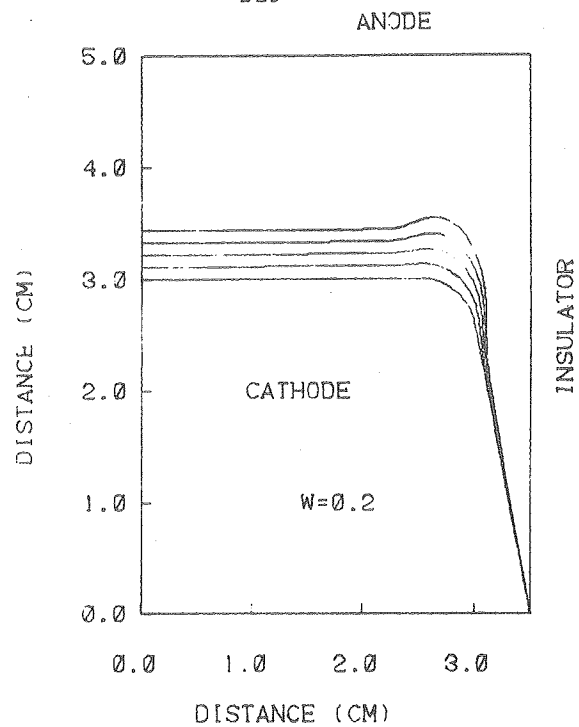


XBL 808-10854 A

Figs. 43-44

Fig. 45. Simulated deposition on a notch electrode. $W = 0.2$, base angle is 11° .

Fig. 46. Simulated deposition on a notch electrode. $W = 1$, base angle is 11° .

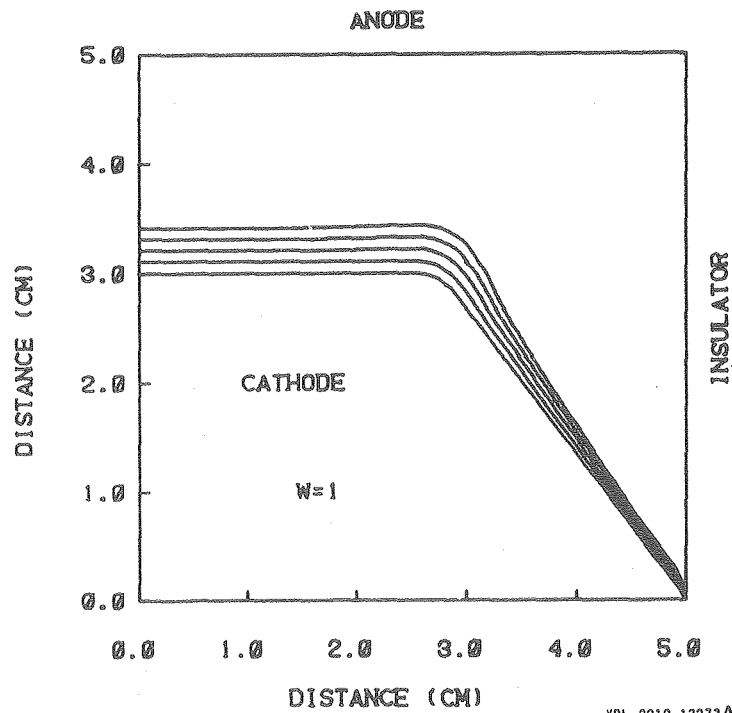
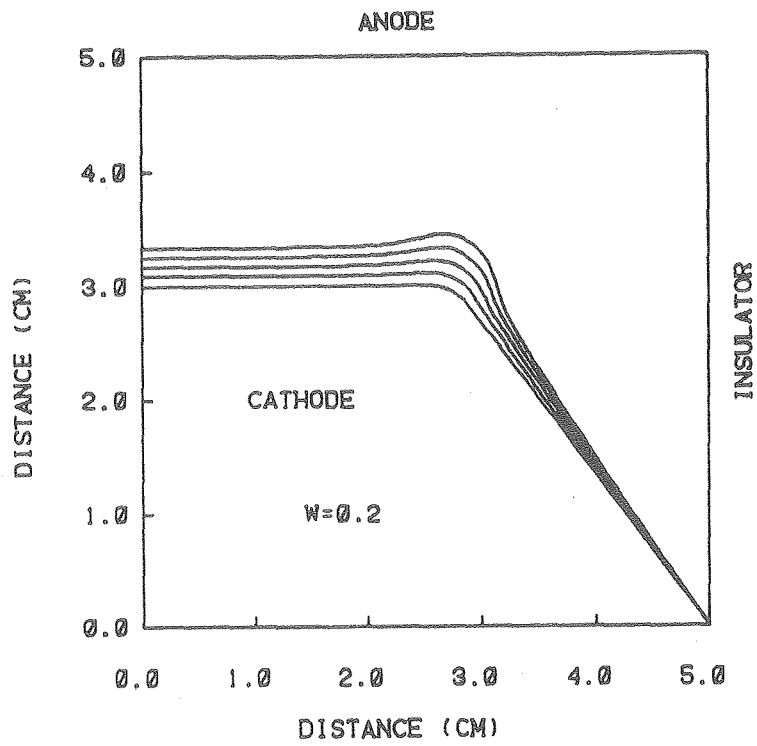


XBL 808-11195A

Figs. 45-46

Fig. 47. Simulated deposition on a notch electrode. $W = 0.2$,
base angle is 40° .

Fig. 48. Simulated deposition on a notch electrode. $W = 1$,
base angle is 40° .

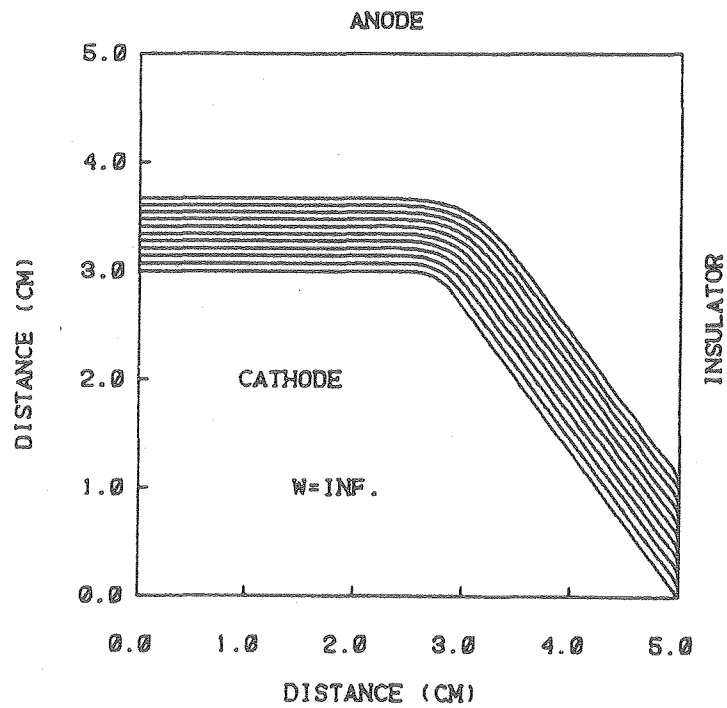
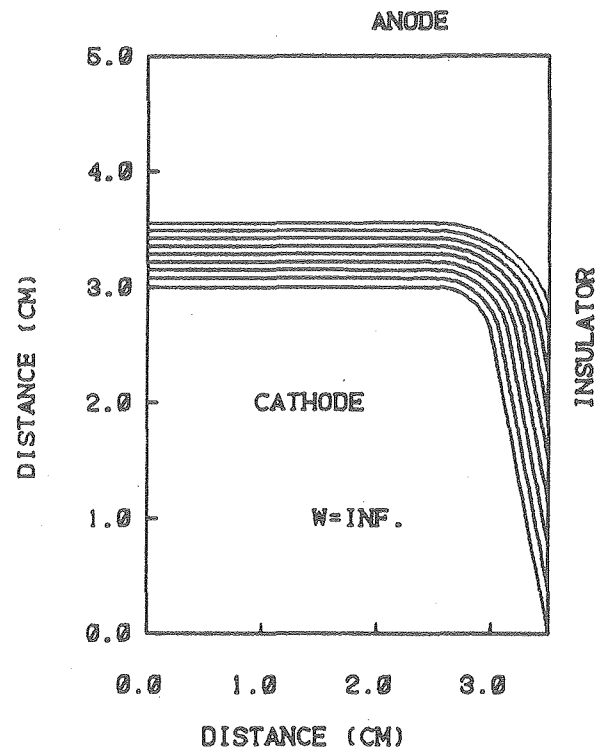


XBL 8010-12273A

Figs. 47-48

Fig. 49. Simulated deposition on a notch electrode. Constant local current density, base angle is 11° .

Fig. 50. Simulated deposition on a notch electrode. Constant local current density, base angle is 40° .



Figs. 49-50

XBL 808-10860A

grows faster than the deposit opposite the anode. The small angle notch closes faster than the large angle notch. This kind of leveling effect is referred to as geometric leveling. In this geometry the leveling efficiency can be defined as the ratio of growth along the insulator to the maximum growth on the electrode opposite the anode. The leveling efficiency is zero for a primary current distribution, and it is greater than one when a more uniform deposit results. The leveling efficiency is summarized in Table 13.

It is interesting to note that the corner grows toward the insulator faster than points below it in all cases studied where Wagner number was less than one. This implies that an occlusion, which will increase the deposit porosity, will form under the conditions studied. For those cases, where the ratio of maximum notch depth is less than one, a Wagner number greater than one is required in order to avoid large occlusions.

Mass Transport Effects on Sinusoidal Profiles

The effects of mass transport on growing sinusoidal profiles were studied. The surface concentration changes that result from ion depletion in the diffusion layer can affect the current distribution in several ways. The exchange current density is usually sensitive to concentration changes. In acid-copper electrolyte the exchange current density increases roughly with the square root of cupric ion concentration. The decrease in cathodic surface ion concentration that accompanies the passage of current has the effect of lowering the exchange current density. This implies that $\partial \eta_s / \partial i$ becomes larger as the limiting current density is approached.

Table 13. Ratio of deposit at the base of the notch to the characteristic deposit thickness.

W	Base Angle 40°	Base Angle 11°
0	0	0
0.2	0	0
0.7	0.2	0.1
∞	1.5	5.2

The magnitude of the concentration overpotential also increases as the limiting current density is approached. In order to characterize this effect, a dimensionless quantity, analogous to the Wagner number, can be defined. Since the surface overpotential increases logarithmically in the high current density regime, it is reasonable to evaluate $|\partial\eta_s/\partial i|$ at an average current density; however, since the concentration overpotential increases rapidly at high fractions of limiting current, it is appropriate to evaluate $|\partial\eta_{cn}/\partial i|$ where the current density is a maximum. A dimensionless number that characterizes mass transport effects can be defined as

$$W_{cn} = \kappa |\partial\eta_{cn}/\partial i|_{i_{\max}} / L \quad (42)$$

In order to calculate the reactant ion concentration at the electrode surface, the transport of the ionic species through the mass transport boundary layer must be computed. Unless the hydrodynamics is well-defined, this computation is extremely complicated. Considerable simplification can be realized by estimating an effective mass transport boundary layer thickness. For certain macroprofiles it is reasonable to assume that the boundary layer follows the profile. For a microprofile where the boundary layer is thick compared with the average surface roughness, it is appropriate to assume that the boundary layer follows the average surface plane. The surface concentration can be assumed to vary linearly with fraction of limiting current.

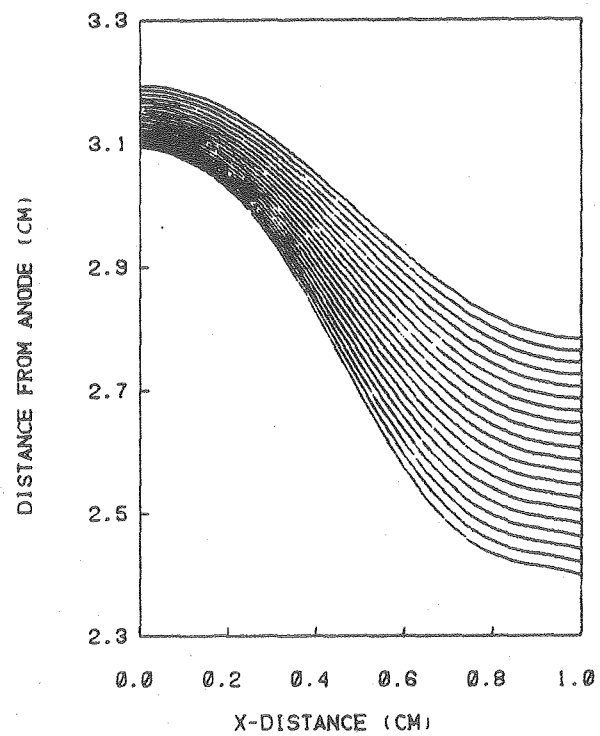
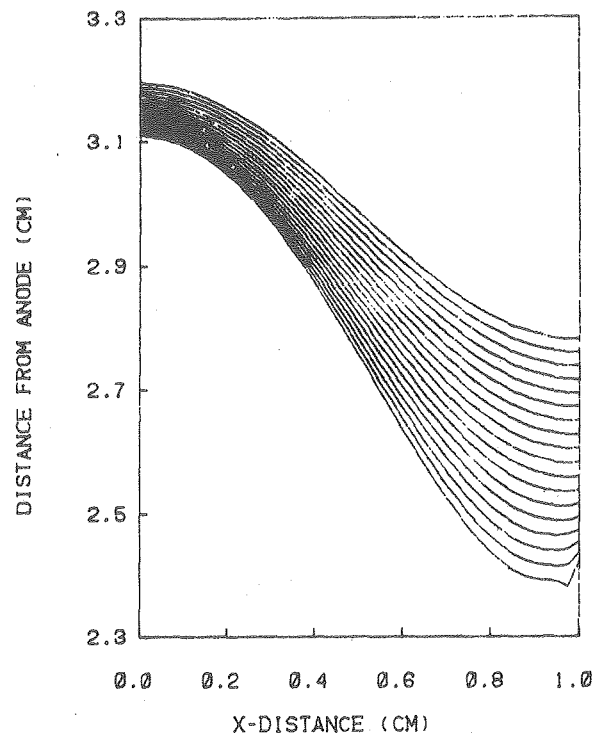
The apparent exchange current density can be affected by decreasing reactant concentration as well as by leveling agents. In one series of simulations the exchange current density was assumed to vary with the local fraction of limiting current (see Eq. 5). On the macroprofile depicted in Fig. 51, the boundary layer was assumed to be of constant thickness, and W_{cn} was assumed to be zero. At a Wagner number of 0.18, the depression at the peak, characteristic of low Wagner number simulations, appears after the peak advances approximately $1.1 A_0$. Growing profiles in the same system were also simulated under the assumption that the exchange current density decreased linearly with current density, as might be appropriate for a leveling agent. With the same applied potential the Wagner number is 0.45 (Fig. 52). Because of this increase in W , the depression at the peak is suppressed, and more uniform growth is realized.

Cases where the surface overpotential was zero but where concentration overpotential was appreciable were also considered. The simulation in Fig. 53 was run with $W_{cn} = 0.3$ and $W = 0$. With significant concentration overpotential a more uniform current distribution is obtained, and the depression at the peak does not appear. If the concentration overpotential is reduced ($W_{cn} = 0.05$), the depression at the peak is again manifested (Fig. 54).

Because W_{cn} increases rapidly at high fractions of limiting current, the current distribution exhibits a characteristic behavior under mass transport control, which is distinct from the behavior under charge transfer control. When mass transport control dominates on a sinusoidal profile, the concentration overpotential falls rapidly

Fig. 51. Simulated deposition on a sinusoidal profile. $A_0/\lambda = 0.1$,
 $W = 0.2, \gamma = 0$.

Fig. 52. Simulated deposition on a sinusoidal profile. $A_0/\lambda = 0.1$,
 $W = 0.45, \gamma = 1$.



Figs. 51-52

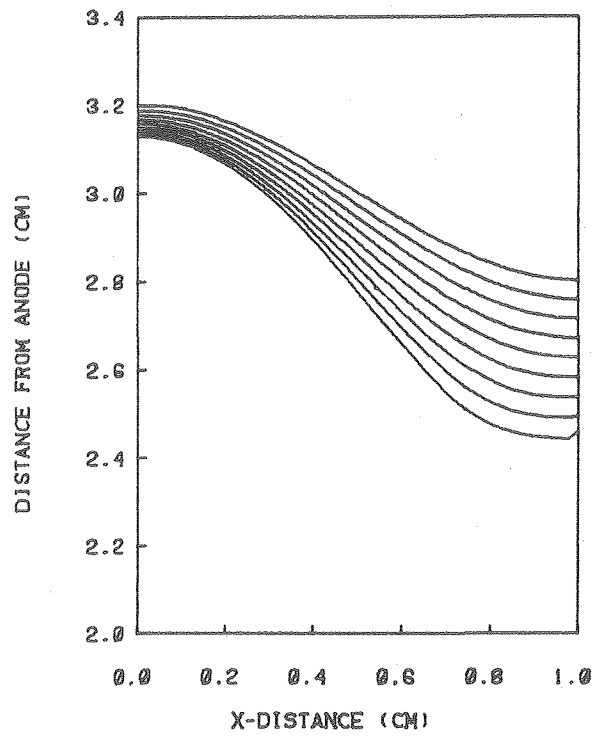
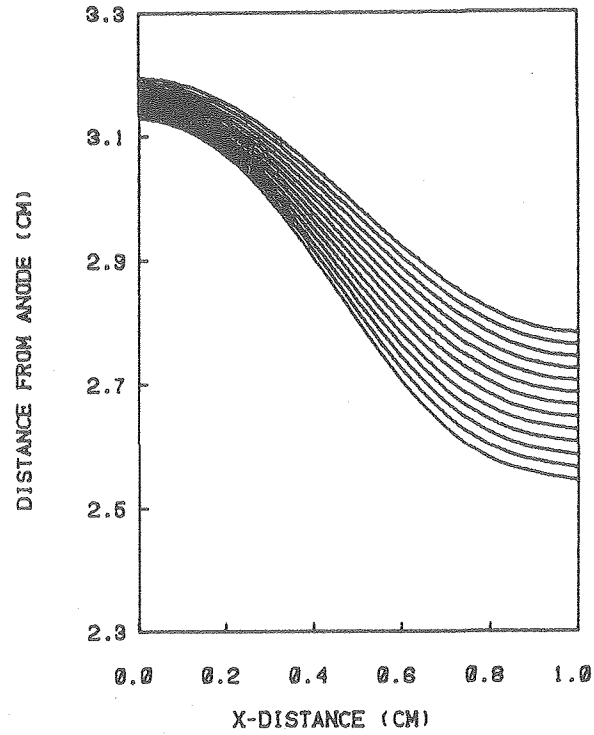
XBL 809-11777A

Fig. 53. Simulated deposition on a sinusoidal profile. $A_o/\lambda = 0.1$,

$W = 0.45$, $\beta = 1$.

Fig. 54. Simulated deposition on a sinusoidal profile. $A_o/\lambda = 0.1$,

$W_{cn} = 0.05$.



Figs. 53-54

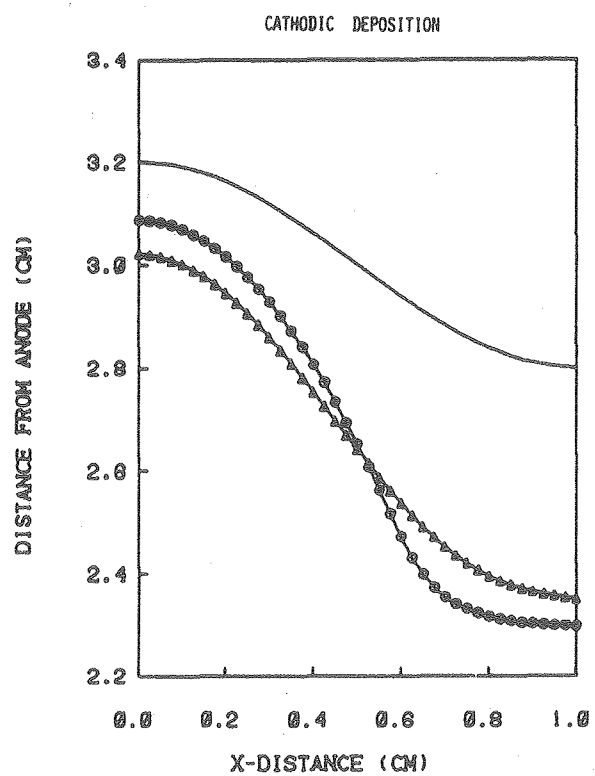
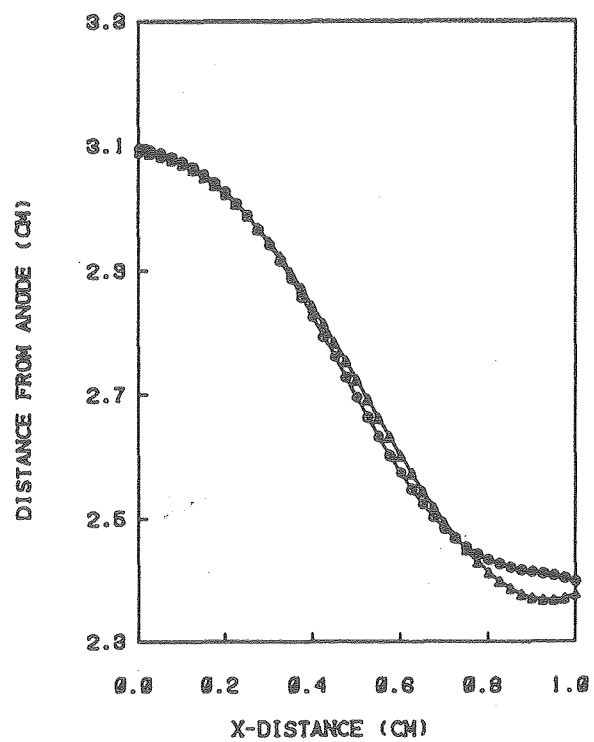
XBL 809-11775A

where the current density decreases most rapidly, near the peak. The rapid drop in overpotential near the peak causes more current to flow to that area. On successive profiles this phenomenon causes a broad flattening of the peak. Although a shoulder forms away from the peak, the rapid increase in concentration overpotential reduces the tendency for diversion of current to that area, and no depression forms at the peak. The contrasting behavior of mass transport and charge transport controlled profiles is illustrated in Fig. 55. Equal quantities of charge have been passed in the two simulations. At $W = 0.4$ the peak grows fastest, and the profile begins to sharpen away from the peak; however, with significant mass transport control ($W = 0.18$, $W_{cn} = 0.21$), the broad flattening of the peak occurs. When the kinetic resistance is increased above the corresponding mass transport resistance (Fig. 56), more uniform growth is realized, but the characteristic broad flattening does not occur.

On microprofiles the diffusion layer is thick compared with the average surface roughness. In this case the diffusion layer follows the average surface plane, rather than following the detailed profile. In order to facilitate comparison with the above simulations, the same initial profile was used. Although it is a macroprofile, the diffusion layer can be assumed to be correspondingly thicker to maintain similarity. The simulations shown in Fig. 57 were carried out under similar conditions ($W = 0.18$, $W_{cn} = 0.2$) except that a thick ($2A_0$ from the peak) diffusion layer, which follows the average surface plane, was assumed in one case; a thin diffusion layer, characteristic of a macroprofile, was assumed in the other. The characteristic flattening

Fig. 55. Simulated deposition on a sinusoidal profile. $A_o/\lambda = 0.1$;
(o) $W = 0.18$, $W_{cn} = 0.21$; (Δ) $W = 0.4$.

Fig. 56. Simulated deposition on a sinusoidal profile. (o) $W = 0.2$,
 $W_{cn} = 0.3$; (Δ) $W = 1.3$.



XBL 808-10957B

Figs. 55-56

Fig. 57. Simulated deposition on a sinusoidal profile. The diffusion layer is approximately 0.4 cm ($2A_0$) from the peak at each time step, and it is parallel to the anode. $W = 0.18$, $W_{cn} = 0.2$.

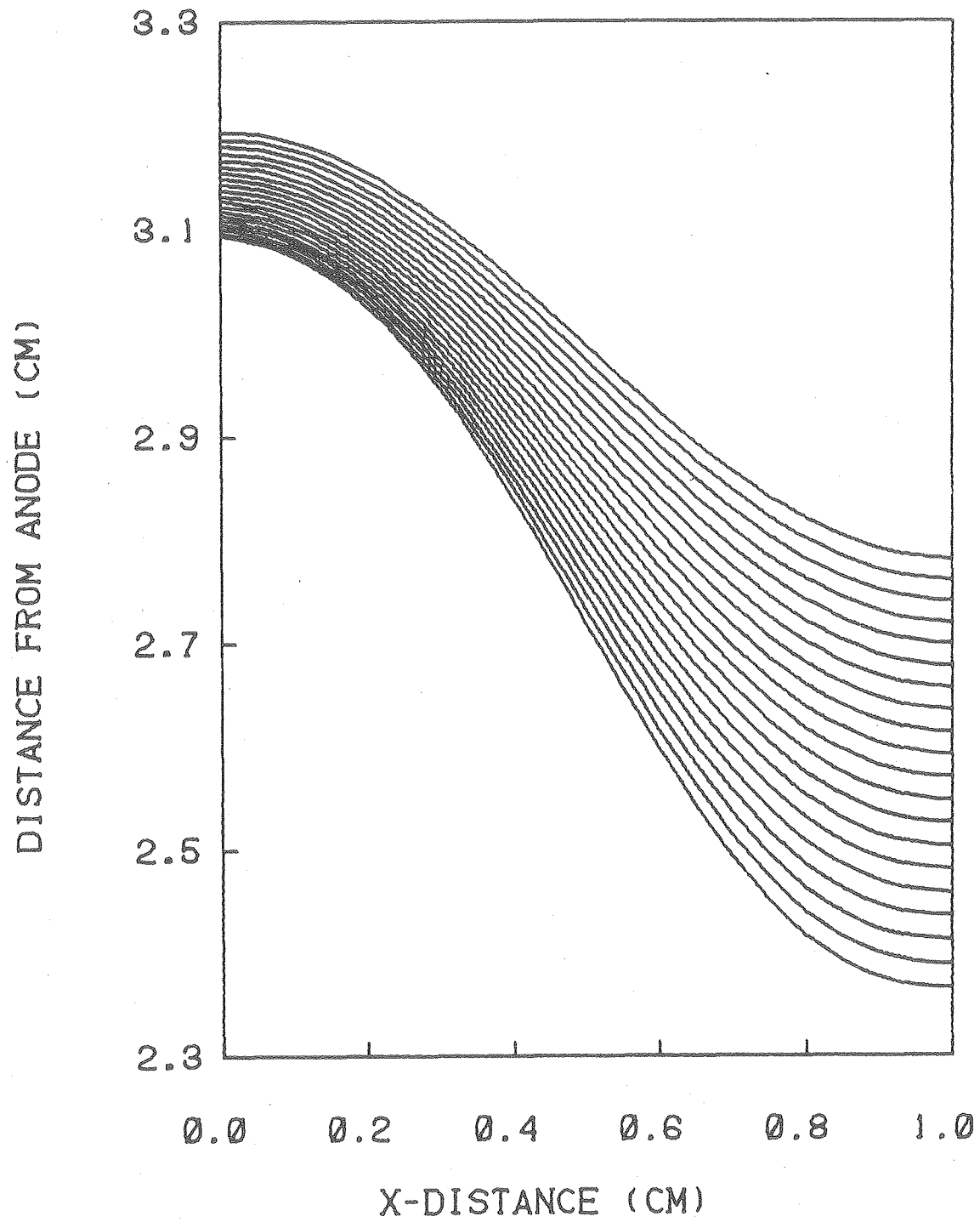


Fig. 57

XBL 809-11779

associated with the macroprofile under mass transport control does not occur when a thick diffusion layer is assumed. These differences can be explained by examining the behavior of the concentration overpotential, which is a function of both the local current density and the local diffusion layer thickness. On the initial profile the diffusion layer decreases sinusoidally along the X-axis; however, the current density decreases more rapidly near the peak (see Fig. 23). As a result, the concentration overpotential decreases more rapidly near the peak, and the flattening associated with mass transport limitations on the macroprofile does not occur.

Anodic Dissolution of a Sinusoidal Profile

In an electropolishing process the reduction of surface roughness is accomplished by preferentially dissolving the protruding features. Wagner⁸ modeled the roughness as a sinusoidal form. He derived an expression for the time-dependent change in amplitude for a diffusion-controlled process. Under the prescribed conditions Wagner demonstrated the mathematical equivalence of the diffusion-controlled problem and the ohmically controlled problem (primary current distribution). Because of the assumption that the normal current density is approximately equal to the current density component normal to the average surface plane, the solution is only valid where the amplitude-to-wavelength ratio (A/λ) is low.

A numerical simulation of the same problem was performed. The behavior of the dissolving profile for an initial amplitude-to-wavelength (A_0/λ) ratio up to 0.3 was examined. Although Wagner assumed that the sinusoidal shape is maintained during dissolution, the peak dissolves

preferentially, and some distortion of the form occurs. As a result, the peak and the recess are no longer equidistant from the average surface plane, and another definition of the amplitude must be invoked. I have chosen to define the apparent amplitude as half of the peak to recess distance. The average surface plane is defined as the mean distance of the profile from a reference plane. With these definitions quantitative comparisons with the results of other investigators can be performed.

Wagner's expression for the change in amplitude with time for a displacement of the average surface plane u is

$$\ln(A/A_0) = -2\pi u/\lambda \quad (43)$$

A plot of $-\ln(A/A_0)/(2\pi u/\lambda)$ vs A_0/λ (Fig. 58) for the numerical solution reveals the resulting differences. The solid line represents the relative change in amplitude extrapolated to $u/\lambda \rightarrow 0$, where the maximum differences occur. For larger u/λ , Wagner's assumption of small A/λ is a better one, and the differences become smaller. The differences are also small if A_0/λ is small. The current density in the recess is always underestimated in Wagner's analysis. It is zero in the recess for an A/λ of $1/2\pi$; thus, the leveling efficiency is always higher than that predicted by other methods.

More recently, Fedkiw²⁵ employed a regular perturbation technique to solve the dissolving sine wave problem. By including fourth order terms, he gave a better approximation for the current distribution. One of the equations resulting from his analysis expresses the ratio of the current density in the recess to the average current density

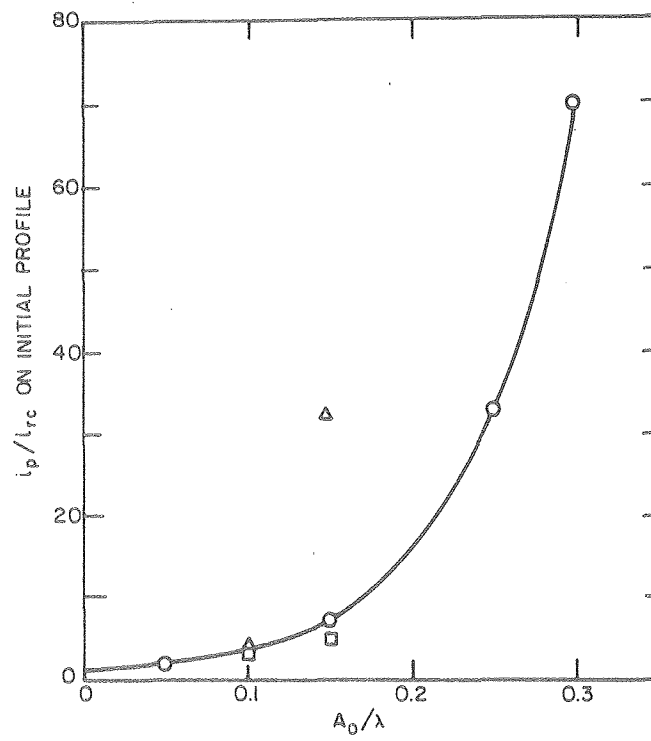
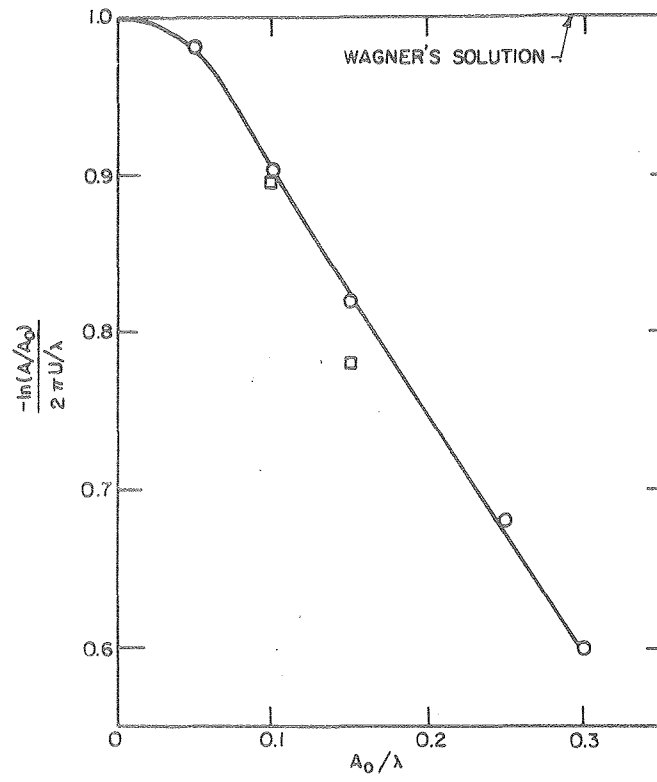
$$i_{rc}/i_{av} = 1 - 2\pi A/\lambda + 2(\pi A/\lambda)^3 + 8/3 (\pi A/\lambda)^4 + O(A/\lambda)^5 \quad (44)$$

Fedkiw noted that Wagner's solution is given by the first 2 terms in Eq. (44). It is clear that the series diverges for A/λ greater than $1/\pi$ and cannot be used in that range; moreover, i_{rc}/i_{av} increases with increasing A/λ for A/λ greater than 0.15. The relative current density in the recess must always decrease with increasing relative amplitude; hence, the four term expansion is insufficient to describe the current density for A/λ greater than 0.15. The results of this analysis for the relative change in amplitude are plotted on Fig. 58. The predicted leveling efficiency tends to be somewhat lower than that predicted by the numerical result. The ratio of maximum to minimum current density on the initial profile is illustrated in Fig. 59. It is clear that the perturbation solution is superior to Wagner's solution in the A_0/λ range of 0.1 to 0.15.

The displacement of the average surface plane required to dissolve a specified fraction of the original amplitude provides a useful measure of the leveling efficiency. The distance, expressed in terms of the original amplitude, that the surface plane must recede in order to dissolve half the original amplitude is plotted in Fig. 60. Since the peak and the recess are nearly equally accessible for low A_0/λ , the profile must traverse a distance equivalent to 10 original amplitudes before the amplitude is reduced by half. By contrast, for $A_0/\lambda = 0.3$, a half amplitude reduction is accomplished as the average surface plane recedes by a half amplitude.

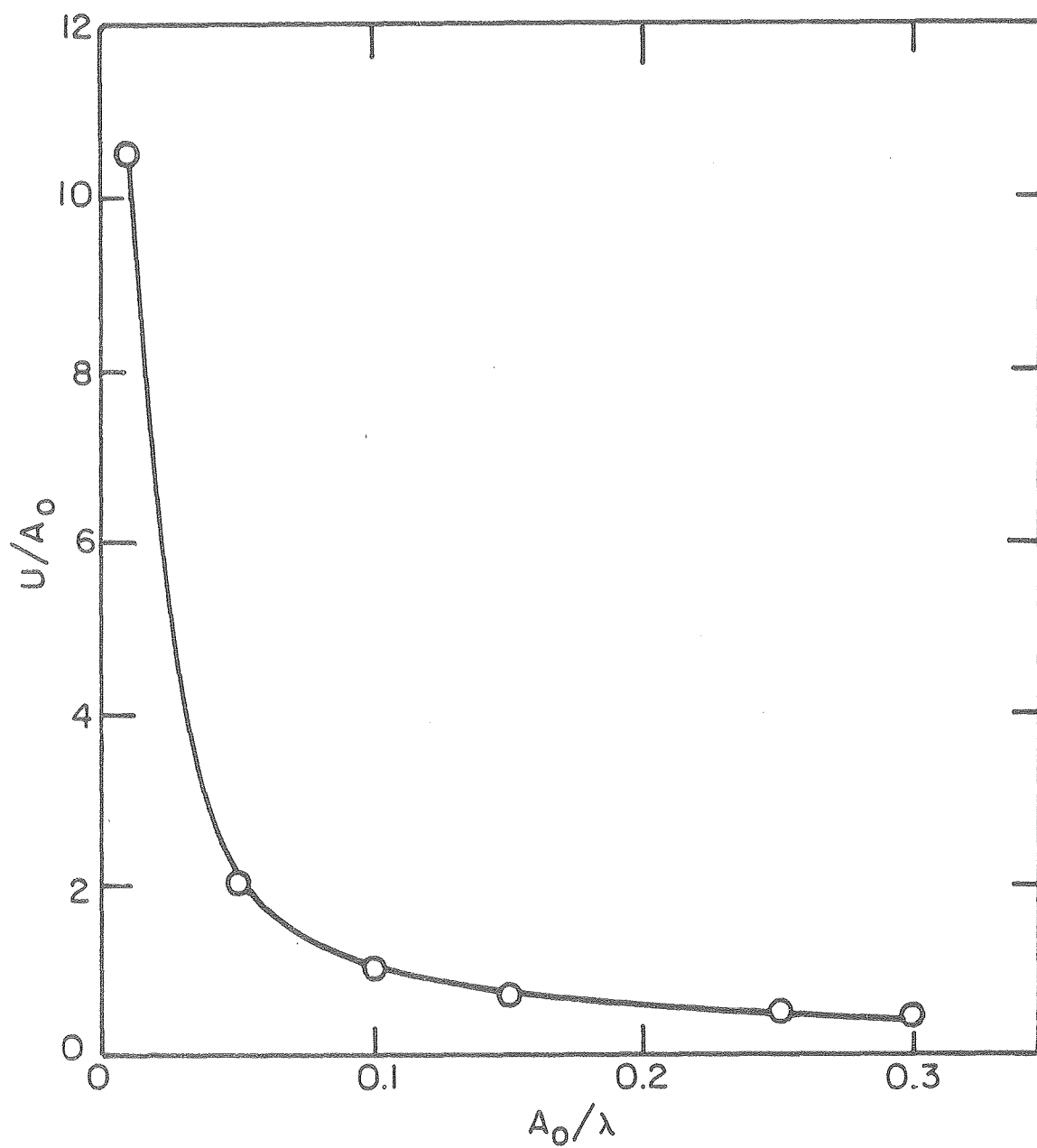
Fig. 58. Comparison of Wagner's solution with the numerical solution (o) and Fedkiw's solution (\square) for the dissolution of a sinusoidal profile.

Fig. 59. Ratio of current density on the peak to current density in the recess as a function of the initial amplitude-to-wavelength ratio. (o) numerical solution, (\square) Fedkiw's solution, (\triangle) Wagner's solution.



XBL808-5750A

Figs. 58-59



XBL 808-5748

Fig. 60. The number of amplitudes required to dissolve half of the original amplitude.

9. SUMMARY AND CONCLUSIONS

A model for simulating the transient behavior of electrodes undergoing deposition or dissolution has been developed. The model accounts for ohmic drop, charge transfer overpotential, and mass transport limitations. Although only two-dimensional and axisymmetric systems were simulated, the methods developed can readily be extended to three-dimensional shapes.

Finite difference techniques were used in the computer simulations. A solution for the primary current distribution simulations can always be obtained; however, convergence will not necessarily be attained for secondary and tertiary current distribution problems. An algorithmic procedure to overcome the instabilities inherent in these cases has been developed. With this procedure convergence has been attained for all reasonable values of the physical parameters. General guidelines for determining the computational parameters (convergence criteria, mesh size, time step interval) have been established, and error limits have been estimated.

Carefully controlled electrodeposition experiments were performed in a contoured rotating cylinder electrode system. Two sinusoidal profiles were machined on different stainless steel cylinders. The amplitude-to-wavelength (A_0/λ) ratio was 0.1 in both cases, but the actual dimensions were greater by a factor of 7 for the larger profile.

Experiments were performed with these two cylinders where the Wagner number was varied between 2 and 20. Because rough deposits were obtained in the acid-copper bath at current densities in excess of 50 mA/cm^2 ,

all successful experiments were performed at average current densities between 25 mA/cm^2 and 40 mA/cm^2 .

When the Wagner number is low, the current density variation on the profile is greatest. In these cases a shoulder tends to form near the peak, where the current density and curvature variations are relatively high. As the shoulder grows, the increased curvature in that area causes current to be diverted from the peak, where a depression forms. When the Wagner number is high, the current density is more uniform, and no depression at the peak occurs.

The kinetic parameters were determined from polarization curves obtained on copper rotating cylinders. These parameters, along with other physical property and geometric data, were incorporated in simulations of the growing sinusoidal profiles. Based on the deposit thickness, the simulated and experimental profiles generally agreed to within 10 percent. The depression at the peak for the low Wagner number runs was predicted by the simulations.

Since the formation of a depression at the peak of the sinusoidal profile was unexpected, this phenomenon was explored further. Primary current distribution simulations were performed with electrodes of different geometries, viz. sinusoidal, circular, parabolic, and biquadratic. The formation of a sharp peak was favored in cases where the curvature effects were relatively unimportant, e.g., the low A_0/λ sinusoidal profile or where the peak was initially sharp, e.g., the low focal length parabolic profile. In the cases that fell between these extremes, the formation of a shoulder away from the peak, and the formation of a depression at the peak was favored. As the Wagner

number is increased on any profile studied, these effects are either manifested at later growth stages or are totally suppressed.

Simulations of deposition on a rounded corner were performed. Several variations with different geometric and polarization parameters were studied. The primary current distribution simulation displayed a characteristic peak that formed above the midpoint of the corner. At a later growth stage the sharpened peak attracted sufficient current from the immediate surroundings so that depressions formed on either side of the peak. As the Wagner number was increased, the peak became less pronounced, and at a Wagner number on the order of one, the peak was no longer discernable. As the electrode separation was changed, slightly different peak characteristics were manifested, but at higher Wagner numbers these differences were minimized.

The characteristics of the primary current distribution simulations in a notch were similar to those for the corner problem. When the angle in the notch is small, little deposition occurs at the base of the notch. With the primary current distribution, for all angles no deposition at the base of the notch occurs. Geometric leveling was demonstrated for the case of constant local current density, i.e., at infinite Wagner number.

The effects of mass transport on growing sinusoidal profiles were considered. The depletion of reactant concentration that accompanies the passage of cathodic current reduces the exchange current density. When this dependence is taken into account, a more uniform current distribution results. As the limiting current density is approached, the concentration overpotential becomes significant. The functional depend-

ence of the concentration overpotential and surface overpotential on the current density is markedly different. Because the concentration overpotential increases rapidly at high fractions of limiting current, a broad flattening of the peak results when the current density at the peak approaches the limiting current density. The surface overpotential increases logarithmically in the high current density range. This slower increase in surface overpotential causes the resulting profiles to be more uniform.

On microprofiles mass transport limitations result in growth patterns that are different from the changes occurring on macroprofiles. When the diffusion layer is thick compared with the average roughness, the diffusion layer follows the average surface plane. In contrast to the mass transport controlled behavior of the macroprofile, the advancing microprofile under corresponding conditions does not exhibit the characteristic, flattened peak.

Simulations of sinusoidal profiles undergoing anodic dissolution were performed. These simulations were compared with Wagner's analytical results. Because of the assumptions that Wagner invoked in order to obtain a solution, his prediction of the time-dependent decrease in amplitude is accurate to within a few percent for an initial amplitude-to-wavelength (A_0/λ) ratio of less than 0.05. Numerical results were obtained for A_0/λ up to 0.3. The simulations performed at high A_0/λ showed that the initial rate of change of amplitude, computed by Wagner, was in error by at least 20 percent.

APPENDIX A

PROGRAM DESCRIPTION

The function of each routine of the computer program for calculating the successive profiles of a sinusoidal cathode undergoing deposition is outlined in this section; the details of each routine are described in the next section.

Main Program CURDIS

All of the geometric, physical, and computational parameters are read-in, and initial estimates for the surface potentials are calculated. The largest portion of the program is devoted to the iterative solution of Laplace's equation by the finite difference equation detailed in Appendix F. The overpotentials are computed from the polarization equations (some form of Eqs. 3 and 6). From the value of the total current, calculated in subroutine CURBAL, the time step is computed from the specified charge per time step (Eq. 9). The new coordinates of the boundary points are calculated from Eqs. 14 and 15. The convergence decisions are all made in this routine. The decision to halt the computation after the total specified charge has been passed is also made in the main program.

Subroutine CONFAC

The weighting factor D in Eq. 11 is calculated in this routine.

Subroutine CURBAL

In this subroutine the total current is calculated from Eq. 8.

Subroutine CURCAL

The calculation of the current density at each surface node, described in appendices G and H, is performed in this routine.

Subroutine CURMAP

The function of this routine is to print out the coordinates of the moving electrode after each converged time step. In addition, the current density, the derivative at each surface node, and other geometric information are also printed out.

Subroutine DEP

The values of the polynomials comprising the cubic spline, which describes the electrode boundary, are calculated. The coefficients in the simultaneous equations of the cubic spline form a tridiagonal matrix, which is solved for the surface derivatives in the subroutine TOMET. The ordinates at the original abscissa values are then computed.

Subroutine GEOM

The coordinates of the electrode at time zero are defined in this routine.

Subroutine GFAC

The distance from the electrode to node points adjacent to the electrode is computed from the spline polynomials. These values are stored for use in computation of the potentials.

Subroutine IEST

The initial estimates of all the potentials in the bulk are calculated by linearizing the potential between the anode and cathode.

Subroutine INVSPL

The coordinates of the profile between the surface nodes are calculated from the interpolating polynomials of the cubic spline.

Subroutine PMAP

Values of the potentials at each node can be printed out from this routine.

Subroutine SETUP

The number of grid points between the electrodes at each abscissa value is established in this routine.

Subroutine SMOOTH

Least squares smoothing of the electrode coordinates (prior to interpolation) can be performed to lessen the tendency for unstable behavior.

Subroutine SPLN

The derivative at each of the surface nodes is computed from the cubic spline.

Subroutine TOMET

The unknowns in simultaneous equations, where the coefficient matrix is tridiagonal, can be determined by the Thomas Method.¹⁶

APPENDIX B

PROGRAM DETAILS

Each section of the main routine and the subroutines is described below. The program variables are defined in the nomenclature section. Each statement is numbered by the MNF 4 compiler, and all references are to the numbers which appear to the left of each statement in the program listing. A problem involving deposition on a sinusoidal cathode is used to illustrate some of the features of the program (see Appendix E).

Main Routine CURDIS

- 1-96 All program parameters are read-in. Zero is the default option for all variables which do not need to be defined.
- 97 The initial geometric arrangement of the cathode is defined in subroutine GEOM.
- 98-123 The program variables are initialized here. All potentials must be positive. A value of -64 indicates that no value has been specified for the potential of a given node.
- 126-129 The initial estimate of the surface potential for linear polarization can be determined explicitly. The distance between the anode and cathode at the specified coordinates KC,IC is used to solve for the surface potential PT(KC,IC) in the one-dimensional problem.
- 130-146 For Tafel kinetics the surface potential cannot be determined explicitly; however, the Newton-Raphson method converges quickly on the correct surface potential. The concentration overpotential can also be included in the calculation (see Appendix J).

- 147-148 Initial estimates of the current density and time step are calculated here.
- 149-155 Each surface node is initially set at the same potential, calculated in previous sections. Alternatively, a surface potential can be specified (PT1).
- 156 The grid is constructed in subroutine SETUP.
- 157-169 The coordinates of the profile can be punched on cards for later plotting.
- 170 The derivative at each surface node is computed in subroutine SPLN.
- 171 The initial estimates for the potentials in the bulk electrolyte are computed in IEST.
- 172-180 The counterelectrode surface is set equal to the anode potential.
- 182 The initial geometric parameters are printed out in CURMAP.
- 184-192 The initial error matrix is set equal to zero.
- 201 The distance to the surface from adjacent nodes is calculated and stored in subroutine GFAC.
- 208 The iterative solution of Laplace's equation begins here.
The methods shown in Appendix F are used to calculate the potentials. The arrangement of node points that are calculated in each section are illustrated in Appendix K.
- 222-227 The potentials for equally spaced nodes in the main grid (low node density) are calculated in this loop.

- 228-237 The potentials for equally spaced nodes in the auxiliary grid (high node density) are calculated in this loop. The potential for nodes adjacent to the boundary is not calculated in this section.
- 238-253 The auxiliary grid for nodes adjacent to the boundary in the J+1 position are calculated in this loop (see Appendix K, Fig. a). The normalized difference in potentials between iterations is stored in the E array. If the difference is greater than the error criterion, NEC is incremented to signal that continued iteration is required.
- 265-291 The main grid potentials for the first row are calculated in this loop. The point in the I-1 position may be in the main grid (statement 272, Appendix K, Fig. b) or in the auxiliary grid (statement 279, Appendix K, Fig. c).
- 296-303 If the first row is an insulated border, the node in the I-1 position takes the same value as the node in the I+1 position (see Appendix K, Fig. d).
- 309-356 The potentials for the first row of the auxiliary grid are calculated in this loop. The potential at the I-1 node can be in the main grid of the previous block (statement 316, Appendix K, Fig. e). The node at the 1,1 location in the auxiliary grid is calculated at statement 342 (Appendix K, Fig. f). The potential for the node adjacent to the boundary is computed at statement 351 (Appendix F, Fig. g).

- 364-380 In this loop the potentials for the second last row of the main grid are computed. The $I+1$ node may be in the main grid of the next block (Appendix K, Fig. h) or in the auxiliary grid of the next block (Appendix K, Fig. l).
- 382-387 The potentials of the second last row for the last block are computed in this loop (Appendix K, Fig. j).
- 394-437 The calculation of the auxiliary grid potentials in the first and second last rows parallels that for the main grid.
- 439-449 The potentials for the $J=1$ points on the auxiliary grid are computed in this loop (See Appendix K, Fig. k).
- 450-455 The main grid potentials are equated to the auxiliary grid potentials where the points coincide.
- 456-570 The potentials of nodes adjacent to the surface where no node exists on the surface are calculated in this section. The distances to the boundary have previously been calculated in subroutine GFAC. The potentials at the intermediate points are determined by linear interpolation. With these distances, the methods shown in Appendix A can be applied to these nodes. The statement numbers and corresponding illustrations in Appendix L are as follows: 484, Fig. a; 486, Fig. b; 489, Fig. c; 495, Fig. d; 529, Fig. e; 547, Fig. f; 554, Fig. g; 562, Fig. h.
- 572-616 The potentials for the last row and last block are computed in this loop.
- 617-629 The values of the potentials can be printed out at specified iterations.

- 631 If all potentials are converged, the current densities are calculated.
- 634-637 Loose convergence criteria allow intermediate calculation of the current densities even if all potentials are not yet converged.
- 641 The current densities are calculated in CURCAL.
- 650 The weighting factor D in Eq. (11) is computed in subroutine CONFAC. The details of the method are in the section on convergence procedure.
- 655-661 The coordinates of the maximum current density points are determined here. These coordinates are used if the maximum current density is a specified fraction of the limiting current.
- 664-671 The concentration overpotential is calculated in this loop.
- 685-691 Surface overpotential described by Tafel kinetics is calculated in this loop.
- 693-697 The overpotential from a linear polarization equation is computed in this loop.
- 701-707 The polarized electrode potentials are stored for the next iteration or timestep.
- 709-716 The Wagner number is recalculated in this section.
- 717-720 The convergence criteria must be met before moving the electrode boundary.
- 722-732 The currents on the anode and cathode are determined in subroutine CURBAL. A comparison of the two results gives a measure of the accuracy of the solution. The time step is calculated according the Eq. (7).

- 735-747 The new coordinates of the boundary are calculated in this loop (see Eqs. 11 and 13).
- 757 The optional subroutine SMOOTH performs least squares smoothing on the boundary.
- 760-763 The new coordinates, the derivatives, and the grid arrangement are computed in the subroutines DEP, SETUP, and SPLN.
- 764-778 After defining the new geometry the surface potentials from the previous iteration are used for the initial estimates. If convergence has not been achieved, the old values of the surface potentials are used for the next iteration.
- 781-792 The convergence status or the values for a converged solution are printed out in this section.
- 815 If convergence is not achieved after the specified number of iterations, the computation halts.
- 818 After the total charge has been passed, the computation is terminated.

Subroutine CONFAC

The weighting factor FP (D in Eq. 13) is computed in this section.

- 4-8 If the surface potential at the specified location (PT(KC,IC)) is proceeding in the same direction between iterations, the factor CFM is increased by 10 percent. If the potential reverses direction, this factor is reduced by 40 percent.
- 9 The factor CF reflects the variation in the current density (ACE) between iterations. For stability a large value of ACE requires a smaller weighting factor.

- 10-11 As the relative surface potential variation approaches a converged value, the factor CIF is reduced.
- 12 If the problem has not converged by the time 80 percent of the specified iteration limit is reached, the factor CIF is reduced. This procedure increases the chances of convergence for problems in which too few iterations have been specified.
- 14-17 The limits of ACE for which the factor CIF will be increased or decreased are calculated here. In the initial stages the minimum limit CMI is on the order of 5 percent, and the maximum limit CMA is on the order of 10 percent. As the surface potential variations decrease, the limits are reduced.
- 19-20 The factor CIF is increased by 20 percent if ACE is less than CMI and decreased by 50 percent if ACE is greater than CMA.
- 21 The weighting factor FP is calculated by multiplying the weighting components together.

Subroutine CURBAL

- 16-27 The approximate area AR of the cathode associated with each node is the auxiliary grid space divided by the cosine of the angle with the normal to the surface. A unit strip width (1 cm in this example) is assumed so that the current per unit electrode length is numerically equal to the current per unit area. The current density CD multiplied by the area increment AR gives the current CC. Summing these gives the total current CCT. Since only half of a grid space is associated with the

first and last nodes, these currents are calculated separately (CCL and CCL). The average cathodic current is the total current CCT divided by the total area AT.

29-49 The anodic current is determined by an analogous procedure. A three point numerical differentiation formula (see Appendix G) is used to determine the potential gradient and the current.

Subroutine CURCAL

19-36 The Y-component of the current density is calculated in this section. If the fractional distance FD between the surface and an adjacent node is less than 20 percent of a grid space, the adjacent point is ignored in the computation (see Appendix G).

38-51 The angle of the electrode is determined so that the appropriate nodes and distances are used in the calculation of the X-components of the current density.

52-56 If the nodes for the numerical differentiation fall in adjacent blocks or on an insulated border, special calculations must be performed. Control is transferred to the appropriate section for these special computations.

57 An image point is used for the calculation of the X-component of current density near an insulated border (see Appendix M, Fig. a).

60-61 Nodes from the previous block may be required in order to perform the differentiation (see Appendix M, Fig. b).

- 65-89 The potential at the node in an adjacent block is calculated in this section (see Appendix M, Fig. c). Quadratic Lagrangian interpolation is used to determine the potential in the adjacent block (see Appendix H).
- 92-94 For electrode surfaces in a recess, the X-component of current density is set to zero.
- 103-125 The interpolated potentials are calculated for use in the 3-point numerical differentiation formula.
- 128-139 The numerical differentiation is performed in this section.
- 140-165 If the angle of the normal to the surface with respect to the established coordinate system is greater than about 35 degrees (see Appendix G, Fig. a), the X-component of the current density on either side of the boundary node are calculated and a linear interpolation is performed to calculate the X-component at the given node.
- 166-185 The current density at each surface node is calculated from Eqs. 11 and 12. Since positive values of the current density are not physically possible, a reduced estimate for the current density is used in this case. The average normalized change in current density between iterations through this loop is also calculated here.

Subroutine CURMAP

The values of the current density, the coordinates of the system, and other pertinent data are printed out in this routine.

Subroutine DEP

In order to interpolate the ordinates back to the original abscissa values, a cubic spline is constructed through the new coordinates.

The ordinates can be obtained from Eq. 2.1.10 in Ahlberg et al.¹⁷ after solving the simultaneous Eq. 2.1.16 for the derivatives at the surface.

6-70 The coefficients ($\lambda(AM)$, $\mu(AM)$, and $C(C)$) for the simultaneous Eqs. 2.1.16 are determined in this section.

71 The values of the derivatives can be determined by solving the simultaneous equations by the Thomas method in subroutine TOMET.

90 The new ordinates are determined by Eq. 2.1.10.

Subroutine GEOM

The problem geometry is defined in this subroutine. The counter-electrode is assumed to be flat and perpendicular to the insulated walls.

In this example the distance between the anode and cathode is

$$Y = 3 + 0.2\cos(2\pi X/\lambda).$$

Subroutine GFAC

7-52 If no node exists on the surface in the I-1 position, the distance to the boundary is determined and stored for use in the potential calculation (see Appendix L). The distance can be calculated from an implicit solution of a cubic interpolating polynomial of the spline; the computation is performed in subroutine INVSPL.

53-62 The distance to the electrode surface, where no node exists in the I+1 position, is calculated here.

64-74 The distances to the I-1, J+1, and I+1 positions are stored in XL, XU, and XR, respectively.

Subroutine IEST

20-22 The potentials for the main grid are linearized for the initial estimates in the bulk electrolyte.

25-34 Linearization of the auxiliary grid potentials is performed for the initial estimate.

Subroutine INVSP

For a given ordinate, the abscissa value can be found by an implicit solution of an interpolating polynomial of the cubic spline. Newton's method is used to locate the root.

Subroutine PMAP

The values of the potentials at each node are printed out from this routine. The values can be printed out at any specified iteration, and the converged values can also be obtained.

Subroutine SETUP

The auxiliary grid is constructed in this section.

15-18 The point closest to the counterelectrode is determined in this loop.

19-30 Auxiliary nodes fill the grid that are the specified distance (NAS*DX) from the point closest to the counterelectrode.

33-40 The distance from the closest node to the surface is computed for each row and is stored in DU.

Subroutine SMOOTH

In this optional subroutine the coordinates of the boundary after passing charge, but before interpolating, can be smoothed by at least squares technique. The routine POLFIT, described in the Sandia Program Library,²⁷ fits the points to the lowest degree polynomial such that the rms error of all points is less than the specified criterion ER (in this example 2 microns).

Subroutine SPLN

The derivatives at each electrode surface node are determined from the cubic spline. The method, equations, and nomenclature are identical to those in subroutine DEP.

Subroutine TOMET

The Thomas method is used to invert a tridiagonal matrix. This matrix arises from the simultaneous equations used to solve for the the derivatives at the electrode surface. The nomenclature used in the program parallels that in Lapidus.¹⁶

APPENDIX C

PROGRAM VARIABLES

A	constant overpotential in $= A + Bi$
AA	alphanumeric title
ACE	average current error between iterations
AL	overrelaxation parameter 1.85
APHI	arctangent of absolute value of the derivative
AVI	average current density
B	1) linear overpotential slope 2) Tafel overpotential slope
BPE	error in surface potential
BV(K)	base vector; distance from counterelectrode to auxiliary grid
BVV, BVM, BVP, BVN	base vector
CAS	anodic charge/time step
CAT	anodic current
CCC	cathodic charge/time step
CCT	cathodic current
CD(K,I)	current density
CDO	exchange current density
CET	sum of normalized current errors
CF	current factor; the component of the weighting factor FP that is a function of the current error ACE

CFM consistency factor; weighting factor component that depends on whether the surface potentials are oscillating.

CIF component of weighting factor that increases as successive current errors stay within specified limits

CL limiting current density

CLC constant in limiting current calculations

CLM limiting current density

CMA maximum change in ACE above which CIF is decreased

CMI minimum change in ACE below which CIF is increased

CN current density

CON electrolyte conductivity

COV(K,I) concentration overpotential (V)

CPC concentration overpotential coefficient

CSA absolute value of the arctangent of $D(K,I)$

CZ $PT(KC,IC)$ at the iteration $r-1$

$D(K,I)$ derivative at electrode surface

DA distance to $J+1$ point

DC, DCF, DCZ variables to determine whether $PT(KC,IC)$ is changing in a consistent manner between iterations

DD $D(K,I)$

DEN electrode density

DF deposition factor; deposit volume/C

DL distance to $I-1$ point

DLD(K,I) diffusion layer depth

DM, DP are $DX(K)$

DMA, DPA are DXA(K)

DR distance to I+1 point

DT time step increment

DU(K,I) distance from electrode to point below

DV voltage difference

DVX potential in the X-direction

DVY potential gradient in the Y-direction

DX(K) main grid spacing

DXA(K) auxiliary grid spacing

DXL distance to I-1 point

DXV(K,I), DYV(K,I) DVX and DVY, respectively stored for output

DZ DX(K)

DZA DXA(K)

D2 DU(K,I)

E(I,J) relative potential error at I,J

EAV average potential error ET/IE

EE PN-PA(K,I,J)

EN relative normalized potential error

ERR convergence criterion for normalized potential error

ET sum of EN

FE Faradaic efficiency

FLC specified fraction of limiting current

FP weighting factor for surface potentials

FW formula weight

I row index
 IC specified row coordinate where current density is relatively
 high
 ICL iterations in the current loop (subroutine CURCAL)
 IE number of points used to compute EAV
 IGK IGR(K)
 ILM maximum specified iterations in potential loop
 IM, IN, INB row indexes
 IPOT flag to indicate whether converged potentials are to be printed
 out (1=yes, 0=no)
 IPU flag to indicate whether cards are to be punched (1=yes, 0=no)
 IS(K,I) row coordinate for points adjacent to electrode and in I+1
 or I-1 positions
 ITC iterations in current loop at a given time step
 ITM maximum specified number of time steps
 ITP iterations in potential loop after exiting current loop
 ITS number of time steps

 J column index
 JD, JH, JL, JR, JU column indexes
 JS(K,I) column index corresponding to IS(K,I)

 K block index
 KB total number of blocks
 KBM KB-1

KK, KM, KP block indexes
 KC block index where current is relatively high

 LIT iterations in potential loop
 LL(K) number of points of type IS,JS
 LLT LL(K)

 MA(K,I) number of columns in auxiliary grid at a given I
 MAA MA(K,I)
 ML(K) number of columns in main grid
 MLL ML(K)

 N NR(K)
 NAS(K) number of auxiliary squares of main grid dimensions to be
 generated between main grid and electrode
 NEC number of potentials tested exceeding the convergence criterion
 NIPO number of iterations in potential loop before calling subroutine
 PMAP

 NKM, NM, NMG, NMN, NM1, NM2, NN1 row counters
 NR(K) number of rows in auxiliary grid

 P(K,I,J) main grid potentials
 PA(K,I,J) auxiliary grid potentials
 PHI angle between electrode and x-axis
 PI 3.14
 PN potential at r+1 iteration

PO, PR, PL potentials

PRO proportionality factor for linear interpolation

PRP(K) potential to the right of P(K,NMG-1,MLM)

PT(L) surface potential

PT1 specified initial estimate for the surface potentials

RBE, RBM average and maximum normalized error in surface potentials,
respectively

T, T1, T2 temporary storage locations

TCA cumulative anodic charge passed

TCC cumulative cathodic charge passed

TIM time

VA anode potential

VC cathode potential

VCC variable convergence criterion

W block width

WC Wagner number for concentration overpotential

WCT Wagner number for charge transfer

WF $1/(1+WN)$

WN Wagner number

storage

Variables in Subroutine SMOOTH

A	work array used in subroutine POLFIT
ER	maximum rms error between the polynomial curve and the surface nodes. The lowest degree polynomial which is less than the rms error is used for smoothing
IERR	flag from POLFIT (1 is normal execution, 2 is error in input parameters, 3 is polynomial of degree greater than L is needed to meet the rms criterion.)
NORD	degree of polynomial used in the smoothing
R	ordinates of the polynomial at the specified abscissa XX
XX, YY	coordinates of surface nodes after deposition

APPENDIX D
PROGRAM LISTING

CURDIS	PROGRAM CURDIS(INPUT,OUTPUT,PUNCH)**	PAGE 1
1.	0000008 PROGRAM CURDIS(INPUT,OUTPUT,PUNCH)	
2.	0015448 DIMENSION AA(10),CCV(1,101),CLD(1,101),E(101,101),IS(1,101), SJS(1,101),LL(6),PRP(6),AL(1,101),XR(1,101),XC(1,101)	
3.	0015448 CCMON/BCHG/XN(1,101),YN(1,101)	
4.	0015448 CCMON/BLCAT/SV(6),DX(6),DXA(6),IGR(6),KB,ML(6),NAS(6),NR(6)	
5.	0015448 CCMON/CONC/CDV	
6.	0015448 CCMON/CONF/ERR,TER,PTC,RBE,FEM,WF,LIT,ILM,ITC,CZ,DCZ,CFM,CIF, SCF,CMI,CMA,FP	
7.	0015448 CCMON/CURCC/DXV(1,101),DYV(1,101),ACE	
8.	0015448 CCMON/CURDEN/CD(1,101)	
9.	0015448 CCMON/DRIV/D(1,101)	
10.	0015448 CCMON/NITS/ITS	
11.	0015448 CCMON/POL/A,B,CDC,CON,VA,VC	
12.	0015448 CCMON/PRT/IPRT	
13.	0015448 CCMON/UPDIS/DU(1,101)	
14.	0015448 CCMON/YDIS/Y(1,101),MA(1,101)	
15.	0015448 CCMON P(1, 51, 51),PA(1,101,101),PT(1,101)	
16.	0015448 READ IC,(AA(L),L=1,10)	
17.	0266708 10 FORMAT(10A8)	
18.	0266708 PRINT 15,(AA(L),L=1,10)	
19.	0266778 15 FORMAT (//10X,1CA8//)	
20.	0266778 READ 20,A,B,CDO	
21.	0267C58 20 FORMAT(3E10.2)	
22.	0267058 IF((B.EQ.0).AND.(A.NE.0)) GO TO 29	
23.	0267128 IF((B.AND.CDO).EQ.0.) GO TO 24	
24.	0267148 IF(CDO.EQ.0.) GO TO 27	
25.	0267168 PRINT 21,B,CDO	
26.	0267248 21 FORMAT (1* TAFEL POLARIZATION PARAMETERS B= *1PE10.2* VOLTS 10= * *1PE10.2* A/CHSQ*)	
27.	0267248 GC TO 40	
28.	0267248 24 PRINT 25	
29.	0267308 25 FORMAT(1* PRIMARY CURRENT DISTRIBUTION**)	
30.	0267308 GC TO 40	
31.	0267308 27 PRINT 28,A,B	
32.	0267368 28 FORMAT (1* LINEAR POLARIZATION PARAMETERS A= *1PE10.2* VOLTS *B= *1PE10.2* V/(A/CHSQ) *)	
33.	0267368 GO TO 40	
34.	0267368 29 PRINT 30,A	
35.	0267438 30 FORMAT(1* CONSTANT OVERPOTENTIAL OF A= *1PE10.2* VOLTS**)	
36.	0267438 40 CONTINUE	
37.	0267438 READ 50,KB,(AR(K),K=1,KB),(NAS(K),K=1,KB)	
38.	0267618 50 FORMAT(16I5)	
39.	0267618 READ 52,(CX(K),DXA(K),K=1,KB)	
40.	0267748 52 FORMAT(16F5.3)	
41.	0267748 PRINT 60	
42.	0267778 60 FORMAT(5X,*BLOCK*5X*MAIN GRID*5X*AUX GRID*5X*AUX SQUARES*5X*WIDTH * (CM)**)	
43.	0267778 DC TO K=1,KB	
44.	0270018 N=NR(K)	
45.	0270018 W=FLOAT(N-1)*DXA(K)	
46.	0270048 PRINT 65,K,DX(K),DXA(K),NAS(K),W	
47.	0270218 65 FORMAT(5X,13,6X,F9.3,10X,F5.3,10X,15,10X,F5.3/)	
48.	0270218 70 CONTINUE	
49.	0270238 READ 80,VA,VC	
50.	0270318 80 FORMAT (2F10.5)	
51.	0270318 PRINT 85,VA,VC	
52.	0270368 85 FORMAT(2X,*ANODE POTENTIAL= *F10.5* CATHODE POTENTIAL= *F10.5*	

PROGRAM CURCIS(INPUT,OUTPUT,PUNCH)

CURCIS

```

53. 0270368 READ 90,AL
54. 0270420 50 FORMAT(5,2)
55. 0270420 PRINT 91,AL
56. 0270468 91 FORMAT(8) OVERRELAXATION PARAMETER=5,2)
57. 0270468 READ 100,ERR
58. 0270528 100 FORMAT(2E10,2)
59. 0270528 DELIMT 105,ERR
60. 0270568 105 FORMAT(8) CONVERGENCE CRITERION=1PE10,2)
61. 0270568 READ 120,ILM,ITM
62. 0270638 120 FORMAT(21,5)
63. 0270638 PRINT 125,ILM,ITM
64. 0270700 125 FORMAT(8) MAX FIELD ITERATIONS=150 MAX TIME STEPS=15)
65. 0270700 READ 130,NIPD
66. 0270748 130 FORMAT(15)
67. 0270748 PRINT 132,NIPD
68. 0271008 135 FORMAT(8) POTENTIAL MAP OUTPUT EVERY=150 ITERATIONS=1
69. 0271008 READ 140,CCN
70. 0271048 140 FORMAT(1E10,2)
71. 0271048 PRINT 145,CCN
72. 0271108 145 FORMAT(8) ELECTROLYTE CONDUCTIVITY=1PE1C,2*(CM-CM)-10)
73. 0271108 READ 150,FM,DM,Z,FE
74. 0271178 150 FORMAT(4F10,5)
75. 0271178 DE=FE*FM/1965000*(2*DM)
76. 0271238 PRINT 155,FM,DM,Z,FE,DE
77. 0271348 155 FORMAT(18) FORMULA HT=10,50 G/G-A DENSITY=10,50 G/CC VAL
78. 0271348 *NCE=10,50 FARADAY EFF=FC,50 DEP FACTOR=1PE12,50*CC/CC+
79. 0271348 160 FORMAT(121,5)
80. 0271348 READ 160,KC,IC
81. 0271418 PRINT 165,KC,IC
82. 0271468 165 FORMAT(8) COORDINATES OF HIGH CC POINTS K=150 I=15)
83. 0271468 C LIMITING CURRENT=CLC/DLICK,1)
84. 0271548 READ 170,CPC,CLC,DLT
85. 0271548 170 FORMAT(3E10,2)
86. 0271548 CLM=CLC/DLT*(1-E-30)
87. 0271548 PRINT 180,CPC,CLC,DLT,CLM
88. 0271668 180 FORMAT(8) CPC,R1/N=1PE10,20 *NFC(BULK)*1PE10,20 * DIFFUSION LAYER
89. 0271668 $,1PE10,20 *CN LIM CURRENT=1PE10,2)
90. 0271668 READ 80,CCOUL
91. 0271728 PRINT 192,CCOUL
92. 0271728 192 FORMAT(8) COULOMBS/TIME STEP=1PE15,5)
93. 0271768 READ 130,IPU
94. 0271768 READ 130,IPU
95. 0271768 READ 183,PII
96. 0271768 READ 183,PII
97. 0271768 183 FORMAT(10,5)
98. 0271768 PRINT 185,PII
99. 0272228 185 FORMAT(8) SPECIFIED FRACTION OF LIMITING CURRENT=10,5)
100. 0272228 C READ INITIAL GEOMETRY
101. 0272228 CALL GEOM
102. 0272228 C INITIALIZE VARIABLES
103. 0272248 AL=1-AL $ WA=0 $ WF=1 $ TIM=0 $ IIS=0 $ ITP=0 $ DT=0
104. 0272248 ACE=0 $ CCC=0 $ TCC=0 $ TCA=CSTER-100*ERR
105. 0272248 DC 190 K=1,K8
106. 0272248 N=NRK1
107. 0272248 DC 190 I=1,N
108. 0272248 PTK,1)=64
109. 0272248 COIK,1)=0 $ DIK,1)=0 $ COVIK,1)=0 $ DYVIK,1)=0 $ DXVIK,1)=0.

```

CURDIS		**PROGRAM CURDIS(INPUT,OUTPUT,PUNCH)**	PAGE 3
119.	0272538	DLD(K,I)=DLY	
120.	0272548	XN(K,I)=(I-1)*DXA(K)	
121.	0272578	DO 190 J=1,101	
122.	0272638	190 PA(K,I,J)=-64.	
123.	0272768	PT(KC,IC)=VC	
124.	0273018	IF(B.EQ.0.) GO TO 225	
125.	0273038	IF(CDC.NE.0.) GO TO 214	
C INITIAL ESTIMATES OF SURFACE POTENTIAL FOR LINEAR POLARIZATION			
126.	0273058	WN=B*CCN/Y(KC,IC) 9 PT(KC,IC)=(VC+WA*VA)/(1+BN)	
128.	0273178	WF=1./(1+BN)	
129.	0273218	GO TO 225	
C INITIAL ESTIMATE FOR TAFEL POLARIZATION			
130.	0273228	214 T1=CCN/(Y(KC,IC)*CCO)	
131.	0273268	CLM=CLC/(DLD(KC,IC)+1.E-30)	
132.	0273328	PT(KC,IC)=VA-1.E-3	
133.	0273368	DO 217 M=1,50	
134.	0273408	T3=CON*(VA-PT(KC,IC))/Y(KC,IC)	
135.	0273448	IF(CLC.EQ.0) CLM=1.E+15	
136.	0273518	IF(T3.GT.CLM) T3=.999*CLM	
137.	0273548	IF(FLC.NE.0) CLM=1.E+15	
138.	0273578	F=VC+B*ALOG(T1*(VA-PT(KC,IC)))-PT(KC,IC)-CPC*ALOG(1-T3/CLM)	
139.	0274008	DE=B/(PT(KC,IC)-VA)-1-CPC/(Y(KC,IC)*CLM/CON-VA+PT(KC,IC))	
140.	0274138	PT(KC,IC)=PT(KC,IC)-.5*F/DE	
141.	0274208	IF(ABS(F).LT.1.E-5) GO TO 220	
142.	0274208	217 CONTINUE	
143.	0274258	220 CONTINUE	
144.	0274268	WN=B/(Y(KC,IC)*(VA-PT(KC,IC)))+CCN*CPC/(Y(KC,IC)*CLM-CON*(VA-PT(KC,IC)))	
145.	0274408	WF=1./(1+BN)	
146.	0274428	225 CONTINUE	
147.	0274438	CD(KC,IC)=CCN*(VA-PT(KC,IC))/Y(KC,IC)	
148.	0274508	DT=DXA(KC)/(DF*CD(KC,IC))	
C INITIALIZE SURFACE POTENTIALS			
149.	0274538	VT=PT(KC,IC)	
150.	0274568	DC 230 K=1,K8	
151.	0274618	N=NR(K)	
152.	0274618	DO 230 I=1,N	
153.	0274658	PT(K,I)=VT	
154.	0274678	IF(PTI.NE.0) PT(K,I)=PTI	
C INITIALIZE CURRENTS AND CONC OVERPOTENTIAL			
155.	0274738	230 CONTINUE	
C SETUP GRID			
156.	0275008	CALL SETUP	
C PUNCH CARDS FOR PLOTTING			
157.	0275028	IF(IPU.EQ.0) GO TO 240	
158.	0275038	PUNCH 235,K8,K8	
159.	0275108	235 FORMAT (10I5)	
160.	0275108	PLACH 238,(DXA(K),K=1,K8)	
161.	0275208	238 FORMAT(13F6.4)	
162.	0275208	PUNCH 235,(NR(K),K=1,K8)	
163.	0275308	PUNCH 3202,ITS,TIM,TCC	
164.	0275368	DC 239 K=1,K8	
165.	0275408	API=NR(K)-1 8 IF(K.EQ.K8) NM1=NM1+1	
167.	0275458	PUNCH 238,(Y(K,I),I=1,AMI)	
168.	0275608	239 CONTINUE	

```

CURDIS      **PROGRAM CUDIS(INPUT,OUTPUT,PUNCH)**      PAGE      4
169. 0275628 C 240 CONTINUE
170. 0275638 C COMPUTE DERIVATIVES AT SURFACE ACDES
      CALL SPLN
C INITIAL ESTIMATES
C LINEARIZE POTENTIALS IN BULK ELECTROLYTE FOR INITIAL ESTIMATES
171. 0275658 C CALL IE51
      CALL IE51
C EQUATE LOWER POTENTIALS TO PG FOR ICK=1
      DC 257 K=1,K8
      ICK=IGRK) & N=NR(K)
      IF ICK=NR-1) GO TO 297
      DO 296 I=1,N,IGK
      IP=I/IGK+1
      PK,IN,I)=VA
172. 0275678 C 296 CONTINUE
173. 0275718 C 297 CONTINUE
174. 0275738 C 297 CONTINUE
175. 0275758 C 297 CONTINUE
176. 0275778 C 297 CONTINUE
177. 0275798 C 297 CONTINUE
178. 0276038 C 297 CONTINUE
179. 0276058 C 297 CONTINUE
180. 0276078 C 297 CONTINUE
181. 0276128 C 297 CONTINUE
182. 0276208 C 297 CONTINUE
      CALL CURMAP
C BEGIN NEW TIME STEP
C
183. 0276228 C 298 CONTINUE
184. 0276248 C 298 CONTINUE
185. 0276268 C 298 CONTINUE
186. 0276288 C 298 CONTINUE
187. 0276308 C 298 CONTINUE
188. 0276328 C 298 CONTINUE
189. 0276348 C 298 CONTINUE
190. 0276368 C 298 CONTINUE
191. 0276388 C 298 CONTINUE
192. 0276408 C 298 CONTINUE
193. 0276508 C 298 CONTINUE
      C CALCULATE GEOMETRIC FACTORS FOR NODES NEAR SURFACE
      CALL GFAC (AR,XU,XL,LL,IS,JS)
201. 0276578 C 299 CONTINUE
      C BEGIN ITERATION IN POTENTIAL LOOP
      C
202. 0276628 C 300 CONTINUE
203. 0276648 C 300 CONTINUE
204. 0276668 C 300 CONTINUE
205. 0276688 C 300 CONTINUE
206. 0276708 C 300 CONTINUE
207. 0276728 C 300 CONTINUE
208. 0276748 C 300 CONTINUE
209. 0276768 C 300 CONTINUE
210. 0276788 C 300 CONTINUE
211. 0276808 C 300 CONTINUE
212. 0276828 C 300 CONTINUE
213. 0276848 C 300 CONTINUE
214. 0276868 C 300 CONTINUE
215. 0276888 C 300 CONTINUE
216. 0276908 C 300 CONTINUE
217. 0276928 C 300 CONTINUE
218. 0276948 C 300 CONTINUE
219. 0276968 C 300 CONTINUE
220. 0276988 C 300 CONTINUE
221. 0277008 C 300 CONTINUE
      C CALCULATE MAIN GRID POTENTIALS IN BULK
      C
222. 0277028 C 310 I=2,NN
223. 0277048 C 310 J=2,MLM
224. 0277068 C 310 J=2,MLM
225. 0277088 C 310 J=2,MLM
226. 0277108 C 310 J=2,MLM
227. 0277128 C 310 J=2,MLM
      C CALCULATE AUXILIARY GRID POTENTIALS IN BULK
      C
228. 0277148 C 400 I=2,NN2

```

CURDIS		**PROGRAM CURDIS(INPUT,OUTPLY,PUNCH)**	PAGE 5
229.	027744B	YL=Y(K,I-1) \$ YR=Y(K,I+1) \$ MA2=MA(K,I)-2	
232.	027751B	DO 400 J=2,MA2	
233.	027755B	YP=(J-1)*DZA+BVV	
		C DC NOT COMPUTE BCRDER PTS	
234.	027760B	IF(VL.LT.YP.CR.VR.LT.YP) GO TO 400	
235.	027764B	PN=(PA(K,I-1,J)*PA(K,I,J+1)+PA(K,I+1,J)+PA(K,I,J-1))/4.	
236.	027773B	PA(K,I,J)=PA(K,I,J)*AI+PN*AL	
237.	030002B	400 CONTINUE	
		C	
		C 2ND LAST COL	
		C	
238.	030007B	DO 420 I=2,NM2	
239.	030010B	J=MA(K,I)-1 \$ YP=(J-1)*DZA+BVV	
241.	030015B	IF(Y(K,I-1).LT.YP.CR.Y(K,I+1).LT.YP) GO TO 420	
242.	030022B	DZ=DU(K,I) \$ T1=DZ+DZA	
244.	030025B	PA=(PA(K,I-1,J)+PA(K,I+1,J))*DZ/(2.*T1)+DZA*(PA(K,I,J+1)*DZA +DZ* *PA(K,I,J-1))/(T1*T1)	
		C CHECK CONVERGENCE OF POTENTIALS	
245.	030045B	EN=(PN-PA(K,I,J))/PN \$ IE=IE+1	
247.	030054B	IF(K.NE.KC) GO TO 410	
248.	030056B	E(I,J)=EN	
249.	030062B	410 CCNTINUE	
250.	030063B	EI=ET+ABS(EN)	
251.	030065B	IF(ABS(EN).GT.ERR) NEC=NEC+1	
252.	030072B	PA(K,I,J)=PA(K,I,J)+AL*(PN-PA(K,I,J))	
253.	030100B	420 CONTINUE	
		C	
		C CALC 1ST ROW	
		C	
254.	030102B	IF(K.EQ.1) GO TO 440	
255.	030104B	KM=K-1 \$ DM=DX(KM) \$ CMA=CXA(KM)	
258.	030110B	BVM=BV(KM) \$ AKP=NR(KM)-1	
260.	030113B	NPN=NR(KM)/IGR(KM)	
261.	030116B	YR=Y(K,2) \$ YL=Y(KM,NKM)	
263.	030122B	44C CONTINUE	
264.	030124B	IF(IGK.EQ.1) GO TO 700	
		C	
		C CALCULATE MAIN GRID (MG) POTENTIALS	
265.	030125B	DC 650 J=2,MLM	
266.	030130B	YP=(J-1)*DZ+1.E-8	
267.	030133B	IF(K.EQ.1) GO TO 540	
		C CHECK IF ABOVE MAIN GRID CF PREVIOUS BLOCK	
268.	030136B	IF(YP.GE.BVM) GO TO 500	
269.	030140B	LP=Y/DH+1 \$ PRO=(YP-(LP-1)*DM)/DM \$ DXL=DM	
272.	030147B	PL=P(KM,NMN,LP)*(1-PRO)+PRO*P(KM,NMA,LP+1)	
273.	030156B	GO TO 600	
274.	030156B	500 CCNTINUE	
		C CALCULATE POTENTIAL CF POINT IN PREVIOUS BLOCK	
275.	030163B	YC=YP-BVM \$ LP=YC/DMA+1 \$PRO=(YD-(LP-1)*DMA)/DMA \$ DXL=DMA	
279.	030170B	PL=PA(KM,NKM,LP)*(1-PRO)+PRO*PA(KM,NKM,LP+1)	
280.	030200B	GO TO 600	
281.	030200B	540 CCNTINUE	
282.	030202B	IF(IGK.EQ.1) GO TO 670	
		C FIRST ROW, FIRST BLOCK, MAIN GRID	
283.	030203B	PL=P(1,2,J) \$ DXL=DZ	
285.	030207B	600 CONTINUE	
286.	030211B	T1=DXL+DZ	
287.	030212B	PN=DXL*DZ*(PL+DZ/DXL+P(K,2,J))/(T1*T1)+DXL*(P(K,1,J+1)+P(K,1,J-1))	


```

CURDIS          **PROGRAM CURDIS(INPUT,OUTPUT,PUNCH)**          PAGE      7
C FOR I=1, J=MA1
345. 0305038 785 CCNTINUE
346. 0305058 IF(IY(K,2).LT.VP) GC TO 790
347. 0305078 IF(K.EQ.1) GO TC 786
348. 0305118 IF(IY(KM,NKM).LT.VP) GC TO 790
349. 0305118 786 CONTINUE
350. 0305168 D2=DU(K,1)
351. 0305178 PN= ((PL*DZA+PA(K,2,MA1)*DXL)/(DXL+CZA)+DXL/(DZA+D2))*PA(K,1,J+1)
      **DZA+PA(K,1,J-1)*D2)/D2)/(1.+DXL/D2)
352. 0305448 EE=PN-PA(K,1,MA1) $ EN=EE/PN
354. 0305508 PA(K,1,MA1)=PA(K,1,MA1)+AL*EE
355. 0305558 IF(ABS(EN).GT.ERR) NEC=NEC+1
356. 0305628 790 CONTINUE
C
C FOR 2ND LAST ROW
C
357. 0305648 800 CONTINUE
358. 0305658 I=AMG-1
359. 0305668 IF(K.EQ.KB) GO TC 865
360. 0305708 BVP=BVP(KP) $ DP=DX(KP) $ DPA=DPA(KP)
363. 0305748 IF(IGK.EQ.1) GC TC 870
C
C FOR MG
364. 0305778 DO 860 J=2,MLM
365. 0306018 YP=(J-1)*DZ+1.E-8
366. 0306048 IF(YP.GT.BVP) GC TC 830
C FOR MG IN NEXT BLOCK
367. 0306078 LP=Y/DP+1 $ PRC=(YP-(LP-1)*EP)/DP
369. 0306148 PR=P(KP,1,LP)*(1-PRC)+PRD*P(KP,1,LP+1)
370. 0306228 GC TO 850
C FOR AG IN NEXT BLOCK
371. 0306228 830 CONTINUE
372. 0306248 YD=Y/DP-BVP $ LP=YD/DPA+1 $ PRO=(YD-(LP-1)*DPA)/DPA
375. 0306338 E50 CCNTINUE
376. 0306358 PR=PA(KP,1,LP)+PRO*(PA(KP,1,LP+1)-PA(KP,1,LP))
377. 0306428 IF(J.EQ.MLM) PRF(K)=PR
378. 0306478 PN=(P(K,I-1,J)+P(K,I,J+1)+PR*P(K,I,J-1))/4.
379. 0306558 P(K,I,J)=P(K,I,J)+AL*(PN-P(K,I,J))
380. 0306648 E60 CONTINUE
381. 0306678 GC TO 870
C FOR 1ND LAST ROW MG, LAST BLOCK
382. 0306678 865 CONTINUE
383. 0306708 IF(IGK.EQ.1) GO TC 870
384. 0306718 DO 869 J=2,PLM
385. 0306748 PN=(P(K,I-1,J)+P(K,I,J+1)+P(K,I+1,J)+P(K,I,J-1))/4.
386. 0306738 P(K,I,J)=P(K,I,J)+AL*(PN-P(K,I,J))
387. 0306718 869 CONTINUE
388. 0306728 PRP(K)=P(K,I+1,MLM)
389. 0306758 870 CCNTINUE
C
C FOR AG
390. 0306718 YR=Y(K,N) $ MA1=MA(K,NM1)-1 $ JL=1
393. 0306758 IF(IGK.EQ.1) JL=2
394. 0306718 DO 920 J=JL,MA1
395. 0306738 YP=(J-1)*DZA+BVP $ YL=Y(K,N-2)
397. 0306718 IF(YL.LT.VP.CR.YR.LT.VP) GO TO 920
398. 0306758 IF (K.EQ.KB) GC TC 895
399. 0306748 IF(YP.GT.BVP-1.E-8) GC TO 885

```

```

C FOR MG IN NEXT BLOCK
400. 030752B LP=YP/DP*1 $ PRC=(YP-(LP-1)*EP)/DP
402. 030760B PR=P(KP,1,LP)*(1-PRC)+PFO*P(KP,1,LP+1)
403. 030766B GC TO 900

C FOR AG IN NEXT BLOCK
404. 030766B 855 CCNTINUE
405. 030770B YD=YP-BVP $ LP=YD/CPA*1 $ T1=YD-(LP-1)*DPA $ T2=DPA
409. 031000B IF(LP+1.EQ.MA(KP,1)) T2=DU(KF,1) $ FRC=T1/T2
411. 031006B PR=PA(KP,1,LP)+PRO*(PA(KP,1,LP+1)-PA(KP,1,LP))
412. 031014B GC TO 900
413. 031015B 855 PR=PA(K,N,J)
414. 031020B 900 CCNTINUE
415. 031022B IF(J.EQ.1) GO TO 510
416. 031023B IF(J.EQ.MA) GO TO 915
417. 031025B PN=(PA(K,NM2,J)+PA(K,NM1,J+1)+PR*PA(K,NM1,J-1))/4.
418. 031036B EN=(PN-PA(K,NM1,J))/PN
419. 031043B PA(K,NM1,J)=PA(K,NM1,J)+AL*(PN-PA(K,NM1,J))
420. 031050B IF(ABS(EN).GT.ERR) NEC=NEC+1
421. 031055B GC TO 920

C FOR FIRST COLUMN
422. 031055B 910 CCNTINUE
423. 031056B NM1=NMG-1
424. 031057B PD=P(K,NM1,MLN)+(1.-1./IGK)*(PRP(K)-P(K,NM1,PLN))
425. 031067B T1=DZ*DZA
426. 031072B PN=(PA(K,NM2,J)+PR)*DZ/(2.*T1)+(PA(K,NM1,J+1)+DZA/DZ+PD)*DZ*DZA/
    *(T1*T1)
427. 031114B PA(K,NM1,1)=PA(K,NM1,1)+AL*(PN-PA(K,NM1,1))
428. 031121B GO TO 920

C FOR 2ND LAST ROW, 2ND LAST COLUMN
429. 031121B 915 CCNTINUE
430. 031122B D2=DU(K,NM1)
431. 031124B T1=DZA*DZ
432. 031126B PN=D2*(PA(K,NM2,J)+PR)/(2.*T1)+DZA*(PA(K,NM1,J+1)+DZA*PA(K,NM1,J)
    +1)*DZ)/(T1*T1)
433. 031146B EE=PN-PA(K,NM1,PA1) $ EN=EE/PN
435. 031154B PA(K,NM1,MA1)=PA(K,NM1,MA1)+AL*EE
436. 031161B IF(ABS(EN).GT.ERR) NEC=NEC+1
437. 031166B 920 CCNTINUE
438. 031170B IF(IGK.EQ.1) GO TO 935

C
C FOR MG/AG INTERFACE
C
439. 031172B T1=DZA*DZ
440. 031174B DO 930 I=2,NM2
441. 031176B XA=(I-1)*DZA
442. 031200B XM=FIX(XA/DZ+1.E-8)+1 $ XM=(XM-1)*DZ $ PRO=(XA-XM)/DZ
445. 031207B IF(IM+1.EQ.NMG) P(K,IM+1,MLN)=PRP(K)
446. 031220B PD=P(K,IM,MLN)+PRC*(P(K,IM+1,MLN)-P(K,IM,MLM))
447. 031225B PN=(PA(K,I-1,1)+PA(K,I+1,1))*DZ/(2.*T1)+DZ*DZA/(T1*T1)*(PA(K,I,2)+
    *PD*DZA/DZ)
448. 031243B PA(K,I,1)=PA(K,I,1)+AL*(PN-PA(K,I,1))
449. 031247B 930 CCNTINUE

C EQUATE COMMON MG/AG PCTERTIALS
450. 031252B NSL=N-IGK
451. 031253B DO 933 I=1,NSL,IGK
452. 031256B IP=I/IGK+1
453. 031260B P(K,IM,NLL)=PA(K,I,1)
454. 031266B 933 CCNTINUE

```

CURDIS **PROGRAM CURDIS (INPUT, OUTPUT, PUNCH)** PAGE 9

```

455. 0312678 935 CONTINUE
      C
      C CALC POINTS ADJACENT TO A SURFACE WHERE NC NCDE OCCURS
      C
456. 0312708 LT=LL(K)
457. 0312718 IF(LT.EQ.0) GO TO 955
458. 0312728 IF(LT.LT.0) GO TO 3300
459. 0312748 DO 953 I=1,LT
460. 0312768 IF(LT.LT.0) GO TO 3300
461. 0313008 L=LQ
462. 0313018 I=IS(K,L) & J=JS(K,L) & DR=XR(K,L) & DA=XU(K,L) & DL=XL(K,L)
463. 0313138 T1=DA+DZA & T2=DR+DL & KP=K+1
464. 0313218 MAA=MA(K,I) & PO=PA(K,T,MAA)
465. 0313278 IF((K.EQ.1).AND.(I.EQ.1)) GO TO 939
466. 0313358 IF((K.EQ.NB).AND.(I.EQ.A)) GO TO 940
467. 0313438 IF(I.EQ.1) GO TO 941
468. 0313458 IF(I.EQ.NM1) GO TO 945
469. 0313478 JL=MA(K,I-1) & JR=MA(K,I+1)
470. 0313548 IF(DR.LT.DZA) GO TO 936
471. 0313578 P3=PA(K,I+1,J)
472. 0313628 GO TO 937
473. 0313648 936 P3=PO+DR/DZA*(PA(K,I+1,JR)-PO)
474. 0313738 937 CONTINUE
475. 0313748 IF(DL.LT.DZA) GO TO 938
476. 0313768 P1=PA(K,I-1,J)
477. 0314018 GO TO 951
478. 0314038 938 P1=PO+DL/DZA*(PA(K,I-1,JL)-PO)
479. 0314128 GO TO 951
480. 0314128 939 CONTINUE
481. 0314148 JR=MA(K,2) & P1=PO+DR/DZA*(PA(K,2,JR)-PO) & P3=P1
482. 0314248 GO TO 951
483. 0314248 940 CONTINUE
484. 0314268 JL=MA(K,NM1) & P1=PO+DL/DZA*(PA(K,NM1,JL)-PO) & P3=P1
485. 0314408 GO TO 951
      C I=1, K NE 1
486. 0314408 941 CONTINUE
487. 0314418 KM=K-1 & NKM=NR(KM)-1
488. 0314438 DZN=DZA(KM) & BVN=BV(KM) & VL=Y(KM,NKM) & VY=Y(K,1)
489. 0314538 IF(DL.LT.DZN) GO TO 942
      C LH
490. 0314568 PT NOT ON BORDER
491. 0314658 YAN=VY-BVN & JU=IF IX(YAN/DZN)+28 JL=MA(KM,NKM)
492. 0314718 IF(JU.GE.JL) JU=JL
493. 0314718 JD=JU-1 & YD=(JD-1)*DZN+BVN & YU=YD+DZN
494. 0314758 IF(JU.EQ.JL) YU=YL
495. 0315018 PRC=(YU-YD)/(YU-YD)
496. 0315048 P1=PA(KM,NKM,JD)+PRC*(PA(KM,NKM,JU)-PA(KM,NKM,JD))
497. 0315148 GO TO 943
      C FOR P1 ON BOUND
498. 0315148 942 CONTINUE
499. 0315168 P1=PO+DL/DZN*(PA(KM,NKM,JL)-PC)
500. 0315258 943 CONTINUE
      C FOR P3
501. 0315268 IF(DR.LT.DZA) GO TO 944
502. 0315308 P3=PA(K,2,J)
503. 0315338 GO TO 951
504. 0315338 944 CONTINUE
      C FOR P3 ON BORDER
505. 0315348 JR=MA(K,2)

```

CURDIS

PROGRAM CURDIS(INPUT,CLTPT,PLNCH)

P=JL 10

```

525. 0315358 P3=PO+DR/DZA*(PA(K,2,JR)-P0)
526. 0315448 GC TC 951
      C I=NM1
527. 0315448 945 CCNTINUE
528. 0315458 JR=MA(KP,1) & JL=MA(K,I-1)
530. 0315518 IF(DR.LT.DZA) GO TC 946
531. 0315548 IF(K.EQ.KB) GC TC 948
      C FOR P3 NOT ON BCRDER
532. 0315558 YK=Y(KP,1) & BVN=BV(KP) & YY=Y(K,I) & YAN=YY-BVN & DZN=DZA(KP)
537. 0315668 IF(K.EQ.KB) JR=PA(K,I+1)
538. 0315748 JU=IFIX(YAN/DZN)+2
539. 0315768 IF(JU.GE.JR) JU=JR
540. 0316038 JU=JU-1 & YD=(JD-1)*DZN+BVN & YU=YD+DZN
543. 0316108 IF(JU.EQ.JK) YL=YR
544. 0316148 PRC=(YY-YD)/(YU-YD)
545. 0316178 P3=PA(KP,1,JU)+PRC*(PA(KP,1,JU)-PA(KP,1,JD))
546. 0316268 GO TO 949
547. 0316268 946 CCNTINUE
548. 0316278 IF(K.EQ.KB) GC TC 947
549. 0316308 P3=PO+DR/DZA*(PA(KP,1,JK)-P0)
550. 0316378 GC TC 949
551. 0316408 947 JK=MA(K,I+1) & P3=PO+DR/DZA*(PA(K,I+1,JK)-P0)
553. 0316528 GC TC 949
554. 0316538 948 P3=PA(K,I+1,J)
      C FOR P1
555. 0316578 949 CCNTINUE
556. 0316618 IF(DL.LT.DZA) GC TC 950
557. 0316638 P1=PA(K,I-1,J)
558. 0316668 GC TC 951
559. 0316668 950 CONTINUE
560. 0316708 JL=MA(K,I-1) & GO TO 938
562. 0316728 951 CCNTINUE
563. 0316748 PN=(T1*(P1/DL+P3/DR)+T2*(PA(K,I,J+1)/DA+
      *PA(K,I,J-1)/DZA))/ (T1*(1/DL+1/DR)+ T2*(1/DA+1/DZA))
564. 0317218 EN=(PN-PA(K,I,J))/PN
565. 0317268 IF(K.NE.KC) GC TC 952
566. 0317308 E(I,J)=EN
567. 0317348 952 CCNTINUE
568. 0317358 IF(ABS(EN).GT.ERR) NEC=NEC+1
569. 0317428 PA(K,I,J)=PA(K,I,J)+AL*(PN-PA(K,I,J))
570. 0317508 953 CCNTINUE
571. 0317528 955 CONTINUE
      C
      C FOR LAST ROW LAST BLOCK
      C
572. 0317558 N=NR(KB) & NM1=N-1 & IGR=IGR(KB) & NMG=N/IGR+1 & NMN=NMG-1
577. 0317648 MLN=ML(KB)-1 & DZ=DX(KB) & DZA=DXA(KB) & BVV=BV(KB)
581. 0317728 IF(IGR(KB).EQ.1) GO TO 970
      C FOR MG
582. 0317748 DO 960 J=2,MLN
583. 0317778 PN=(2.*P(KB,NMN,J)+P(KB,NMG,J+1)+P(KB,NMG,J-1))/4.
584. 0320078 EN=(PN-P(KB,NMG,J))/PN
585. 0320138 IF(ABS(EN).GT.ERR) NEC=NEC+1
586. 0320218 P(KB,NMG,J)=P(KB,NMG,J)+AL*(PN-P(KB,NMG,J))
587. 0320258 960 CCNTINUE
      C FOR AG
588. 0320308 970 CCNTINUE
589. 0320318 MAA=MA(KB,N) & MA1=MAA-1 & MA2=MAA-2 & YL=Y(KB,N-1)

```

```

593. 032C378 DO 980 J=2,MA2
594. 0320428 YP=(J-1)*DZA+BYV
595. 032C458 IF(YL.LT.YPI) GC TC 980
596. 03205C8 PN=(2.*PA(KB,NM1,J)+PA(KB,N,J+1)+PA(KB,N,J-1))/4.
597. 0320608 EN=(PN-PA(KB,N,J))/PN
598. 0320648 IF(ABS(EN).GT.ERR) NEC=NEC+1
599. 0320718 PA(KB,N,J)=PA(KB,N,J)+AL*(PN-PA(KB,N,J))
600. 032C758 980 CONTINUE
      C FOR PA(KB,N,MA1)
601. 0321008 YP=(MA1-1)*DZA+BYV
602. 0321048 IF(YP.GT.YL) GC TO 990
603. 0321068 D2=DUI(KB,N) * T1=D2*DZA
605. 0321128 PN=D2*PA(KB,NM1,MA1)/T1+DZA*(PA(KB,N,MAA)*DZA+PA(KB,N,MA2)*D2)/
      *(T1+T1)
606. 0321318 EE=PN-PA(KB,N,MA1)
607. 0321368 PA(KB,N,MA1)=PA(KB,N,MA1)+AL*EE
608. 0321438 EN=EE/PN * IF(ABS(EN).GT.ERR) NEC=NEC+1
610. 0321518 990 CONTINUE
611. 0321518 IF(IGR(KB).EQ.1) GC TO 1000
612. 0321538 T1=D2*DZA
      C FOR PA(KB,N,1)
613. 0321558 PN=DZ/T1*PA(KB,NM1,1)+ DZ*DZA/T1/T1*(PA(KB,N,2)+PA(KB,NMG,MLM)*DZA
      */DZ)
614. 0321748 PA(KB,N,1)=PA(KB,N,1)+AL*(PN-PA(KB,N,1))
615. 0322C08 P(KB,NMG,MLL)=PA(KB,N,1)
616. 0322C58 1000 CONTINUE
617. 0322068 EAV=ET/IE
618. 0322C78 IF(MOD(LIT,NIPC).NE.0) GC TC 1070
619. 0322148 PRINT 320C,TIM,ITS
620. 0322228 CALL PMAP
621. 0322248 N=NR(KC)
622. 0322258 IF(KC.NE.KB) N=N-1
623. 0322318 DO 1065 I=1,N
624. 0322338 MAA=MA(KC,I)
625. 0322358 DO 1065 J=1,MAA
626. 0322408 IF(ABS(E(I,J)).GT.ERR) PRINT 1064,I,J,E(I,J)
627. 0322568 1064 FORMAT(* I,J,E*215,1PE10.2)
628. 0322568 1065 CONTINUE
629. 0322638 1070 CONTINUE
630. 0322638 IF(LIT.GT.ILM) GC TC 1080
631. 0322658 IF(NEC.EQ.0) GO TO 1080
632. 0322668 IF(B.EQ.0.AND.CPC.EQ.0) GC TO 300
      C CALC CD FOR TAFEL, AFTER LCCSE CCNV
633. 0322718 VCC=1.E-4*(ERR/1.E-3)**(1000*ERR/RBM)
634. 0322778 IF(RBM.LT.10*TER) VCC=.01*ERR
635. 0323058 IF(EAV.GT.VCC) GO TO 300
636. 0323078 IF(ITP.GT.9*1000.*ERR/RBM+1) GO TO 1080
637. 0323148 GO TO 300
638. 0323148 1080 CONTINUE
639. 0323158 ITP=0 * ITC=ITC+1
641. 0323168 CALL CURCAL
642. 0323218 IF(MOD((ITC-1),20).EQ.0) PRINT 3175
643. 0323318 IF(IPRT.EQ.1) GC TC 9030
644. 0323328 IPRT=1
645. 0323338 GO TO 300
646. 0323338 9000 CONTINUE
      C DETERMINE FACTORS FOR WEIGHTING
647. 0323358 IF(CPC.EQ.0.AND.B.EQ.0) GO TO 3155

```

CURDIS

PROGRAM CURDIS(INPUT,OUTPUT,PUNCH)

P. 12

```

648. 0323378 IF(ACE.GT..2)GC TO 300
649. 0323418 PTC=PT(KC,IC)
650. 0323438 CALL CONFAC
651. 0323468 CCC=10*ERR
652. 0323478 IF(CPC.EQ.0) GC TO 3142
653. 0323518 IF(FLC.EQ.0) GC TO 3135
C FIND COORDINATES OF MAX CURRENT POINT
654. 0323528 CDMAX=CD(1,1)
655. 0323528 DO 3130 K=1,K8
656. 0323558 NM1=NR(K)-1
657. 0323568 DO 3130 I=1,NM1
658. 0323618 IF(CD(K,I+1).LT.CDMAX) GC TO 3130
659. 0323668 CDMAX=CD(K,I+1)
660. 0323708 3130 CONTINUE
661. 0323768 3135 CCATIAUE
662. 0323768 DO 3141 K=1,K8
663. 0324008 N=NR(K)
C CONCENTRATION OVERPOTENTIAL
664. 0324008 DO 3141 I=1,N
665. 0324048 CL=CLC/OLD(K,I)
666. 0324068 IF(FLC.NE.C) CL=CDMAX/FLC
667. 0324138 TLC=CD(K,I)/CL
668. 0324148 IF(TLC.GT.1) TLC=.999
669. 0324208 COV(K,I)=-CPC*ALOG(1-TLC)
670. 0324258 3141 CCNTINUE
671. 0324348 3142 CCNTINUE
672. 0324348 BPE=0.
673. 0324348 CBE=0
674. 0324358 RBM=0
675. 0324358 L=C
676. 0324368 DO 3150 K=1,K8
677. 0324418 NM1=NR(K)-1
678. 0324428 IF(K.EQ.K8) NM1=NR(K)
679. 0324458 DO 3150 I=1,NM1
680. 0324478 CDD=ABS(CD(K,I)) * IF(CDD.LT.CDD) CDD=1.01*CDD
681. 0324578 L=L+1
682. 0324608 J=PA(K,I)
683. 0324618 IF(CDD.EQ.0) GETC 3145
C TAFEL POLARIZATION
685. 0324628 PN=VC+B*ALOG(CDD/CDD)+CCV(K,I)
686. 0324718 BPE=ABS((PN-PA(K,I,J))/PN)
687. 0324778 IF(BPE.GT.RBM) RBM=BPE
688. 0325038 IF(PN.GT.VA) PA=VA
689. 0325068 PA(K,I,J)=PA(K,I,J)+FP*(PN-PA(K,I,J))
690. 0325138 CBE=BPE+CBE
691. 0325148 GO TO 3150
692. 0325148 3145 CONTINUE
C LINEAR POLARIZATION
693. 0325168 PN=VC+A+B*CD(K,I)+CCV(K,I)
694. 0325238 BPE=ABS((PN-PA(K,I,J))/PN)
695. 0325318 IF(PN.GT.VA) PN=VA
696. 0325348 PA(K,I,J)=PA(K,I,J)+FP*(PN-PA(K,I,J))
697. 0325418 3150 CONTINUE
698. 0325478 RBE=CBE/L
699. 0325508 3155 CONTINUE
700. 0325528 IF(ILLT.GT.ILLM) GO TO 3185
C STORE BOUNDARY POTENTIALS
701. 0325548 DO 3156 K=1,K8

```

```

CURDIS      **PROGRAM CURDIS (INPUT, OUTPUT, PUNCH)**

702. 0325568 NMI=NR(K)-1
703. 0325578 IF (K.EQ.KB) NMI=NR(K)
704. 0325628 DO 3156 I=1,NMI
705. 0325648 J=MA(K,I)
706. 0325668 PT(K,I)=PA(K,I,J)
707. 0325718 3156 CONTINUE
708. 0325748 IF (B.EQ.O. AND CPC.EQ.O) GO TO 3158

C FOR TAFEL POLARIZATION
709. 0325778 IF (CDO.EQ.O) GO TO 3157
710. 0326008 CLM=CLC/(DLD(KC,IC)+1.E-30)
711. 0326048 WC=CPC/(CLM-CD(KC,IC))*CCN/Y(KC,TC)
712. 0326118 IF (FLC.NE.O) WC=CCN/Y(KC,IC)*CPC/(CDMAX/FLC-COMAX)
713. 0326238 WCT=CCN*B/Y(KC,IC)*CD(KC,IC)
714. 0326308 WN=WC+WCT
715. 0326318 WF=1/(1+WN)
716. 0326338 3157 CONTINUE
717. 0326348 IF (NEC.NE.O) GO TO 3165
718. 0326358 IF (RBN.GT.1000.*ERR) GO TO 3165
719. 0326378 IF (ACE.GT.CCT) GO TO 3165
720. 0326378 3158 CONTINUE
721. 0326428 IF (IPOT.NE.O) CALL PMAP

C DETERMINE TIME STEPS
722. 0326458 CALL CURBAL(CCT,CAT,AVI)
723. 0326478 IF (CCOUL.EQ.O.) CCOUL=CCT*DT & DT=CCOUL/CCT
725. 0326548 CCS=CCT*DT & CAS=CAT*DT & TCC=CCS*YCC & TCA=CAS+TCA

C CALC TOT COULOMBS
729. 0326628 PRINT 3159,CCT,CAT,CCS,CAS,TCC,TCA
730. 0326748 3159 FORMAT(/% CATHODE CURRENT*1PE15.5% ANODE CURRENT*1PE15.5% CATH
+COUL 1 TS*1PE15.5% ANODE COUL 1 TS*1PE15.5% TOTCATH COUL*1PE15.
+5% TCT ANODE COUL*1PE15.5/)
731. 0326748 PRINT 3160,AVI
732. 0327008 3160 FORMAT(/% AVG CURRENT*1PE15.5)
C FOR K=1, I=1 AND K=KB, AND I=N
C PRINT CONVERGENCE STATUS
733. 0327008 PRINT 3169,EAV,LIT,NEC,ITC
734. 0327078 3169 FORMAT(/% AVERAGE ERROR PER NODE*1PE10.3% ITERATIONS*15% UNCON
+VERGED POINTS*15% ITERATIONS IN CURRENT LOOP*15)

C CALC NEW POSITION OF BOUNDARY
735. 0327078 DO 3161 K=1,KB
736. 0327118 DZA=DZA(K)
737. 0327118 NMI=NR(K)-1
738. 0327138 IF (K.EQ.KB) NMI=NMI+1
739. 0327208 DO 3161 I=1,NMI
740. 0327228 DD=D(K,I) & PHI=ATAN(CD) & APHI=ABS(PHI) & CSA=COS(APHI)
744. 0327348 T=DF*CD(K,I)*DT
745. 0327378 XN(K,I)=(I-1)*DZA+T*SIN(PHI)
746. 0327458 YN(K,I)=Y(K,I)-T*CSA
747. 0327518 3161 CONTINUE
748. 0327578 IF (KB.EQ.1) GO TO 3163

C EQUATE COORDINATES OF LAST ROW TO FIRST ROW OF PREVIOUS BLOCK
749. 0327608 KBM=KB-1
750. 0327618 DO 3162 K=1,KBM
751. 0327638 KP=K+1 & N=NR(K)
753. 0327658 XN(K,N)=XN(KP,1)+(N-1)*DZA(K) & YN(K,N)=YN(KP,1)
755. 0327748 3162 CONTINUE
756. 0327758 3163 CONTINUE
757. 0327768 CALL SMOOTH
758. 0330008 Y(1,1)=YN(1,1) & Y(KB,N)=YN(KB,N)

```


CURDIS		**PROGRAM CURDIS(INPUT,OUTPUT,PUNCH)**	PAGE 14
760.	0330048	CALL DEP	
761.	0330068	CALL SETUP	
762.	0330108	CALL SPLN	
763.	0330128	3165 CCNTINUE	
764.	0330128	C RESET CATHODE POTENTIAL	
765.	0330148	DO 3166 K=1,K8	
766.	0330158	NMI=NR(K)-1	
767.	0330208	DO 3166 I=2,NMI	
768.	0330228	MAA=MA(K,I)	
		DC 3166 J=1,MAA	
769.	0330268	C FOR ANODIC DISSOLUTION	
770.	0330378	IF(PA(K,I,J).LT.-56) PA(K,I,J)=PT(K,I)	
771.	0330468	3166 CCNTINUE	
772.	0330478	DO 3167 K=1,K8	
773.	0330508	NMI=NR(K)-1	
774.	0330538	IF(K.EQ.K8) NMI=NR(K)	
775.	0330558	DO 3167 I=1,NMI	
776.	0330578	J=MA(K,I)	
777.	0330678	IF(PT(K,I).GT.VAI PT(K,I)=.5*VA+.1*VC	
778.	0330728	PA(K,I,J)=PT(K,I)	
779.	0331008	3167 CCNTINUE	
		PRINT 3168,LI,T,EAV,CFM,CF,WF,CIF,FP,RBE,CD(KC,IC),PT(KC,IC),CD(1,1	
		S),PT(1,1),ACE	
780.	0331268	3168 FORMAT(15,12(1PE10.3))	
781.	0331268	DO 3173 K=1,K8	
782.	0331308	IF(MOD(LITC,20).NE.0) GO TO 3181	
783.	0331348	PRINT 317C,K	
784.	0331418	3170 FORMAT(* K=15)	
785.	0331418	N=NR(K)	
786.	0331428	PRINT 3171,(CD(K,I),I=1,N)	
787.	0331568	3171 FORMAT(10T1PE11.4)	
788.	0331568	3173 CCNTINUE	
789.	0331608	PRINT 3174,CMI,CMA,MC,WCT,MN,RBM*6(1PE12.3)	
790.	0331728	3174 FORMAT(* ,CMI,CMA,MC,WCT,MN,RBM*6(1PE12.3))	
791.	0331728	3175 FORMAT(7* ITER AVERAGE CONSIST CURRENT WAGNER CURR B.T	
		\$ DAMPING BOUNDARY CD(KC,IC) BOUNDARY CU(1,1) BOUNDARY AVERA	
		\$GE\$ 7* POTENTIAL FACTOR ERROR FACTOR MULT	
		\$ FACTOR ERROR PCTENTIAL PCTENTIAL CURRE	
		SNT\$ 7* ERROR	
		\$ (KC,IC)	
		1,1) ENR	
		\$OR\$)	
792.	0331728	3181 CONTINUE	
793.	0331728	IF(B.EQ.0.AND.CPC.EQ.0) GO TO 3185	
794.	0331748	IF(RBM.GT.1000*ERR) GC TO 300	
795.	0331768	IF(NEC.EQ.0.AND.ACE.LT.CCC) GO TO 3185	
796.	0332028	GC TO 300	
797.	0332028	3185 CONTINUE	
798.	0332038	ITS=ITS+1	
799.	0332048	TIM=TIM+DT	
800.	0332058	PRINT 3200,TIM,ITS	
801.	0332138	3200 FORMAT (7/5X, *TIME=*1PE15.5* SEC TIME STEP=*15)	
802.	0332138	IF(IPI.EQ.0) GC TO 3206	
803.	0332148	PUNCH 3202,ITS,TIM,TCC	
804.	0332228	IF(ITS.EQ.ITM) PUNCH 3202,ITS,TIM,TCC	
805.	0332328	3202 FORMAT(15,2E15.5)	
806.	0332328	DO 3204 K=1,K8	
807.	0332348	NMI=NR(K)-1 \$ IF(K.EQ.K8) NMI=NMI+1	
809.	0332418	PUNCH 238,(V(K,I),I= 1,NMI)	

CURDIS

PROGRAM CURDIS (INPUT,CUTPUT,PUNCH)

PAGE 15

```

810. 033254B 3204 CONTINUE
811. 033256B 3206 CONTINUE
812. C33257B (ALL CURMAP
813. C33261B PRINT 3250,CL,CCV(KC,IC)
814. 033271B 3250 FORMAT(* LIM CUR*1PE15.5* CONC OVERPOTENTIAL*1PE15.5)
815. C33271B IF(LIT.GT.ILM) PRINT 3251,EAV
816. 033300B 3251 FORMAT(* NO CONV, AV ERROR *1PE10.2)
817. 033300B IF(LIT.GT.ILM) GO TO 3300
818. C33302B IF(LTS.LT.IT#) GO TO 298
819. 033302B 3300 CONTINUE
820. C33305B END

```

CCNFAC

SUBROUTINE CONFAC

PAGE 1

```

1. 000000B SUBROUTINE CONFAC
2. 000000B COMMON/CCNF/ERR,TER,PTC,RBE,RBM,WF,LIT,ILM,ITC,CZ,DCZ,CFM,CIF,
SCF,CMI,CMA,FP
3. 000000B COMMON/CURCOM/DYV(1,101),DYV(1,101),ACE
4. 000000B DC=PTC-CZ
5. 000001B DCF=DC*DCZ & CFM=1.10*CFM & IF(CFM.GT.1,ICFM=1.
8. 000010B IF(DCF.LT.0) CFM=.6*CFM+ERR
9. 000015B CF=1/(1+.5*CFM*ACE)+100*ERR
10. 000021B IF(RBE.LT.100.*ERR) CIF=.8*CIF
11. 000025B IF(RBM.LT.1000.*ERR) CIF=.6*CIF+ERR
12. 000032B IF(LIT.GT..8*ILM) CIF=.75*CIF+1.E-4
13. 000041B IF(CIF.GT.1/TER) CIF=1/TER
14. 000046B CMI=.007*WF*(1+.5*CFM)
15. 000052B CMA=.012*WF*(1+.5*CFM)
16. 000057B T1=.001*(1+.2000*RBE/(1.E4*ERR+RBE))
17. 000065B CMI=T1*CMI & CMA=T1*CMA
18. 000070B IF(ACE.LT.CMI) CIF=1.2*CIF & IF(ACE.GT.CMA) CIF=.5*CIF+ERR
21. 000102B FP=CF*CFM*WF*CIF+1.E-4
22. 000106B IF(FP.GT.WF) FP=WF+1.E-4
23. 000112B CZ=PTC
24. 000112B DCZ=DC
25. 000114B RETURN & END

```

CURBAL

SUBROUTINE CURBAL(CCT,CAT,AVI)

PAGE 1

```

1. 0000002 SUBROUTINE CURBAL(CCT,CAT,AVI)
2. 0000008 C CALCULATE THE TOTAL ANODE AND CATHODE CURRENTS
3. 0000008 COMMON/BLDAT/BVI(6),DX(6),DXA(6),IGR(6),KB,PL(6),NAS(6),NR(6)
4. 0000008 COMMON/CIRCDN/CC(1,101)
5. 0000008 COMMON/DXIV/D(1,101)
6. 0000008 COMMON/POL/A,B,CDC,CUN,VA,VC
7. 0000008 COMMON/YOIS/Y(1,101),MA(1,101)
8. 0000008 COMMON P1, S1, S11, PA(1,101,101),PT(1,101)
11. 0000018 CCT=0. $ CAT=0. $ AT=0.
12. 0000048 DO 50 K=1,KB
N=NR(K) $ NM1=N-1 $ DZA=DXA(K) $ IGR IGR(K)
C CATHODE INTERIOR
16. 0000108 DO 10 I=2,NP1
17. 0000148 AR=DZA/COS(ATAN(C(K,I))) $ CC=CD(K,I)*AR $ AT=AT+ABS(AR)
20. 0000318 CCT=CCT+ABS(CCT)
21. 0000338 10 CONTINUE
C CATHODE 1ST AND LAST
22. 0000368 AAL=.5*AR $ AR=DZA/CCS(ATAN(D(K,1))) $ CCL=.5*CD(K,1)*AR
25. 0000518 CCL=.5*CC
26. 0000528 CCL=CCT+ABS(CCL)+ABS(CCL)
27. 0000608 AT=AT+ABS(AAL)+ABS(AR) $ AVI=CCT/AT
C ANODE
29. 0000678 NM1=N/IGK
30. 0000728 IF(IGK.EQ.1) NM1=N-1
31. 0000768 DO 30 I=2,NP1
32. 0001008 IF(IGK.EQ.1) GO TO 20
33. 0001028 PM1=P(K,I,2) $ PM2=P(K,I,3)
35. 0001078 GO TO 25
36. 0001108 20 PM1=PA(K,I,2) $ PM2=PA(K,I,3)
38. 0001158 25 CONTINUE
39. 0001168 CA=CON*(PM2/2-2*PM1+1.5*VA)
40. 0001238 CAT=CAT+ABS(CA)
41. 0001258 30 CONTINUE
42. 0001308 IF(IGK.EQ.1) GO TO 35
43. 0001328 CAL=.5*CON*(P(K,1,3)/2-2*P(K,1,2)+1.5*VA)
44. 0001418 GO TO 40
45. 0001428 35 CAL=.5*CON*(PA(K,1,3)/2-2*PA(K,1,2)+1.5*VA)
46. 0001528 40 CONTINUE
47. 0001538 CAL=.5*CA
48. 0001548 CAT=CAT+ABS(CAL)+ABS(CAL)
49. 0001618 50 CONTINUE
50. 0001648 RETURN
51. 0001668 END

```

CURCAL

SUBROUTINE CURCAL

PAGE 1

```

1. 0000008 SUBROUTINE CURCAL
2. 0000008 CCMCN/BLDAT/8Y(6),DX(6),DZA(6),IGR(6),KB,ML(6),NAS(6),NR(6)
3. 0000008 CCMCN/CURCOM/D>V(1,101),D>V(1,101),ACE
4. 0000008 CCMCN/CURDEN/CC(1,101)
5. 0000008 CCMCN/DRIV/D(1,101)
6. 0000008 CCMCN/PCL/A,B,(CO,CUN,VA,VC
7. 0000008 CCMCN/UPDIS/DU(1,101)
8. 0000008 CCMCN/YDIS/Y(1,101),MA(1,101)
9. 0000008 CCMCN/P(1,51,51),PA(1,101,101),PT(1,101)
10. 0000008 M=C $ CET=0
12. 0000018 DC 3120 K-1,KB
13. 0000038 N=NR(K) $ NM1=N-1 $ DZA=DZA(K) $ NM2=N-2
C CALCULATE ALL Y-COMPONENTS
17. 0000108 NM=N-1
18. 0000118 IF(K.EQ.KB)NM=NM+1
19. 0000168 DC 3120 I=1,NM
20. 0000208 J=MA(K,I)
21. 0000228 PD=PA(K,I,J-1) $ P1=PA(K,I,J-2) $ P2=PA(K,I,J)
24. 0000348 YV=Y(K,I) $ DV=D(K,I) $ PD=DU(K,I)
C FIND Y-DISTANCE VARIABLES FOR Y-COMPONENTS
27. 0000408 FC=(PD+DZA)/DZA
28. 0000428 T1=1+FD
29. 0000448 PIX=(FD*(PD-P2)/T1-T1*(P1-P2)/FD)/DZA
30. 0000538 FC=PD/DZA
31. 0000558 PC=PA(K,I,J-2) $ P1=PA(K,I,J-1) $ P2=PA(K,I,J)
34. 0000728 T1=1+FD
35. 0000748 P2X=(FD*(PD-P2)/T1-T1*(P1-P2)/FD)/DZA
C IGNORE 2ND LAST COLUMN IF IGC CALCSE TO SURFACE NODE
36. 0001038 D>V=P2X $ IF(FD.LT..2) D>V=PIX
C COMPUTE X-DERIVATIVE
38. 0001128 IF(ABS(DR).GT.1.E-2) GO TO 2C20
C FOR FLAT SURFACE
39. 0001148 DVX=0.
40. 0001158 GC TO 3100
41. 0001158 2020 CONTINUE
C CHECK DIRECTION OF ASCENT
42. 0001168 KP=K-1 $ KP=K+1
44. 0001178 IF(DR.LT.0) GO TO 2030
C FOR +DR
45. 0001228 I1=I+1 $ I2=I+2
47. 0001248 GO TO 2040
48. 0001248 2C30 CONTINUE
49. 0001268 I1=I-1 $ I2=I-2
51. 0001308 2040 CONTINUE
52. 0001318 IF((I2.LT.N).AND.(I2.GT.0)) GO TO 3010
C FOR 2ND ROW 1ST RL, 2ND LAST ROW LAST RL
53. 0001348 IF((K.EQ.1).AND.(I.EQ.2)) GO TO 2050
54. 0001438 IF((K.EQ.KB).AND.(I.EQ.NM1)) GO TO 2050
55. 0001518 IF((K.EQ.KB).AND.(I.EQ.NM2)) GO TO 3010
56. 0001608 GO TO 2060
C USE IMAGE POINTS FOR 2ND OR IND LAST ROWS, DERIVATIVE LT 0, GT 0 RESP
57. 0001618 2C50 I2=1
58. 0001618 GC TO 3010
59. 0001618 2060 CONTINUE
C 1ST ROW OR LT 0
60. 0001638 IF(I.NE.1) GO TO 2070
61. 0001648 KP=KM $ I1=NR(KK)-1 $ I2=I1-1

```

CURCAL	**SUBROUTINE CURCAL**	PAGE 2
64.	00C1708 GC TO 3020	
65.	0001708 2070 CONTINUE	
	C 2ND ROW, DR LT 0, CR 2ND LAST OF GT 0	
66.	00C1728 KK=KP & IF(I.EQ.2)KK=KN	
68.	00C1778 DZN=DZA(KK) & BVN=BV(KK) & YAN=YY-BVN & T=YAN/DZN	
72.	00C2048 JL=IFIX(I)+1 & INB=NR(KK)-1	
74.	00C2108 IF(I.EQ.NM1) INB=2	
75.	00C2148 IF(I.EQ.NM2) INB=1	
76.	00C2178 MA1=MA(KK,INB)-1	
77.	00C2218 IF(YY.GT.Y(KK,INB)) GO TO 3055	
78.	00C2268 JH=JL+1	
79.	00C2278 YLN=(JL-1)*DZN & PDN=YAN-YLN	
81.	00C2358 TD= DZN*DU(KK,INB)	
82.	00C2368 IF(JH.NE.(MA1+1)) TD=2.*DZN	
83.	00C2418 YPX=DZN*PDN	
84.	00C2428 PX2= PDN*(YPX-TD)*PA(KK,INB,JL-1)/(DZN*TD)+ YPX*(YPX-TD)* * PA(KK,INB,JL)/(DZN*(DZN-TD))+ YPX*(YPX-DZN)*PA(KK,INB,JH)/ * (TD*(TD-DZN))	
85.	00C2718 L=3 & KK=KP & IF(I.EQ.2.CR.I.EQ.NM2)KK=K	
	C GENERAL CASE FOR THE X-COMPONENT OF CURRENT	
88.	00C3018 GO TO 3030	
89.	00C3018 3010 KK=K	
90.	00C3028 DZN=DZA(KK)	
91.	00C3048 IF(I.EQ.1) GO TO 3020	
92.	00C3068 YLL=Y(K,I-1)+1.E-8 & YRR=Y(K,I+1)+1.E-8	
94.	00C3128 IF(YY.LT.YLL).OR.(YY.LT.YRR)) GO TO 3020	
	C FOR DEEP RECESS	
95.	00C3168 DVX=0.	
96.	00C3168 GO TO 3100	
97.	00C3208 3020 L=1	
98.	00C3208 DZN=DZA(KK)	
99.	00C3228 3030 IN=11	
100.	00C3238 IF(KK.EQ.K) GO TO 3040	
101.	00C3268 IF(I.EQ.NM1.AND.K.NE.K8) IN=1	
102.	00C3348 3040 CCNTINUE	
103.	00C3348 BVN=BV(KK) & YAN=YY-BVN & DZN=DZA(KK) & T=YAN/DZN	
107.	00C3418 JL=IFIX(I)+1 & MA1=MA(KK,IN)-1	
109.	00C3468 JH=JL+1	
110.	00C3478 IF(YY.GT.Y(KK,IN)) GO TO 3095	
111.	00C3548 YLN=(JL-1)*DZN & PDN=YAN-YLN	
113.	00C3608 TD= DZN*DU(KK,IN)	
114.	00C3638 IF(JH.NE.(MA1+1)) TD=2.*DZN	
115.	00C3668 YPX=DZN*PDN	
116.	00C3678 IF(DU(K,I)+1.E-4.GT.DZA) GO TO 3050	
117.	00C3738 IF(ABS(DR).GT..7) GO TO 3105	
118.	00C3738 3050 CONTINUE	
119.	00C3768 PX= PDN*(YPX-TD)*PA(KK,IN ,JL-1)/(DZN*TD)+ YPX*(YPX-TD)* * PA(KK,IN ,JL)/(DZN*(DZN-TD))+ YPX*(YPX-DZN)*PA(KK,IN ,JH)/ * (TD*(TD-DZN))	
120.	00C4258 IF(L.EQ. 2) GO TO 3070	
121.	00C4278 PX1=PX & IN=12	
123.	00C4328 IF(L.EQ.3) GO TO 3090	
124.	00C4348 L=2	
125.	00C4358 GO TO 3040	
126.	00C4358 3070 CONTINUE	
127.	00C4378 PX2=PX	
	C COMPUTE THE X-COMPONENT OF CURRENT	
128.	00C4378 DVX=(PX2/2.-2.*PX1+1.5*P2)/DZN	

CURCAL	**SUBROUTINE CURCAL**	PAGE 3
129.	0004458 IF(DVX,GT,0) DVX=(P2-PX1)/DZA	
130.	0004458 GC TO 3100	
131.	0004508 C FOR UNEQUAL SPACING	
132.	0004518 3090 CONTINUE	
133.	0004528 BT=DZA/DZN	
134.	0004548 T1=1.+BT	
135.	0004548 DVX=(BT*(PX2-P2)/T1-T1*(PX1-P2)/BT)/DZN	
136.	0004638 IF(DVX,GT,0) DVX=(P2-PX1)/DZA	
137.	0004678 GC TO 3100	
138.	0004708 3095 DVX=0.	
139.	0004708 GO TO 3100	
140.	0004728 3105 CONTINUE	
141.	0004728 MAA=MA(K,I) & MA1=MAA-1	
142.	0004748 IF(DU(KK,IN)+1.E-4,GT,DZA) GO TO 3107	
143.	0005028 IF(MA(KK,IN).EQ,MAA) GO TO 3050	
144.	0005028 3107 CONTINUE	
145.	0005078 IF(DR,GT,0) GO TO 3110	
146.	0005108 N1=1-1 & N2=1-2 & N3=1-3	
147.	0005138 GO TO 3112	
148.	0005138 3110 CONTINUE	
149.	0005158 N1=1+1 & N2=1+2 & N3=1+3	
150.	0005208 3112 CONTINUE	
151.	0005218 IF(N3,GT,NM1) GO TO 3050	
152.	0005238 IF(N1,LT,1) GC TO 3050	
153.	0005258 DXH=(PA(K,N3,MAA)/2-2*PA(K,N2,MAA)+1.5*PA(K,N1,MAA))/DZA	
154.	0005418 DXL=(PA(K,N2,MAA)/2-2*PA(K,N1,MAA)+1.5*PA(K,I,MAA))/DZA	
155.	0005558 PRO=DU(K,I)/DZA & DVX=(1-PRO)*DXL+PRO*DXH	
156.	0005628 3100 CONTINUE	
157.	0005648 M=M+1	
158.	0005658 DXV(K,I)=DVX & DYV(K,I)=DZY	
159.	0005678 3120 CONTINUE	
160.	0005678 C COMPLETE TOTAL CD	
161.	0005768 DO 3131 K=1,K8	
162.	0005778 NM1=NR(K)-1	
163.	0006008 IF(K.EQ,K8) NM1=NM1+1	
164.	0006048 DC 3131 I=1,NM1	
165.	0006068 UD=D(K,I) & AD=ABS(UD)	
166.	0006118 APHI=ATAN(AD) & CSA=COS(APHI)	
167.	0006178 DVX=DXV(K,I) & DZY=DYV(K,I)	
168.	0006228 CA=CON*(DZY*CSA+DVX*SIN(APHI))	
169.	0006318 IF(CN,GT,0) PRINT 3124,K,I,PI(K,I),CN	
170.	0006438 3124 FORMAT(* K,I,PI(K,I), CN*215,2(1PE15.5))	
171.	0006438 IF(CN,GT,0) CN=.9*CD(K,I) & CN=ABS(CN)	
172.	0006508 RCE=(CN-CD(K,I))/(CN+1.E-8) & REC=ABS(RCE)	
173.	0006558 CD(K,I)=CN	
174.	0006568 CET=CET+REC	
175.	0006578 3131 CONTINUE	
176.	0006658 ACE=CET/M	
177.	0006668 RETURN & END	

CURMAP

SLROUTINE CURMAP

PAGE 1

```

1. 0000008 SUBROUTINE CURMAP
2. 0000008 DIMENSION CCV(1,101)
3. 0000008 CCMPCN/BCFG/XN(1,101),YN(1,101)
4. 0000008 CCMPCN/BLCAT/BV(6),DX(6),CXA(6),IGR(6),KB,ML(6),NAS(6),NR(6)
5. 0000008 CCMON/CURCCN/DXV(1,101),DYV(1,101),ACE
6. 0000008 CCMCN/CCNC/CCV
7. 0000008 CCMCN/CURDEN/CD(1,101)
8. 0000008 CCMON/DRIV/D(1,101)
9. 0000008 CCMCN/YOIS/Y(1,101),PA(1,101)
10. 0000008 CCMON P(1, 51, 51),PA(1,101,101),PT(1,101)
11. 0000008 X=0.
12. 0000008 DO 3240 K=1,KB
13. 0000008 XB=X
14. 0000008 PRINT 3210, K,BV(K)
15. 0000148 3210 FORMAT(72X, *BLCCK*I3/2X, *BV=*F5.2)
16. 0000148 PRINT 3220
17. 0000178 3220 FORMAT(* RCW AG X-COORD Y-COORD NEW X NEW Y
$ DERIVATIVE CURRENT X-COMPONENT Y-COMPONENT BOUNDARY*/
$ * PTS (CM) (CM) COORDINATE COORDINATE
$ (A/CMSQ) POTENTIAL*)
18. 0000178 DZA=DXA(K)
19. 0000208 N=NR(K)
20. 0000218 DO 3240 I=1,N
21. 0000248 X=((-1)*DZA+XB
22. 0000278 PRINT 3230,I,MA(K,I),X,Y(K,I),XN(K,I),YN(K,I),D(K,I),CD(K,I),DXV(K
$,I),DYV(K,I),PT(K,I),COV(K,I)
23. 0000648 3230 FORMAT(215,9(1PE12.4),0PF6.3)
24. 0000648 3240 CONTINUE
25. 0000718 RETURN $ END

```

DEP	**SUBROUTINE DEF**	PAGE 1
1.	0000008 SUBROUTINE DEF	
2.	0000008 DIMENSION AL(101),AM(101),C(101),DN(1,101),DC(101)	
3.	0000008 COMMON/BLDAT/BV(6),DX(6),DXA(6),IGR(6),KB,ML(6),NAS(6),NR(6)	
4.	0000008 COMMON/YDIS/Y(1,101),PA(1,101)	
5.	0000008 COMMON/BCMG/XN(1,101),YN(1,101)	
6.	0000008 DO 110 K=1,KB	
7.	0007738 N=NR(K) \$ NM=N-1 \$ KM=K-1 \$ KP=K+1 \$ DZA=DXA(K)	
12.	0010008 IL=0 \$ IA=1 \$ IB=N	
15.	0010038 C FIND 1ST PT TO LEFT OF LHS OR USE Y(KM,NR(KM))	
16.	0010068 IF(XN(K,1).LE.0.) GO TO 10	
	NP=NR(KM)	
	C USE Y-PTS CALCD FROM PREVIOUS BLOCKS	
17.	0010078 HJ=DXA(KM) \$ HJP=XN(K,2)	
19.	0010138 AL(1)=HJP/(HJ+HJP) \$ AM(1)=1.-AL(1)	
21.	0010168 C(1)=3.*AL(1)*(Y(KM,NM)-Y(KM,NM-1))/HJ +3.*AM(1)*(YN(K,2)-YN(KM,NM))	
	*/HJP	
22.	0010328 GC TO 30	
23.	0010328 10 CCNTINUE	
24.	0010348 IF(K.EQ.1) GC TO 20	
	C WHEN 1ST PT IN BLOCK TO LEFT	
25.	0010358 NM=NR(KM) \$ XN1=(NM-1)*DXA(KM)-XN(KM,NM-1)	
27.	0010438 HJ=XN(K,1)+XN1 \$ HJP=XN(K,2)-XN(K,1)	
29.	0010478 AL(1)=HJP/(HJ+HJP) \$ AM(1)=1.-AL(1)	
31.	0010528 C(1)=3.*AL(1)*(Y(K,1)-YN(KM,NM-1))/HJ +3.*AM(1)*(YN(K,2)-YN(K,1))	
	*/HJP	
32.	0010668 GC TO 30	
33.	0010668 20 CCNTINUE	
34.	0010708 IA=2 \$ DN(K,1)=C.	
36.	0010718 30 CCNTINUE	
	C CHECK IF LAST PT IN SAME BLOCK	
37.	0010738 XR=(N-1)*DZA \$ XN=XN(K,N) \$ NT=N	
40.	0011008 IF(XM.GE.XR) GO TO 50	
	C USE PTS FROM KP BLOCK NOW IN KTH BLOCK	
41.	0011038 DC 40 IL=1,5	
42.	0011048 XM=XN(KP,IL+1)+XR \$ NT=N+IL	
44.	0011108 XN(K,NT)=XM \$ YN(K,NT)=YN(KP,IL+1)	
46.	0011178 IF(XM.GE.XR) GO TO 50	
47.	0011178 40 CCNTINUE	
48.	0011248 CALL ABORT	
49.	0011268 50 CCNTINUE	
	C CALC INTERIOR CONSTS	
50.	0011268 AL1=NT-1 \$ HJ=XN(K,2)-XN(K,1)	
52.	0011318 DO 60 I=2,NL1	
53.	0011348 HJP=XN(K,I+1)-XN(K,I) \$ AL(I)=HJP/(HJ+HJP) \$ AM(I)=1.-AL(I)	
56.	0011428 C(I)=3.*AL(I)*(Y(K,I)-YN(K,I-1))/HJ +3.*AM(I)*(YN(K,I+1)-YN(K,I))	
	*/HJP	
57.	0011548 HJ=HJP	
58.	0011558 60 CCNTINUE	
59.	0011568 IF(K.EQ.KB) GO TO 70	
	C FOR RH PT	
60.	0011608 HJ=XN(K,NT)-XN(K,NL1) \$ HJP=XN(KP,IL+2)-XN(K,NT)+XR	
62.	0011728 AL(NT)=HJP/(HJ+HJP) \$ AM(NT)=1.-AL(NT)	
64.	0011748 C(NT)=3.*AL(NT)*(Y(K,NT)-YN(K,NL1))/HJ +3.*AM(NT)*(YN(KP,IL+2)-YN(K,NT))/HJP	
65.	0012158 IB=NT	
66.	0012168 GC TO 80	
67.	0012168 70 CCNTINUE	

DEF **SUBROUTINE DEP** PAGE 2

```

66. C012208 IB=N-1 & DA(KB,N)=0.
70. C012238 80 CONTINUE
71. C012248 CALL TCMEY(IA,IB,AL,AM,C,DD)
72. C012268 DO 85 I=1A,1B
73. C012308 85 DN(K,I)=DD(I)
      C INTERPOLATE TO PREVIOUS X-GRID
74. C012348 II=2
75. C012358 DC 105 I=2,AM1
76. C012378 XP=(I-1)*DZA
77. C012418 DC 90 IT=II,NT
78. C012448 XJ=XN(K,IT)
79. C012468 IF(XJ.GT.XP) GO TO 100
80. C012478 90 CONTINUE
81. C012548 100 CONTINUE
82. C012558 II=IT & IM=IT-1 & XJM=XN(K,IP)
85. C012618 HJ=XN(K,IT)-XN(K,IM) & HS=HJ*HJ & HC=HJ*HS
88. C012668 T1=XJ-XP & T2=XP-XJM
90. C012728 Y(K,I)= DN(K,IM)*T1*T1*T2/HS -DN(K,IT)*T2*T2*T1/HS +YA(K,IM)*T1*T1
      ** (2.*T2+HJ)/HC +YA(K,IT)*T2*T2*(2.*T1+HJ)/HC
91. C013178 105 CONTINUE
      C EQUATE Y(KP,I) TO Y(K,N)
92. C013218 IF(K.EQ.KB) GO TO 110
93. C013238 Y(K+1,I)=Y(K,N)
94. C013258 110 CONTINUE
95. C013318 RETURN
96. C013338 END

```

CECM **SLBROUTINE GECP** PAGE 1

```

1. C000008 SLBROUTINE GECP
2. C000009 COMMON/BLOAT/BV(6),DX(6),DXA(6),IGR(6),KB,ML(6),NAS(6),AR(6)
3. C000008 COMMON/RDIS/RS
4. C000008 COMMON/YDIS/Y(1,101),MA(1,101)
      C DEFINE PROBLEM GEOMETRY
5. C000008 PI=3.1415926
6. C000008 DZA=DXA(1)
7. C000008 N=AR(1)
8. C000038 DO 200 I=1,N
9. C000068 T1=PI*(I-1)*DZA
10. C000118 Y(I,1)=3.*.20*CCS(T1)
11. C000178 200 CONTINUE
12. C000278 RETURN & END

```

GFAC		**SUBROUTINE GFAC (XR,XU,XL,LL,IS,JS)**	PAGE 1
1.	0000008	SLBROUTINE GFAC (XR,XU,XL,LL,IS,JS)	
		C DETN DISTANCE FROM NODES NEAR SURFACE WHERE NO ADJACENT NODE EXISTS	
2.	0000008	DIMENSION XR(1,101),XU(1,101),XL(1,101),LL(6),IS(1,101),JS(1,101)	
3.	0000008	COMMON/BLDAT/BV(6),DX(6),DXA(6),IGR(6),KB,ML(6),MAS(6),NR(6)	
4.	0000008	COMMON/DRIV/DI(1,101)	
5.	0000008	COMMON/UPDIS/DU(1,101)	
6.	0000008	COMMON/YDIS/YI(1,101),MA(1,101)	
		C COMPUTE DISTANCE TO BORDER PTS	
7.	0000008	DO 110 K=1,KB	
8.	0000028	N=NR(K) \$ KM=K-1 \$ BVV=BV(K) \$ CZA=CXA(K) \$ L=0 \$ DXX=DZA	
14.	0000108	NMI=N-1	
15.	0000128	IF(K.EQ.KB) AMI=AMI+1	
16.	0000178	DO 100 I=1,NMI	
17.	0000218	MAA=MA(K,I) \$ MAN=MAA-1 \$ ZL=DZA \$ IR=DZA	
21.	0000268	DO 90 JJ=1,MAN	
22.	0000328	LN=L	
23.	0000328	J=MAA-JJ	
24.	0000348	YP=BVV*(J-1)*DZA \$ YY=Y(K,I)	
26.	0000428	IF((K.EQ.KB).AND.(I.EQ.N)) GO TO 10	
27.	0000518	YR=Y(K,I+1)	
28.	0000538	IF((K.EQ.1).AND.(I.EQ.1)) GO TO 70	
29.	0000618	IF(I.EQ.1) GO TO 20	
		C K=KB, I=AMI	
30.	0000618	10 CONTINUE	
31.	0000648	VL=Y(K,I-1)	
32.	0000658	GC TO 30	
		C K NE 1, I=1	
33.	0000668	20 NMN=NR(KM)-1	
34.	0000708	VL=Y(KM,NMN)	
35.	0000728	30 CONTINUE	
		C CHECK LHS	
36.	0000748	IF(VL.LT.YP) GO TO 40	
37.	0000768	GO TO 70	
38.	0000768	40 CCNTINUE	
39.	0000778	L=LN+1	
		C SAVE COORD OF BORDER PTS	
40.	0001008	IS(K,L)=I \$ JS(K,L)=J	
42.	0001058	DD=D(K,I)	
43.	0001068	IF(I.EQ.1) GO TO 50	
44.	0001108	DM=D(K,I-1)	
45.	0001128	GO TO 60	
46.	0001128	50 CCNTINUE	
47.	0001148	DM=D(KM,NMN) \$ DXX=DXA(KM)	
49.	0001178	60 CCNTINUE	
50.	0001218	CALL INVSPL(DXX,CP,DD,VL,VY,YP,XX)	
51.	0001238	ZL=ABS(XX)	
52.	0001248	70 CCNTINUE	
53.	0001258	XX=0.	
54.	0001258	IF((K.EQ.KB).AND.(I.EQ.N))GO TO 85	
		C CHECK RHS	
55.	0001348	IF(YR.LT.YP) GO TO 80	
		C STOP CHECKING WHEN NO BORDER PT FOUND	
56.	0001368	GO TO 85	
57.	0001378	80 L=LN+1	
58.	0001408	IS(K,L)=I \$ JS(K,L)=J \$ DM=D(K,I) \$ DD=D(K,I+1)	
62.	0001508	CALL INVSPL(DZA,DM,DD,VY,YR,YP,XX)	
63.	0001538	85 IF (L.EQ.LN) GO TO 100	

[illegible]

INVSPL	**SLROUTINE INVSPL(DZA,CM,DC,YM,YY,YB,X)**	PAGE 1
1. 00000CB	SLROUTINE INVSPL(DZA,CM,DC,YM,YY,YB,X)	
	C INVERSE INTERPOLATE USING CUBIC SPLINE	
	C INITIAL ESTIMATE	
2. CCCCC0B	H= DZA & HS=H*H & HC=H*H & L=0 & E=1.E-6*DZA & T=-DZA	
8. 000006B	PRO=(YM-YB)/(YM-YY)	
9. 000012B	X=(PRO-1.)*H	
10. 000014B	10 CCNTINUE	
11. 000015B	L=L+1 & XS=X*X & XC=X*X	
14. 000017B	FX= DP*(XC-T*XS)/HS+DD*(XC-2.*XS+T*x*HS)/HS+YM*(2.*XC-2.*T*XS+H*XS *1/HC+YY*(XS-2.*T*XS+HS)*(H-2.*X)/HC-YB	
15. 000053B	IF(ABS(FX).LT.E) GO TO 40	
16. 000056B	IF(L.GT.20) GO TO 20	
	C SOLVE BY NEWTONS METHOD	
17. C0CC57B	UY=DM*(3.*XS-2.*T*X)/HS+DD*(3.*XS-4.*T*X+HS)/HS+YM*(6.*XS-4.*T* *X+2.*H*X)/HC+YY*((-XS+2.*T*X-HS)*2+(H-2*X)*(2*X-2*T))/HC	
18. 000117B	X=X-FX/DY	
19. C0C122B	GO TO 10	
20. 000122B	20 CCNTINUE	
21. C0C123B	PRINT 30,X,FX,YP,YY,YB,DP,DD,CY,DZA,L	
22. 000140B	30 FORMAT (* X FX YM YY YB DM DD DY DZA L *)	
	*9(1PE10.2), (5)	
23. 00C140B	CALL ABORT	
24. 00C142B	40 CONTINUE	
25. 00C142B	RETURN	
26. 00C144B	END	

PHAP	**SLROUTINE PHAP**	PAGE 1
1. CCCCC0B	SLROUTINE PHAP	
2. 000000B	COMMON/BLDAT/BV(6),DX(6),DXA(6),IGR(6),KB,PL(6),NAS(6),NR(6)	
3. 000000B	COMMON/YOIS/Y(1,101),MA(1,101)	
4. 000000B	COMMON P(1,5),S(1,5),PA(1,101,101),PT(1,101)	
5. 000000B	DO 1050 K=1,KB	
6. 000002B	PRINT 1020,K	
7. 000007B	1020 FORMAT(/** BLOCK*13)	
8. 000007B	N=NR(K) & IGR=IGR(K) & PLL=PL(K) & NM1=N-1	
12. 00CC14B	IF(K.EQ.KB) NM1=NM1+1	
13. 00CC20B	IF(IGR.EQ.1) GO TO 1026	
14. 000C21B	PRINT 1021	
	C PRINT MG	
15. 000025B	1021 FORMAT (10X*MAIN GRID POTENTIALS*)	
16. 000025B	DC 1025 I=1,NM1,IGR	
17. 00CC30B	IM=1/IGR+1	
18. 000032B	PRINT 1022,I,IM	
19. C0CC41B	1022 FORMAT(* ROW AG/MG*2I3)	
20. 000041B	PRINT 1040,(P(K,IM,J),J=1,PLL)	
21. 000056B	1025 CCNTINUE	
22. C0CC61B	1026 CCNTINUE	
	C PRINT INTERMEDIATE RESULTS FOR AG	
23. C0CC61B	PRINT 1028	
24. 000064B	1028 FORMAT (/*AUX GRID POTENTIALS*)	
25. 000064B	DC 1050 I=1,NM1	
26. 00CC66B	PRINT 1030,I	
27. 000073B	1030 FORMAT(* ROW*13)	
28. C0CC73B	MAA=MA(K,I)	
29. 000075B	PRINT 1040,(PA(K,I,J),J=1,MAP)	
30. 00C114B	1040 FCRPAT(2X,10(1PE12.4))	
31. C0C114B	1050 CONTINUE	
32. 00C121B	RETURN & END	

SETUP		**SUBROUTINE SETUP**	PAGE 1
1.	000000B	SUBROUTINE SETUP	
		C CCNSTRCT AUXILIARY AND MAIN GRIDS	
2.	000000B	COMMON/BLDAT/BV(6),DX(6),DZA(6),IGR(6),KB,PL(6),NAS(6),NR(6)	
3.	000000B	COMMON/UPCIS/CU(1,101)	
4.	000000B	COMMON/YOIS/Y(1,101),MA(1,101)	
		C DEFINE AUXILIARY (FINE) GRID	
5.	000000B	T1=.005*DZA(1)	
6.	000001B	DO 120 K=1,KB	
7.	000004B	DZ=DX(K) \$ DZA=CXA(K) \$ N=NR(K)	
10.	000007B	T=(DZ+T1)/DZA \$ IGR(K)=IFIX(T) \$ IGR=IGR(K) \$ YL=Y(K,1)	
		C FIND LOWEST PT IN BLOCK	
14.	000015B	IF(IGR.EQ.1) GO TO 110	
15.	000020B	DO 100 I=2,N	
16.	000023B	YY=Y(K,I)	
17.	000025B	IF(YY.LT.Y(K,I-1)) YL=YY	
18.	000032B	100 CONTINUE	
19.	000034B	T=(YL+T1-NAS(K)*DZ)/DZ	
20.	000041B	ML(K)=IFIX(T)+1	
		C CHECK THAT LOWER BOUND ABOVE BASE	
21.	000042B	IF(ML(K).LT.1) PL(K)=1	
22.	000046B	GO TO 115	
23.	000046B	110 CCATINUE	
24.	000047B	ML(K)=1	
25.	000047B	115 CCATINUE	
26.	000051B	I1=1 \$ NM1=N-1 \$ PLL=ML(K) \$ DZ=DZA(K)	
30.	000056B	BV(K)=(ML-1)*DZ \$ BVV=BV(K)	
32.	000061B	IF(IGR.EQ.KB) AM1=N	
		C DEFINE MAX AG PT	
33.	000065B	DO 120 I=1,NM1	
34.	000067B	YY=Y(K,I)	
35.	000071B	MA(K,I)=IFIX((YY-BVV)/DZA)+2	
36.	000074B	DU(K,I)=YY-BVV-(MA(K,I)-2)*DZA	
37.	000100B	IF(DU(K,I).GT.T1) GO TO 120	
38.	000104B	MA(K,I)=MA(K,I)-1 \$ DU(K,I)=DZA	
40.	000107B	120 CCATINUE	
41.	000115B	RETURN	
42.	000117B	END	

SFLA

SUBROUTINE SPLN

PAGE 1

```

1. 0000000 SUBROUTINE SPLN
C DETERMINE THE DERIVATIVES AT THE SURFACE NODES WITH THE CUBIC SPLINE
2. 0000000 DIMENSION AL(101),AM(101),DD(101),C(101)
3. 0000000 CCPPCN/BLCAT/2V(6),DX(6),DZA(6),IGR(6),KB,ML(6),NAS(6),NR(6)
4. 0000000 COMMON/DRIV/D(1,101)
5. 0000000 COMMON/YOIS/Y(1,101),MA(1,101)
6. 0000000 DO 70 K=1,KB
7. 0006268 DZA=DZA(K) & KM=K-1 & N=NR(K) & NM1=N-1
C CALC CONSTS FOR INTERIOR
11. 0006328 DC 10 I=2,NM1
12. 0006358 AL(I)=.5 & AM(I)=.5
14. 0006368 10 C(I)=1.5*(Y(K,I+1)-Y(K,I-1))/DZA
15. 0006458 IF(KB.EQ.1) GO TC 20
16. 0006478 IF(K.EQ.1) GC TC 30
17. 0006518 IF(K.EQ.KB) GC TC 40
18. 0006538 NM=NR(KM)-1 & DMA=DZA(KM)
20. 0006568 AL(1)=DZA/(DMA+DZA) & AM(1)=1.-AL(1)
22. 0006628 C(1)= 3.*AL(1)*(Y(K,1)-Y(KM,NM))/DMA+3.*AM(1)*(Y(K,2)-Y(K,1))/DZA
23. 0006768 IA=1
24. 0006778 GC TO 50
C FOR SINGLE BLOCK
25. 0006778 20 CONTINUE
26. 0007018 D(1,1)=0. & D(1,N)=0. & IA=2
29. 0007048 GC TO 50
30. 0007048 30 CONTINUE
C FIRST BLOCK
31. 0007058 D(1,1)=0. & IA=2
33. 0007068 GC TO 50
C LAST BLOCK
34. 0007068 40 CONTINUE
35. 0007108 D(KB,N)=0. & NM=NR(KM)-1 & DMA=DZA(KM)
38. 0007158 AL(1)=DZA/(DMA+DZA) & AM(1)=1.-AL(1)
40. 0007218 C(1)=3.*AL(1)*(Y(KB,1)-Y(KM,NM))/DMA+3.*AM(1)*(Y(KB,2)-Y(KB,1))/
    *DZA
41. 0007358 IA=1
42. 0007368 50 CONTINUE
43. 0007378 CALL TOMET (IA,NM1,AL,AM,C,DD)
44. 0007418 DO 60 I=IA,NM1
45. 0007448 60 D(K,I)=DD(I)
46. 0007478 70 CONTINUE
C EQUATE D(K,N) TO D(K+1,1)
47. 0007528 IF(KB.EQ.1) GO TC 75
48. 0007538 KBM=KB-1
49. 0007558 DC 65 K=1,KBM
50. 0007578 N=NR(K)
51. 0007578 65 D(K,N)=D(K+1,1)
52. 0007638 75 CONTINUE
53. 0007648 RETURN
54. 0007668 END

```

SMOOTH		**SUBROUTINE SMOOTH**	PAGE 1
1.	0000008	SUBROUTINE SMOOTH	
2.	0000008	DIMENSION W(101),R(101),A(500),YY(101),XX(101)	
3.	0000008	COMMON/BCFG/XN(1,101),YN(1,101)	
4.	0000008	COMMON/BLDAT/BV(6),DX(6),DXA(6),IGR(6),KB,ML(6),NAS(6),NR(6)	
5.	0000008	N=NR(1) \$ NM1=N-1 \$ W(1)=-1	
8.	0016138	L=.5*N	
9.	0016168	GC TO 30	
10.	0016178	ER=1.E-5	
> (10)	WARNING	-----CANNOT BE EXECUTED - NO STATEMENT NUMBER	
11.	0016208	PRINT 40,ER	
12.	0016258	40 FORMAT(* RMS SMOOTHING* IPE12.4)	
13.	0016258	DO 5 I=1,N	
14.	0016278	XX(I)=XN(I,I)	
15.	0016308	5 YY(I)=YN(I,I)	
16.	0016338	PRINT 10,(YY(I),I=1,N)	
17.	0016448	10 FORMAT(* YN*10F10.7)	
18.	0016448	CALL POLFIT(A,XX,YY,W,L,NGRD,ER,R,IERR,A)	
19.	0016468	PRINT 15,NGRD,ER,IERR,L	
20.	0016558	15 FORMAT(* ORDER CCMP,RMS ERR,FLG,MAX ORDER*15,IPE12.4,215)	
21.	0016558	DO 20 I=1,N	
22.	0016578	YN(I,I)=R(I)	
23.	0016578	20 CONTINUE	
24.	0016638	PRINT 10,(R(I),I=1,N)	
25.	0016738	30 CONTINUE	
26.	0016738	RETURN \$ END	
>	CAUTION	-----NM1 WAS SET BUT NEVER USED	

```

**SUBROUTINE TONET (IA, IB, AL, AM, C, DO)**
      PAGE 1

      1. 0000008 C SUBROUTINE TONET (IA, IB, AL, AM, C, DO)
      2. 0000008 C INVERT THE TRIANGULAR MATRIX USING THE THOMAS METHOD
      3. 0000008 DIMENSION AL(101),AM(101),DO(101),G(101),W(101),Q(101),C(101)
      4. 0000008 W(IA)=2.5*(IA-C(IA))/2.
      5. 0004628 IB=IB-15*(IA-C(IA))/2.
      6. 0004628 DO 10 I=IA,IB
      7. 0004628 W(I)=1.5*(IA-C(IA))/2.
      8. 0004628 IB=IB-15*(IA-C(IA))/2.
      9. 0004628 W(I)=1.5*(IA-C(IA))/2.
      10. 0004628 DO 10 I=IA,IB
      11. 0004628 W(I)=1.5*(IA-C(IA))/2.
      12. 0004628 DO 10 I=IA,IB
      13. 0004628 W(I)=1.5*(IA-C(IA))/2.
      14. 0004628 DO 10 I=IA,IB
      15. 0004628 W(I)=1.5*(IA-C(IA))/2.
      16. 0004628 DO 10 I=IA,IB
      17. 0004628 W(I)=1.5*(IA-C(IA))/2.
      18. 0004628 DO 10 I=IA,IB
      19. 0004628 W(I)=1.5*(IA-C(IA))/2.
      20. 0004628 DO 10 I=IA,IB
      21. 0004628 W(I)=1.5*(IA-C(IA))/2.
      22. 0004628 W(I)=1.5*(IA-C(IA))/2.

```


APPENDIX E

DEPOSITION ON A SINUSOIDAL PROFILE

The behavior of the sinusoidal cathode as it undergoes deposition is treated in this section. In this problem the solution side of the anode is equipotential (i.e., there is no current dependence of overpotential), but surface overpotential, described by Tafel kinetics, and concentration overpotential, described by Eq. (4), are present at the cathode. In addition, the anode is assumed to be inert so that it does not dissolve upon passage of current.

The choices of the parameters are shown on the first page of output. The Tafel slope is $B = 0.1$ V and $i_o = 0.001$ A/cm². A main grid spacing of 0.2 cm and an auxiliary grid spacing of 0.1 cm are used. The anode is set 10 V higher than the cathode potential, which is at 1 V. The overrelaxation parameter of 1.85 is used for all computations. The convergence criterion for potentials in the bulk is $ERR = 10^{-6}$. In principle, the relative change in potential for each node on successive iterations must be less than 10^{-6} . In practice, to save computation time, only the nodes at the periphery are tested for convergence. Three convergence criteria must be met simultaneously for convergence to occur: the relative change in potentials in the bulk must be less than ERR , the relative change in surface potentials (which result from a numerical differentiation) must be less than $1000\ ERR = 10^{-3}$, and the average relative change in current density must be less than $10\ ERR = 10^{-5}$.

Five hundred iterations are specified as the maximum number of iterations per time step. When this limit is exceeded, the computation halts. Two time steps are specified; the computation halts after the

second step. In order to suppress the potential map, a large number of iterations (8000) is specified. The electrolyte conductivity is $1 \text{ ohm}^{-1} \text{ cm}^{-1}$. For the formula weight, metal density, and valence, the values for copper are used. With 100 percent faradaic efficiency, $3.7 \times 10^{-5} \text{ cm}^3$ of metal is deposited per coulomb of charge. Since a higher current density is expected near the peak, the surface node of the tenth row of the block is chosen as a point where a high current density occurs; this point is used for initial estimate and convergence calculations. The pre-logarithmic factor in Eq. (6) is $1.3 \times 10^{-2} \text{ V}$. In this problem I have specified that the highest current density point is at 50 percent of the limiting current density. Alternatively, one can specify a diffusion layer depth and other constants which determine a limiting current. The number of coulombs/time step is specified as 750.

Under $T = 0$ in the output, the initial geometry and initial estimates of the surface potential are printed out. The row number, the X and Y coordinates, and the number of points in the auxiliary grid in each row, as illustrated in the output below, are printed out. The initial estimates of the current and potential, as calculated from the tenth row (IC), are also listed. The derivatives are calculated numerically from the cubic spline. For certain nodes adjacent to the surface, the distances from the nodes to the surface and to surrounding points are listed after the geometric map.

The convergence status status is printed (from line 780 in routine CURDIS) each time the surface potential is re-evaluated. The headings explain the numbers which appear immediately below. From the current

balance one can see that the anodic and cathodic currents are within 0.02 percent of each other. The coulombs passed is also printed.

In the first time step, the time for deposition is printed out. The new coordinates just after deposition are printed along with the coordinates which result from interpolating back to the original X-coordinates. The current densities and the X and Y components of the current density are shown. The last column (not labeled) is the concentration overpotential in volts. The profile at each time step is illustrated in Fig. 10.

The execution time for this problem is 0.6 s on a CDC 7600. A total of approximately 150 nodes are used in the calculation and 360 iterations are required in the potential loop; 23 iterations in the current and surface potential loops are required. This amounts to an average computation time of 10^{-5} s per node. The total job cost including compilation and overhead is \$1.45.

```

TAFEL PLARIZATION PARAMETERS B= 1.COE-01 VCLTS 10= 1.COE-03 A/CM2Q
BLOCK MAIN GRID AUX GRID AUX SQUARES WIDTH (CM)
1 .200 .100 3 1.000
ANODE POTENTIAL= 11.00000 CATHODE POTENTIAL= 1.00000 VCLTS
CYCLES RELAXATION PARAMETER 1.05
CONVERGENCE CRITERION= 1.COE-06
MAX FIELD ITERATIONS 500 MAX TIME STEPS 2
POTENTIAL MAP OUTPUT EVERY 8000 ITERATIONS
ELECTROLYTE CONDUCTIVITY 1.00E+00(OHM-CM)-1
FORMULA BT 63.50000 G/G-A DENSITY 8.89000 G/CC VALENCE 2.00000 FARADAY EFF 1.00000 DEP FACTOR 3.70096E-05CC7C
COORDINATES OF HIGH CO POINTS K= 1 I= 10
CPC,RT/AF 1.30E-02 NFCC(BULK) 1.00E-03 DIFFUSION LAYER 1.50E-04 CM LHM CURRENT 6.67E+00
CULOMBS/TIME STEP 7.50000E+02
SPECIFIED FRACTION OF LIMITING CURRENT .50000

```

TIME= 0. SEC TIME STEP= 0

[illegible]

ITER	AVERAGE POTENTIAL ERROR	CENSTST FACTOR	CURRENT ERROR	WAGNER FACTOR	CURRENT MULT FACTOR	DAMPING FACTOR	BOUNDARY ERROR	CD(KC,IC)	BOUNDARY POTENTIAL (KC,IC)	CD(I,1)	BOUNDARY POTENTIAL (I,1)	AVERAGE CURRENT ERROR
26	6.448E-05	1.000E+00	3.012E-01	9.916E-01	1.195E+00	3.587E-01	2.569E-02	4.723E+00	1.826E+00	1.355E+00	1.778E+00	4.642E-03
45	8.342E-05	1.000E+00	8.182E-02	9.914E-01	1.434E+00	1.165E-01	1.511E-02	4.639E+00	1.829E+00	1.433E+00	1.773E+00	2.247E-02
56	6.684E-05	1.000E+00	3.604E-01	9.914E-01	1.721E+00	6.152E-01	1.326E-02	4.626E+00	1.844E+00	1.447E+00	1.746E+00	3.550E-03
74	6.516E-05	1.000E+00	1.214E-01	9.913E-01	2.061E+00	2.486E-01	4.242E-03	4.569E+00	1.845E+00	1.504E+00	1.743E+00	1.449E-02
83	3.829E-05	1.000E+00	4.028E-01	9.913E-01	2.479E+00	9.898E-01	3.033E-01	4.560E+00	1.851E+00	1.509E+00	1.734E+00	2.967E-03
103	2.942E-05	1.000E+00	2.751E-01	9.912E-01	2.974E+00	8.112E-01	2.776E-04	4.537E+00	1.851E+00	1.526E+00	1.735E+00	5.273E-03
137	1.778E-07	6.000E-01	6.538E-01	9.912E-01	2.142E+00	8.329E-01	6.883E-05	4.539E+00	1.851E+00	1.525E+00	1.735E+00	1.059E-03
163	1.341E-07	6.000E-01	7.331E-01	9.912E-01	1.028E+00	4.331E-01	3.534E-05	4.539E+00	1.851E+00	1.524E+00	1.735E+00	7.286E-04
174	2.373E-07	7.260E-01	8.545E-01	9.912E-01	4.934E-01	3.035E-01	4.998E-06	4.539E+00	1.851E+00	1.524E+00	1.735E+00	3.407E-04
182	1.445E-07	7.866E-01	9.873E-01	9.912E-01	2.842E-01	2.222E-01	2.308E-06	4.539E+00	1.851E+00	1.524E+00	1.735E+00	2.585E-05

CAT-ODE CURRENT	3.1224CE+00	ANODE CURRENT	3.12291E+00	CATH CCUL 1 TS	7.50000E+02	ANODE COUL 1 TS	7.50124E+02
TOTCATH COUL	7.50000E+02	TOT ANODE CCUL	7.50124E+02				

AVG CURRENT 2.71102E+00

AVERAGE ERROR PER NCCE 2.401E-07 ITERATIONS 183 UNCONVERGED POINTS 0

ITERATIONS IN CURRENT LCUP 12

183 2.401E-07 8.765E-01 9.964E-01 9.912E-01 1.637E-01 1.421E-01 1.496E-06 4.539E+00 1.851E+00 1.524E+00 1.735E+00 7.495E-06

TIME= 2.40200E+02 SEC TIME STEP= 1

BLOCK	1	BY=	2.00	ROW	AG	X-COORD	Y-COORD	NEW X	NEW Y	DERIVATIVE	CURRENT	X-COMPONENT	Y-COMPONENT	BOUNDARY
					PTS	(CM)	(CM)	COORDINATE	COORDINATE		(A/CMSQ)			POTENTIAL
1	13	0.				3.1865E+00	0.	3.1865E+00	0.		1.5241E+00	0.	-1.5241E+00	1.7353E+00 .002
2	13	1.0000E-01				3.1760E+00	9.7345E-02	3.1765E+00	-2.0746E-01	1.5672E+00	-2.4339E-01	-1.5492E+00	1.7381E+00 .002	
3	13	2.0000E-01				3.1456E+00	1.9477E-01	3.1476E+00	-3.9565E-01	1.6977E+00	-4.9112E-01	-1.6283E+00	1.7463E+00 .003	
4	12	3.0000E-01				3.0981E+00	2.6226E-01	3.1023E+00	-5.4534E-01	1.9219E+00	-7.4474E-01	-1.7774E+00	1.7551E+00 .003	
5	12	4.0000E-01				3.0383E+00	3.8582E-01	3.0448E+00	-6.4310E-01	2.2314E+00	-1.0143E+00	-1.9934E+00	1.7746E+00 .004	
6	11	5.0000E-01				2.9717E+00	4.8751E-01	2.9801E+00	-6.7621E-01	2.6413E+00	-1.2513E+00	-2.3331E+00	1.7923E+00 .004	
7	11	6.0000E-01				2.9052E+00	5.8575E-01	2.9144E+00	-6.4443E-01	3.1169E+00	-1.4641E+00	-2.7561E+00	1.8058E+00 .005	
8	10	7.0000E-01				2.8450E+00	6.8516E-01	2.8532E+00	-5.4615E-01	3.6838E+00	-1.5247E+00	-3.3574E+00	1.8278E+00 .007	
9	9	8.0000E-01				2.7508E+00	7.8705E-01	2.8031E+00	-3.8729E-01	4.2043E+00	-1.4050E+00	-3.9625E+00	1.8422E+00 .008	
10	9	9.0000E-01				2.7686E+00	8.9231E-01	2.7702E+00	-1.5684E-01	4.5392E+00	-9.5578E-01	-4.4384E+00	1.8508E+00 .009	
11	5	1.0000E+00				2.7588E+00	1.0000E+00	2.7588E+00	0.	4.6324E+00	0.	-4.6324E+00	1.8531E+00 .009	
LIM CUR						9.26482E+00	CONC OVERPOTENTIAL	8.75193E-03						
K	IS	JS	L	XL	XU	XR								
1	3	12	1	1.00E-01	4.56E-C2	5.66E-02								
K	IS	JS	L	XL	XU	XR								
1	5	11	2	1.00E-01	3.83E-02	5.80E-02								
K	IS	JS	L	XL	XU	XR								
1	7	10	3	1.00E-01	5.18E-03	8.08E-03								
K	IS	JS	L	XL	XU	XR								
1	8	9	4	1.00E-01	4.50E-C2	5.48E-02								

ITER	AVERAGE	CONSIST	CURRENT	WAGNER	CURRENT	DAMPING	BOUNDARY	CD(KC,IC)	BOUNDARY	CD(1,1)	BOUNDARY	AVERAGE
	POTENTIAL	FACTOR	ERRGR	FACTOR	MULT	FACTOR	ERROR	POTENTIAL	POTENTIAL	POTENTIAL	POTENTIAL	CURRENT
	ERROR				FACTOF			(KC,IC)	(KC,IC)	(1,1)	(1,1)	ERRGR
68	8.072E-05	1.000E+00	4.855E-01	9.615E-01	1.189E+00	5.725E-01	2.021E-03	4.724E+00	1.853E+00	1.433E+00	1.732E+00	2.121E-03
78	9.124E-06	1.000E+00	4.386E-01	9.915E-01	1.427E+00	6.207E-01	7.307E-04	4.721E+00	1.854E+00	1.448E+00	1.731E+00	2.561E-03
112	3.672E-07	1.000E+00	6.565E-01	9.914E-01	1.713E+00	9.916E-01	2.340E-04	4.716E+00	1.855E+00	1.446E+00	1.730E+00	1.045E-03
141	4.100E-07	1.000E+00	7.490E-01	9.914E-01	1.233E+00	9.159E-01	3.745E-05	4.714E+00	1.855E+00	1.449E+00	1.730E+00	6.706E-04
158	8.556E-08	6.000E-01	8.007E-01	9.914E-01	2.960E-01	1.411E-01	2.663E-05	4.714E+00	1.855E+00	1.447E+00	1.730E+00	4.981E-04
165	1.820E-07	6.600E-01	9.571E-01	9.914E-01	1.705E-01	1.069E-01	1.815E-05	4.714E+00	1.855E+00	1.448E+00	1.730E+00	8.984E-05
171	8.990E-08	7.260E-01	9.796E-01	9.914E-01	9.820E-02	6.934E-02	1.384E-05	4.714E+00	1.855E+00	1.448E+00	1.730E+00	4.180E-05
175	5.248E-08	7.586E-01	9.851E-01	9.914E-01	5.657E-02	4.440E-02	1.165E-05	4.714E+00	1.855E+00	1.448E+00	1.730E+00	2.224E-05
176	2.511E-07	8.765E-01	9.945E-01	9.914E-01	3.258E-02	2.832E-02	1.052E-05	4.714E+00	1.855E+00	1.448E+00	1.730E+00	1.120E-05

CAT-ODE CURRENT 3.16577E+00 ANODE CURRENT 3.16081E+00 CATH CCUL I TS 7.50000E+02 ANODE COUL I TS 7.47880E+02

TCTCATH COUL 1.50000E+03 TOT ANODE COUL 1.45800E+03

AVG CURRENT 2.74152E+00

AVERAGE ERROR PER NCCE 1.012E-07 ITERATIONS 177 UNCONVERGED POINTS 0

ITERATIONS IN CURRENT LOOP 11

177 1.012E-07 9.663E-01 9.958E-01 9.914E-01 1.677E-02 1.801E-02 9.840E-06 4.714E+00 1.855E+00 1.448E+00 1.730E+00 8.588E-06

TIME= 4.76810E+02 SEC TIME STEP= 2

BLOCK 1

BY= 2.00	ROW	AG	X-COORD	Y-COORD	NEW X	NEW Y	DERIVATIVE	CURRENT	X-COMPONENT	Y-COMPONENT	BOUNDARY
	PIS		(CM)	(CM)	COORDINATE	COORDINATE		(A/CMS)			POTENTIAL
	1	13	0.	3.1738E+00	0.	3.1738E+00	0.	1.4477E+00	0.	-1.4477E+00	1.7299E+00 .002
	2	13	1.0000E-01	3.1626E+00	5.7345E-02	3.1632E+00	-2.2123E-01	1.4926E+00	-2.4559E-01	-1.4734E+00	1.7329E+00 .002
	3	13	2.0000E-01	3.1302E+00	1.9477E-01	3.1324E+00	-4.2281E-01	1.6248E+00	-4.9535E-01	-1.5513E+00	1.7417E+00 .002
	4	12	3.0000E-01	3.0794E+00	2.9222E-01	3.0839E+00	-5.8439E-01	1.8546E+00	-7.6073E-01	-1.6976E+00	1.7553E+00 .003
	5	12	4.0000E-01	3.0151E+00	3.8568E-01	3.0222E+00	-6.9110E-01	2.1779E+00	-1.0417E+00	-1.9194E+00	1.7719E+00 .003
	6	11	5.0000E-01	2.9434E+00	4.8720E-01	2.9528E+00	-7.3011E-01	2.6085E+00	-1.3143E+00	-2.2602E+00	1.7908E+00 .004
	7	10	6.0000E-01	2.8716E+00	5.8508E-01	2.8820E+00	-6.9479E-01	3.1454E+00	-1.5245E+00	-2.7555E+00	1.8105E+00 .005
	8	10	7.0000E-01	2.8069E+00	6.8432E-01	2.8163E+00	-5.8501E-01	3.7364E+00	-1.6618E+00	-3.3458E+00	1.8250E+00 .006
	9	9	8.0000E-01	2.7568E+00	7.8630E-01	2.7626E+00	-4.0753E-01	4.3314E+00	-1.4898E+00	-4.0678E+00	1.8451E+00 .008
	10	9	9.0000E-01	2.7264E+00	8.9203E-01	2.7281E+00	-2.0011E-01	4.7144E+00	-1.0064E+00	-4.6067E+00	1.8546E+00 .009
	11	9	1.0000E+00	2.7166E+00	1.0000E+00	2.7166E+00	0.	4.8237E+00	0.	-4.8237E+00	1.8571E+00 .009
	LIM CUR		9.6474E+00	CCAC	CVERPCTENTIAL	8.71945E-03					

```

.77777777.77777777.77777777.77777777.77777777.77777777.77777777.77777777.77777777.77777777.77777777.77777777.77
.77777777.77777777.77777777.77777777.77777777.77777777.77777777.77777777.77777777.77777777.77777777.77777777.77
.77777777.77777777.77777777.77777777.77777777.77777777.77777777.77777777.77777777.77777777.77777777.77777777.77

```

APPENDIX F

CALCULATION OF NODE POTENTIALS

In order to calculate the potential at node zero in Fig. a, the distances between the node zero and the surrounding four numbered nodes is determined (see subroutine GFAC). The distance between node 0 and node 1 is denoted as h_1 , between node 0 and node 2 as h_2 , etc. The potential $P(X,Y)$ in the electrolyte can be approximated by a polynomial.

$$P(X,Y) = P_0 + a_1x + a_2y + a_3x^2 + a_4y^2 + a_5xy$$

where the coefficients a_i are to be determined. Node 0 is considered to represent the origin of the cartesian system

$$\left. \frac{\partial^2 P}{\partial x^2} \right)_{x=y=0} = 2a_3 \qquad \left. \frac{\partial^2 P}{\partial y^2} \right)_{x=y=0} = 2a_4$$

$$P_1 - P_0 = -a_1h_1 + a_3h_1^2$$

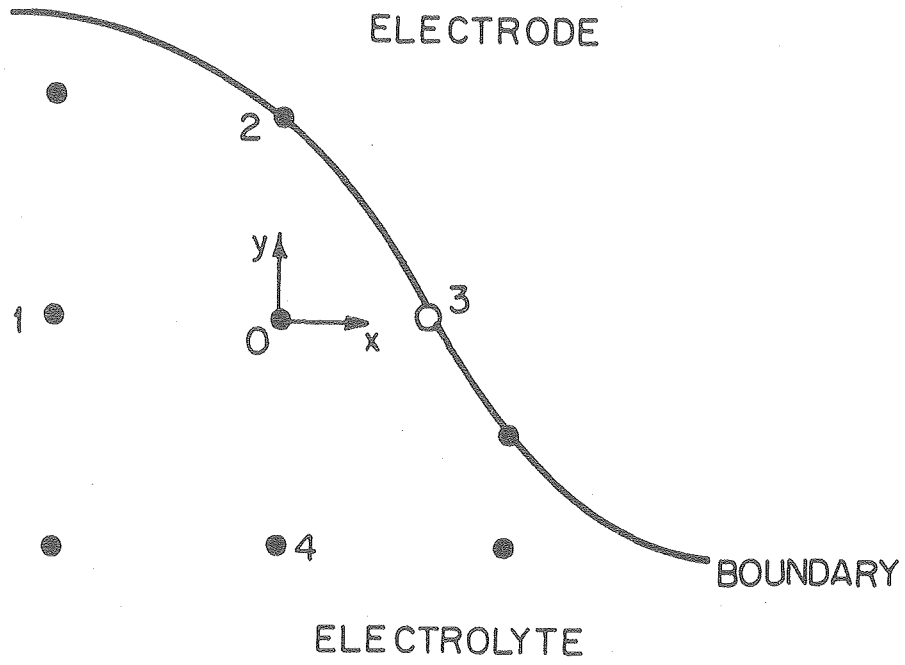
$$P_3 - P_0 = a_1h_3 + a_3h_3^2$$

$$P_2 - P_0 = a_2h_2 + a_4h_2^2$$

$$P_4 - P_0 = -a_2h_4 + a_4h_4^2$$

Solving for a_3 and rearranging

$$a_3 = \left[P_1 - P_0 \left(1 + \frac{h_1}{h_3} \right) + \frac{h_1}{h_3} P_3 \right] / h_1^2 \left(1 + \frac{h_3}{h_1} \right)$$



XBL 808-5741

Node arrangement for potential calculations.

Analogously,

$$a_4 = \left[P_2 - P_0 \left(1 + \frac{h_2}{h_4} \right) + \frac{h_2}{h_4} P_4 \right] / h_2^2 \left(1 + \frac{h_4}{h_2} \right)$$

Since

$$\frac{\partial^2 P}{\partial x^2} + \frac{\partial^2 P}{\partial y^2} = 0 = a_3 + a_4$$

then

$$P_0 = \frac{\frac{P_1 + \frac{h_1}{h_3} P_3}{h_1^2 \left(1 + \frac{h_3}{h_1} \right)} + \frac{P_2 + \frac{h_2}{h_4} P_4}{h_2^2 \left(1 + \frac{h_4}{h_2} \right)}}{\frac{1 + \frac{h_1}{h_3}}{h^2 \left(1 + \frac{h_3}{h_1} \right)} + \frac{1 + \frac{h_2}{h_4}}{h^2 \left(1 + \frac{h_4}{h_2} \right)}}$$

For $h_1 = h_2 = h_3 = h_4$

$$P_0 = (P_1 + P_2 + P_3 + P_4)/4$$

APPENDIX G

NUMERICAL DIFFERENTIATION PROCEDURE

In order to calculate the normal current density at node 0 on the electrode surface (Fig. a), the components of the field in the X and Y directions must first be calculated. The components can then be projected onto the line normal to the electrode surface as indicated in Eq. (9). An expression for the Y-component of the field can be derived by expanding the potentials P at node 1 and node 2 in a Taylor series about the potential at node 0. One then solves for P_y which is equal to the negative of the y-component of the electric field.

$$P_1 = P_0 - \alpha h P_y + \frac{(\alpha h)^2}{2} P_{yy}$$

$$P_2 = P_0 - (1 + \alpha) h P_y + \frac{(1 + \alpha)^2 h^2}{2} P_{yy}$$

where

h is the standard node spacing

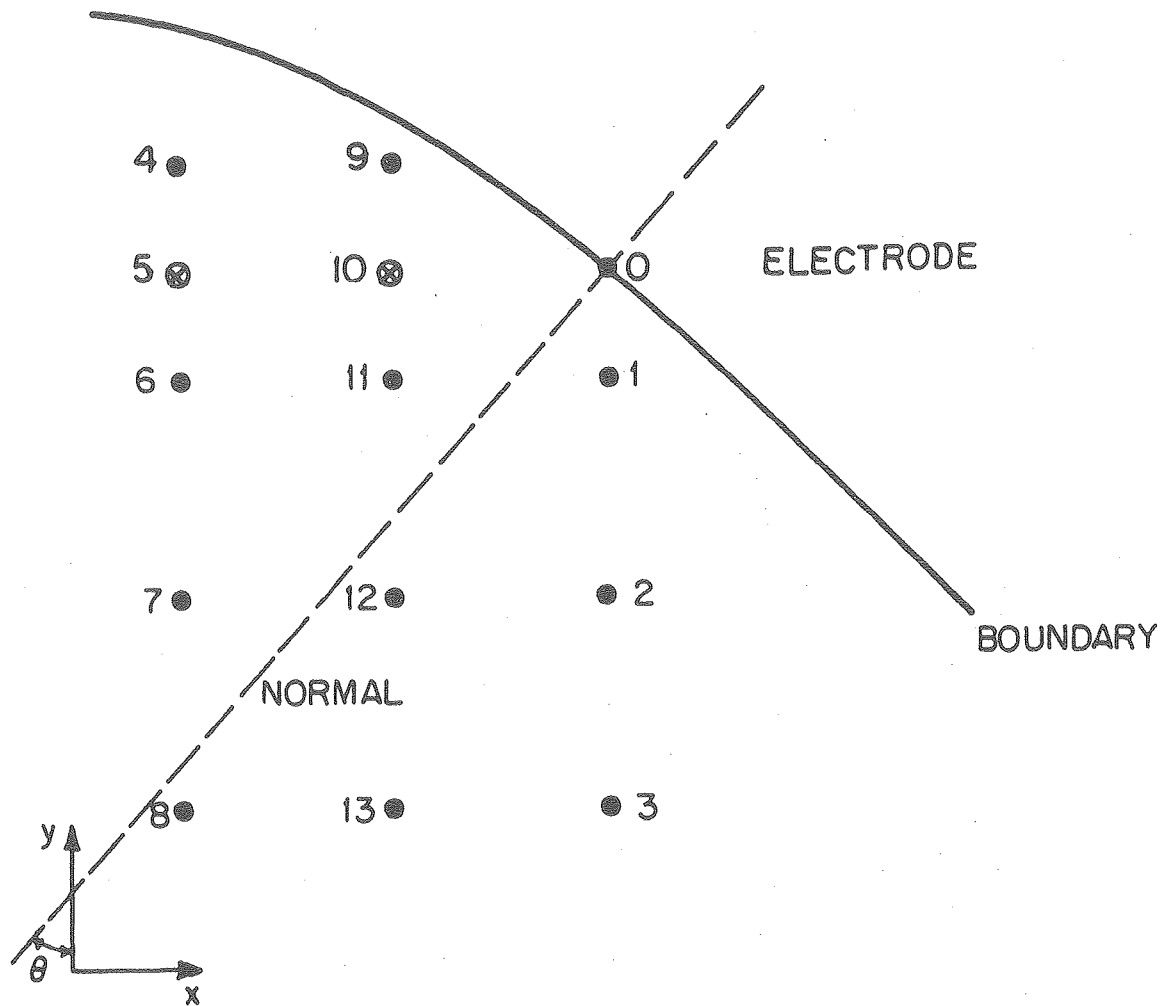
αh is the distance between nodes 0 and 1

$$P_y = \left(\frac{\partial P}{\partial y} \right)_0$$

$$P_{yy} = \left(\frac{\partial^2 P}{\partial y^2} \right)_0$$

Eliminating P_{yy}

$$P_3 = P_0 - (1 + \alpha) h P_y + \frac{(1 + \alpha)^2 h^2}{2} \left(\frac{2}{\alpha^2 h^2} \right) \left(P_1 - P_0 + \alpha h P_y \right)$$



XBL 808-5742

Fig. a. Node arrangements for numerical differentiation.

Solving for P_y and rearranging gives the desired equation

$$P_y = \frac{1}{h} \left[\frac{\alpha (P_2 - P_0)}{1 + \alpha} - \frac{(1 + \alpha)}{\alpha} (P_1 - P_0) \right]$$

For α equal to one, i.e., equal node spacing

$$P_y = \frac{1}{h} \left(\frac{1}{2} P_2 - 2P_1 + \frac{3}{2} P_0 \right)$$

Analogously, in the X-direction

$$P_x = \frac{1}{h} \left[\frac{B}{1+B} (P_5 - P_0) - \frac{(1+B)}{B} (P_{10} - P_0) \right]$$

where Bh is the distance from node 10 to node 0. The method of determining the potentials at nodes 5 and 10 is described in Appendix C.

When the angle θ is large, variations in the potential in the X-direction cause inaccuracies in the Y-direction interpolation. Therefore, for $\tan^{-1}\theta$ greater than $0.7(\theta = 35^\circ)$, the X-component of the field is calculated by a different method. In this case two numerical differentiations are performed and the results linearly interpolated. First, the potential at nodes 9, 4, and 14 are differentiated then the same can be done for potentials 1, 11, and 6. A linear interpolation in the Y-direction gives the result.

APPENDIX H

LAGRANGIAN INTERPOLATION

The potentials at points not on the grid can be approximated by a quadratic Lagrangian interpolation formula. The potential at node 10 (see appendix B, Fig. a) is given by

$$P_{10} = P_{12} \frac{d(d-h_u)}{h_d(h_d+h_u)} - P_{11} \frac{(d-h_u)(h_d+d)}{h_u h_d} + P_9 \frac{d(h_d+d)}{h_u(h_d+h_u)}$$

where

h_d is the distance between nodes 11 and 12

h_u is the distance between nodes 9 and 11

d is the distance between nodes 10 and 11

P_5 is obtained in an analogous manner.

APPENDIX I

OVERPOTENTIAL CALCULATIONS IN THE BUTLER-VOLMER EQUATION

The implicit solution of the Butler-Volmer equation for the overpotential is most easily performed by using Newton's method.

$$i = i_o (e^{B_a \eta} - e^{-B_c \eta})$$

where

$$B_a = \frac{\alpha_a F}{RT}$$

$$B_c = \frac{\alpha_c F}{RT}$$

the function G is defined such that G is zero when the overpotential at the r th iteration is the solution for a specified current density

$$G^{(r)} = i_o (e^{B_a \eta^{(r)}} - e^{-B_c \eta^{(r)}}) - i$$

$$\frac{dG}{d\eta}^{(r)} = i_o \left(B_a e^{B_a \eta^{(r)}} + B_c e^{-B_c \eta^{(r)}} \right)$$

An initial guess must be made for the overpotential. An improved estimate of the overpotential is

$$\eta^{(r+1)} = \eta^{(r)} - G^{(r)} / \frac{dG}{d\eta}^{(r)}$$

This improved estimate is then substituted into the defining equation, and the iteration continued until G is less than a specified convergence criterion.

APPENDIX J

INITIAL ESTIMATE FOR SURFACE POTENTIAL

The initial estimate for the surface potential can be calculated by solving the corresponding one-dimensional problem. Tafel kinetics is assumed to apply, and the concentration overpotential can be obtained from Eq. (4). In addition, only the cathode is polarized.

$$\eta = B \ln |i| / i_o + \frac{RT}{nF} \ln(1 - |i| / i_1) \quad (1)$$

$$|i| = |-k(V_A - \phi_0)| / Y \quad (2)$$

$$\phi_0 = V_c - \eta \quad (3)$$

Substituting Eqs. (1) and (2) into (3) yields

$$\phi_0 = V_c + B \ln \left[\frac{k(V_A - \phi_0)}{Y i_o} \right] - \frac{RT}{nF} \ln \left[1 - \frac{k(V_A - \phi_0)}{Y i_1} \right]$$

where

V_A is the anode potential

V_C is the cathode potential

B is the Tafel slope ($RT/\alpha_c F$)

Y is the anode-cathode separation

I define the function F such that the magnitude of F is less than a specified convergence criterion and $\phi_0^{(r)}$ is the solution at the r th iteration

$$F^{(r)} = V_c + B \ln \left[\frac{\kappa (V_A - \phi_0^{(r)})}{Yi_0} \right] - \frac{RT}{nF} \ln \left[1 - \frac{\kappa (V_A - \phi_0^{(r)})}{Yi_1} \right] - \phi_0^{(r)}$$

$$\left(\frac{dF}{d\phi_0} \right)^{(r)} = - \frac{B}{V_A - \phi_0^{(r)}} - \frac{\frac{RT}{nF}}{\left(\frac{Yi_1}{\kappa} - V_A + \phi_0^{(r)} \right)} - 1$$

A better estimate of ϕ_0 is

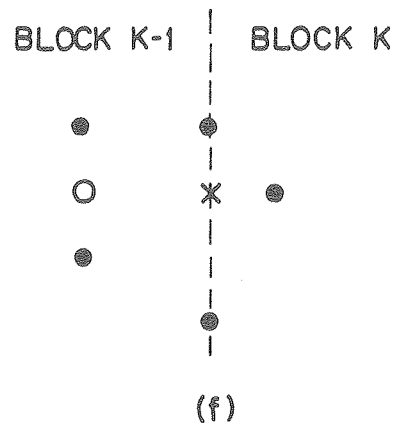
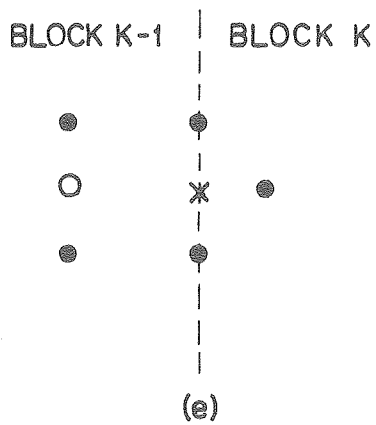
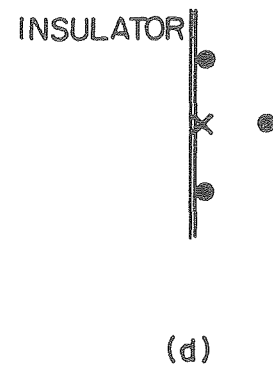
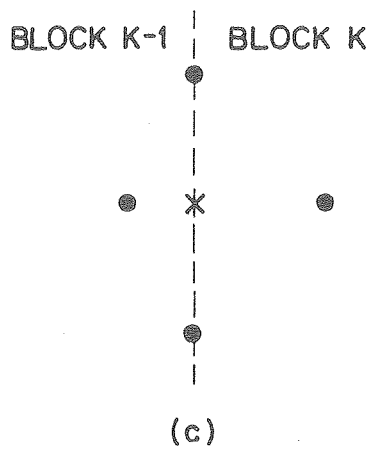
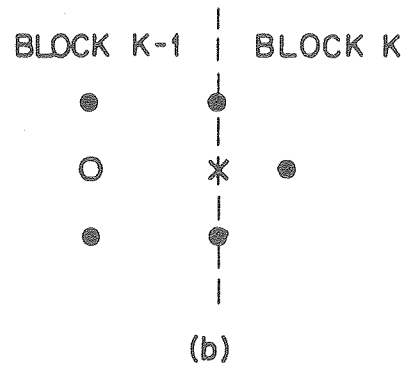
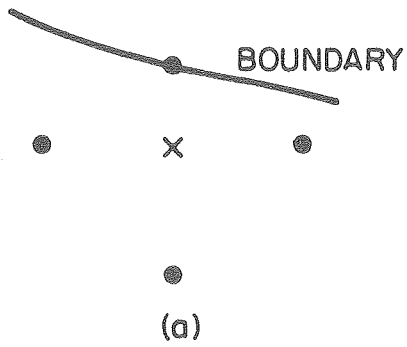
$$\phi_0^{(r+1)} = \phi_0^{(r)} - F^{(r)} / (dF/d\phi_0)^{(r)}$$

This estimate is then substituted into the expression for $F^{(r)}$ and iteration continued. An initial guess of ϕ_0 near the anode potential is required for computational stability.

APPENDIX K

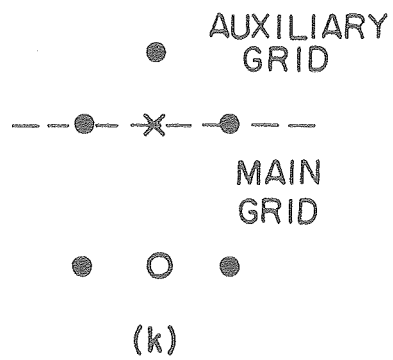
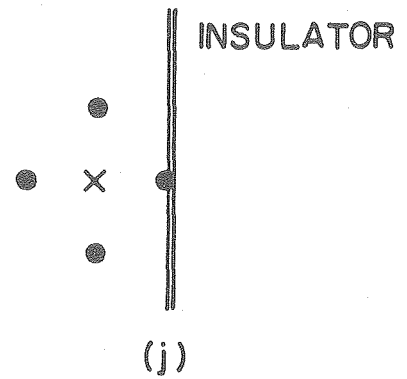
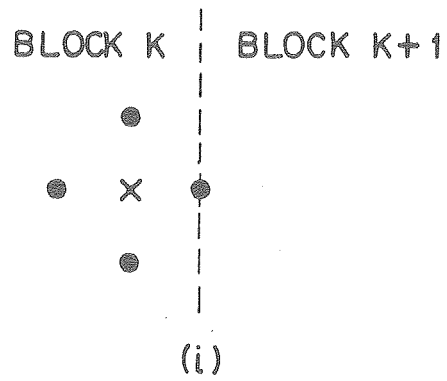
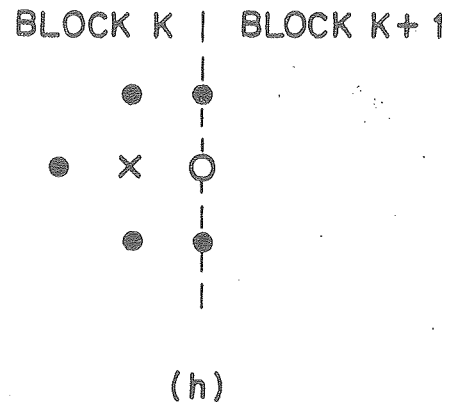
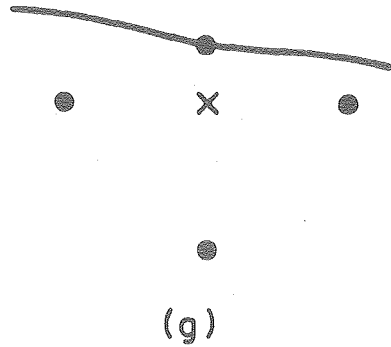
NODE ARRANGEMENTS FOR POTENTIAL CALCULATIONS

The method described in Appendix A is used to calculate the potential at each node. The node arrangement for each type of calculation is illustrated in the following figures. The potential at the node indicated by an x is the one to be calculated. In the figures the I-1 position is at the left, the J+1 above, the I+1 to the right, and the J-1 below. The open circles represent interpolated values.



XBL808-5744

Node arrangements for potential calculations.

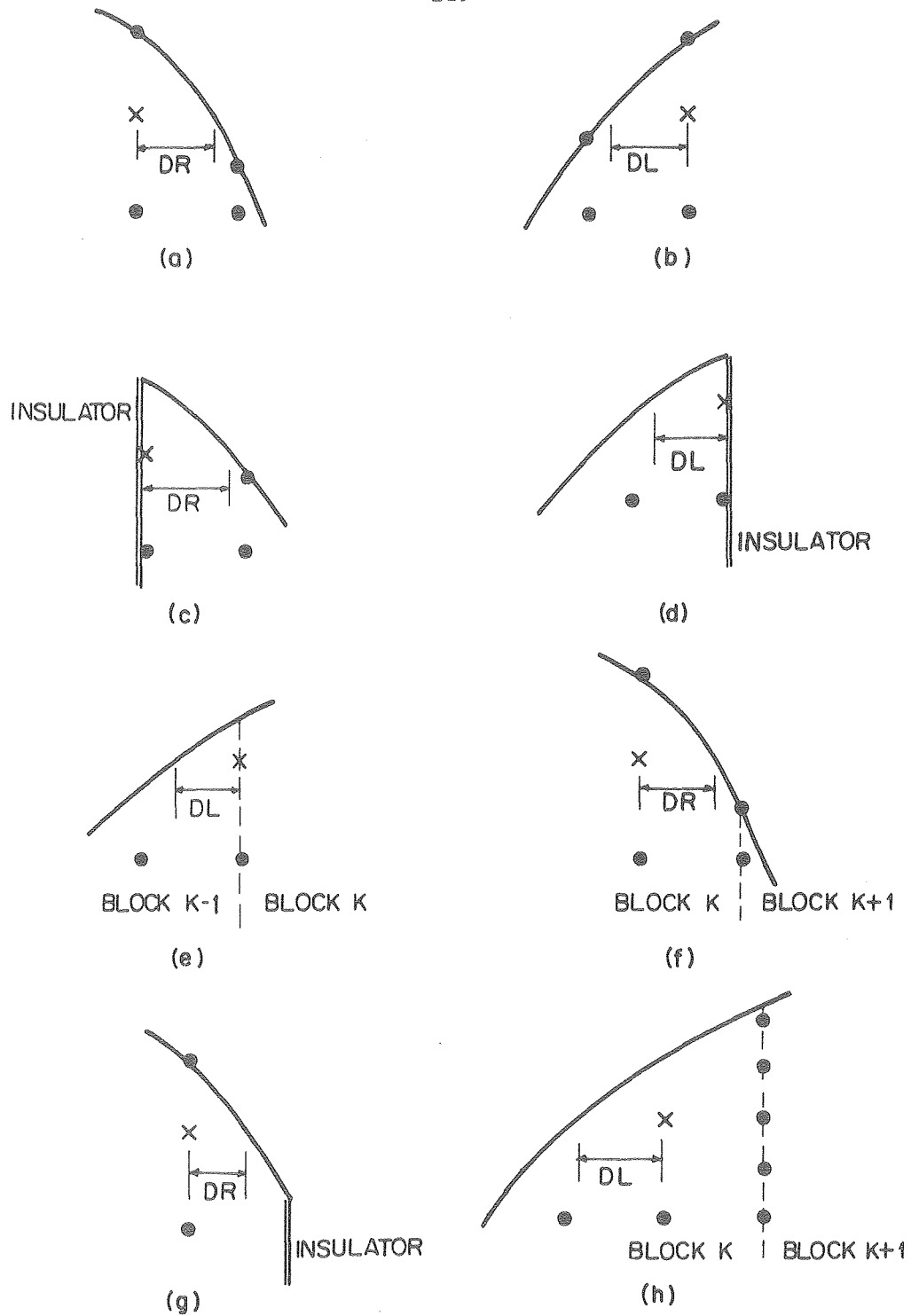


XBL 808-5745

APPENDIX L

NODE ARRANGEMENT FOR POTENTIAL CALCULATION NEAR SURFACE

The nodes adjacent to the boundary, where special treatment is required, are illustrated below. The node where the potential is to be calculated is indicated by an x.



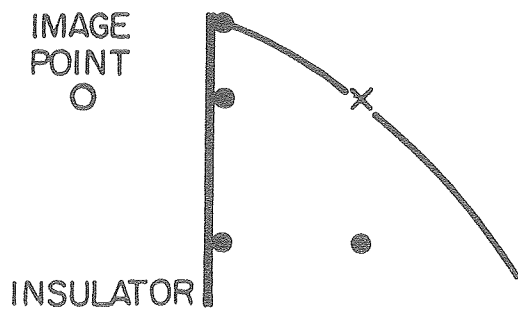
XBL 808-5746

Node arrangements for calculation of potential near the electrode surface.

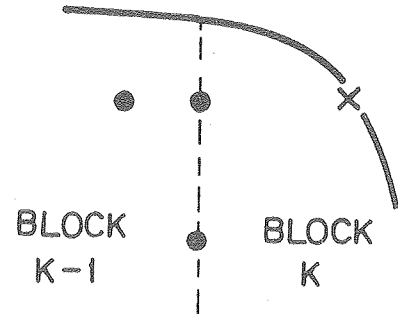
APPENDIX M

NODE ARRANGMENTS FOR CURRENT CALCULATIONS

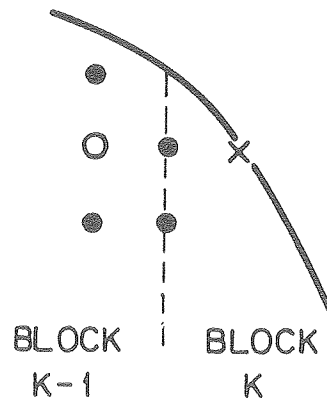
The nodes used in the three point numerical differentiation formula (see Appendices B and C) are illustrated below.



(a)



(b)



(c)

XBL 808-5747

Node arrangements for current density calculations.

REFERENCES

1. C. Kasper, Trans. Electrochem. Soc., 77, 353 (1940); 77, 365 (1940); 78, 131 (1940); 78, 147 (1940); 82, 153 (1942).
2. C. Wagner, J. Electrochem. Soc., 98, 116 (1951).
3. J. A. Klingert, S. Lynn, and C. W. Tobias, Electrochimica Acta, 9, 297 (1964).
4. R. N. Fleck, D. N. Hanson, and C. W. Tobias, Lawrence Radiation Laboratory, Berkeley, California, Sept. 1964 (UCRL-11612).
5. J. Newman, J. Electrochem. Soc., 113, 1235 (1966).
6. W. R. Parrish and J. Newman, J. Electrochem. Soc., 116, 169 (1969).
7. R. Caban and T. Chapman, J. Electrochem. Soc., 123, 1036 (1976).
8. C. Wagner, J. Electrochem. Soc., 101, 225 (1954).
9. R. H. Nilson and Y. G. Tsuei, Trans. ASME, 98, 54 (1976).
10. R. H. Nilson and Y. G. Tsuei, Computer Methods in Appl. Mech. and Eng., 6, 265 (1975).
11. J. B. Riggs, R. H. Muller, and C. W. Tobias, Electrochimica Acta, in press.
12. K. W. Choi, D. N. Bennion, and J. Newman, J. Electrochem. Soc., 123, 1616 (1976).
13. R. Alkire, T. Bergh, and R. L. Sani, J. Electrochem. Soc., 125, 1981 (1978).
14. K. H. Huebner, "The Finite Element Method for Engineers", John Wiley and Sons, New York (1975).
15. J. H. Hohl and D. J. Hamilton, J. Electrochem. Soc., 124, 1912 (1977).
16. L. Lapidus, "Digital Computation for Chemical Engineers", McGraw-Hill, New York (1962).

17. A. J. Ahlberg, E. N. Nilson, and J. L. Walsh, "The Theory of Splines and Their Applications," Academic Press, New York (1967).
18. M. Eisenberg, C. W. Tobias, and C. R. Wilke, J. Electrochem. Soc., 101, 306 (1954).
19. L. L. Scheir and J. W. Smith, J. Electrochem. Soc., 99, 64 (1952).
20. E. Mattsson and J. O. Bockris, Trans. Faraday Soc., 55, 1586 (1959).
21. D. R. Turner and G. R. Johnson, J. Electrochem. Soc., 109, 798 (1962).
22. J. Newman, "Electrochemical Systems", Prentice-Hall, Englewood Cliffs, New Jersey (1973).
23. T. P. Hoar, in "Modern Aspects of Electrochemistry", J. O. Bockris, ed., vol. 2 (1959).
24. E. F. Kern and M. Y. Chang, Trans. Am. Electrochem. Soc., 41, 181 (1923).
25. P. Fedkiw, J. Electrochem. Soc., 127, 1304 (1980).
26. R. Kung, "Users Guide to the Sandia Mathematical Program Library at Berkeley," Lawrence Berkeley Laboratory Report, LBID-002 (1979); Program available from R. E. Huddleston, Applied Math. Div. 8332, Sandia Laboratory, Livermore, CA 94550.

